POLITECNICO DI TORINO

Master Degree in Aerospace Engineering

Master thesis

Data fusion between strain data from strain gauges and displacement data from image registration

Politecnico di Torino
1859

Supervisors

Prof. Gherlone Marco, Supervisor

Prof. Lattanzi David, Co-Supervisor

Prof. Surace Cecilia, Co-Supervisor

Candidate

Giuseppe Ciaramella

290489

A.Y. 2023-2024

Contents

Sommario 1

Abstract 2

1 State of the art 3
- 1.1 Shape sensing . . . 3
  - 1.1.1 Methods based on the numerical integration of experimental strains . . 4
  - 1.1.2 Methods based on global or piecewise continuous basis functions . . . 6
  - 1.1.3 Methods based on Neural Networks (NN) . . . 7
  - 1.1.4 Methods based on a finite-element discrete variational principle 8
- 1.2 Image registration . . . 10
  - 1.2.1 Digital image correlation . . . 11
  - 1.2.2 Image matching - Thirion Diffusion process . . . 17

2 Formulation of the beam inverse finite element 21
- 2.1 Timoshenko beam element . . . 21
  - 2.1.1 Estimating strain measures . . . 25
- 2.2 Bernoulli-Euler beam element . . . 28
  - 2.2.1 Element shape functions . . . 31
  - 2.2.2 Estimating strain measures . . . 32

3 Strain measuring sensors 34
- 3.1 Fiber Bragg Grating . . . 34
- 3.2 Strain Gauge . . . 36

4 Experimental tests 41
- 4.1 Experiment 1 . . . 41
  - 4.1.1 Experimental setup . . . 42
  - 4.1.2 Loads and boundary conditions . . . 46
- 4.2 Experiment 2 . . . 48
  - 4.2.1 Experimental setup . . . 48
  - 4.2.2 Loads and boundary conditions . . . 53

5 Data fusion: developed algorithms 54
- 5.1 First method . . . 55
  - 5.1.1 Computation of $v(z)$ . . . 55
  - 5.1.2 Computation of $\varepsilon(z)$ . . . 61

5.1.3 Computation of $\varepsilon_{fix}(z)$ . . . 62
5.1.4 Computation of $v_{fix}(z)$ . . . 64
5.1.5 Changes for the second experiment . . . 66
5.2 Second method . . . 70
5.2.1 Shape sensing $(\varepsilon_{fix}(z))$ . . . 70

6 Results **72**
6.1 Experiment 1 . . . 72
6.1.1 Experimental measurements . . . 73
6.1.2 Parametric smoothing parameter analysis . . . 75
6.1.3 Method 1 results . . . 78
6.1.4 Accuracy of method 1 . . . 82
6.2 Experiment 2 . . . 84
6.2.1 Experimental measurements . . . 84
6.2.2 Method 1 results . . . 88
6.2.3 Accuracy of method 1 . . . 89
6.2.4 Method 2 results . . . 91

7 Conclusions **93**

A Expression of Lagrange polynomials **95**

B Smoothing spline formulation **96**
B.1 Lagrangian parameter minimisation . . . 98

References **100**

Sitography **103**

List of Figures

1.1 Example of a Neural Network [35] . . . 7
1.2 DIC set up for 2D displacement [14] . . . 11
1.3 Example of an evenly-spaced virtual grid of the ROI [14] . . . 12
1.4 Example of speckle patterns with different diameter sizes [16] . . . 13
1.5 Reference subset before and after the deformation [14] . . . 15
1.6 Instantaneous velocity from image M to image S [24] . . . 17
1.7 Deformable model with demons (2D case) [25] . . . 18
1.8 Iterative scheme [24] . . . 19

2.1 Beam reference system $0\,(x, y, z)$ [26] . . . 21
2.2 Beam inverse finite element geometry and nodes [26] . . . 25
2.3 (a) Beam geometry and kinematic variables, (b) beam cross section with the parameter c indicating the distance along the perimeter, (c) strain gauge placed on the surface of the beam, oriented at an angle β with respect to the axis of the beam [28] . . . 26
2.4 Beam reference system (x, y, z) [29] . . . 28
2.5 0^{th} order element [29] . . . 32
2.6 Strain gauge coordinate system [29] . . . 33

3.1 Bragg fiber [36] . . . 34
3.2 Snell's Law . . . 35
3.3 An electric strain gauge [37] . . . 36
3.4 Mechanical principle [30] . . . 36
3.5 Wheatstone bridge . . . 37
3.6 Full bridge configuration . . . 38
3.7 Half bridge configuration (type II) . . . 39
3.8 Quarter bridge configuration . . . 39
3.9 Half bridge configuration (type I) . . . 40

4.1 Beam geometric dimensions . . . 41
4.2 Beam cross-section in main inertia reference system . . . 42
4.3 Structural pivot [38] . . . 43
4.4 Structural pivot - beam . . . 43
4.5 Roller constraint . . . 44
4.6 Laser sensor on its support . . . 44
4.7 Camera on its support . . . 45
4.8 Experiment 1 setup . . . 45

4.9 Kind of weight used for the test 46
4.10 Beam geometric dimensions 48
4.11 Strain gauges locations 49
4.12 Beam pattern for Thirion's demons algorithm and 3D DIC 49
4.13 Clamp constraint 50
4.14 LVDTs used in the test 50
4.15 Image taken by DIC - Marker under the LVDT 51
4.16 Loading system 51
4.17 Cameras and lights for DIC and IIM techniques 52
4.18 Blackboard in the background 53

5.1 Data fusion methods 54
5.2 Frames taken from the video 55
5.3 Post-processed frames 56
5.4 Pixel windows 56
5.5 Displacement punctual data 58
5.6 First Interpolation 59
5.7 Displacement calculation flowchart 60
5.8 $v\left(z\right)$ displacement function 61
5.9 $\varepsilon\left(z\right)$ strain function 62
5.10 Strain field correction flowchart 62
5.11 $\varepsilon_{fix}\left(z\right)$: First interpolation 63
5.12 $\varepsilon_{fix}\left(z\right)$ strain function 64
5.13 v_{fiz} displacement function 66
5.14 Image took by the IIM camera from test 1 67
5.15 Experiment 2 - Pre-processed image 67

6.1 Case study 01 subcase 1: best $K = 17$ 75
6.2 Case study 01 subcase 2: best $K = 88$ 76
6.3 Case study 01 subcase 3: best $K = 7$ 76
6.4 Case study 02: best $K = 108$ 77
6.5 Case 01 - Subcase 1 78
6.6 Case 01 - Subcase 2 78
6.7 Case 01 - Subcase 3 79
6.8 Case 02 79
6.9 Case 03 - Subcase 1 80
6.10 Case 03 - Subcase 2 80
6.11 Case 03 - Subcase 3 81
6.12 Case 04 - Subcase 1 81
6.13 Case 04 - Subcase 2 82
6.14 $u\left(z\right)$ displacement 86
6.15 $u\left(z\right)$ displacement 87
6.16 Test 2 88
6.17 Test 3 89

List of Tables

4.1 Beam geometric properties and material characteristics . . . 41
4.2 Case studies . . . 47
4.3 Beam geometric properties and material characteristics . . . 48
4.4 Case studies . . . 53

5.1 iFEM - Bernoulli-Euler beam . . . 70
5.2 iFEM - Timoshenko beam . . . 71

6.1 Case study 01 - Subcase 1 . . . 73
6.2 Case study 01 - Subcase 2 . . . 73
6.3 Case study 01 - Subcase 3 . . . 73
6.4 Case study 02 . . . 73
6.5 Case study 03 - Subcase 1 . . . 73
6.6 Case study 03 - Subcase 2 . . . 74
6.7 Case study 03 - Subcase 3 . . . 74
6.8 Case study 04 - Subcase 1 . . . 74
6.9 Case study 04 - Subcase 2 . . . 74
6.10 Errors between displacements provided by the IIM method and those provided by the sensor laser . . . 77
6.11 Method 1 results . . . 83
6.12 Experimental measurements and relative percentage errors for 5 kg . . . 84
6.13 Absolute and relative percentage errors - 5 kg . . . 90
6.14 Comparison of centreline displacement before and after data fusion . . . 90
6.15 iFEM case study . . . 91
6.16 iFEM results . . . 91

Sommario

Nell'analisi strutturale, diversi strumenti possono essere utilizzati per misurare la posizione, la distanza o la vibrazione di un oggetto. Tali strumenti possono essere suddivisi in due categorie fondamentali: strumenti di misura a contatto e strumenti di misura non a contatto.
Tra le numerose tipologie di misurazioni non a contatto, vi sono le tecniche di *registrazione dell'immagine* e di flusso ottico. Con l'utilizzo di una fotocamera, è possibile calcolare il movimento di tutti i punti della struttura da questa ripresi. Con queste tecniche, se da un lato è possibile ottenere lo spostamento in numerosi punti della struttura senza la necessità di una strumentazione complessa, dall'altro i dati ottenuti sono affetti da un elevato livello di rumore.
Tra i tipi di misura a contatto ci sono gli estensimetri, che forniscono i valori di deformazione della struttura nei punti in cui sono installati. Con gli estensimetri, utilizzando tecniche di *shape-sensing*, è possibile calcolare lo deformata della struttura in tempo reale. Ma se da un lato i dati forniti dai sensori di deformazione sono molto precisi, dall'altro è necessario installarne un gran numero per ricostruire la deformata della struttura con una certa accuratezza.

Lo scopo di questa tesi è quello di effettuare una fusione tra i dati forniti dalla registrazione delle immagini e dati di deformazione, per migliorare il campo di spostamento che si otterrebbe utilizzando le due tecniche in modo indipendente. La fusione dati sarà eseguita su due prove sperimentali relative a due diverse travi, utilizzando una fotocamera e degli estensimetri.

In questa tesi verranno innanzitutto illustrate le tecniche di registrazione delle immagini e di shape-sensing. Dopo una breve rassegna degli strumenti utilizzati per la misurazione delle deformazioni, seguiranno le descrizioni delle prove sperimentali e degli algoritmi sviluppati per eseguire la fusione dati. Infine, verranno presentati i risultati delle analisi, con una valutazione sull'efficacia dei metodi insieme alle conclusioni.

Abstract

In structural analysis, different tools can be used to measure an object's position, distance, or vibration. Such instruments can be divided into two basic categories: contact and non-contact instruments.
Among the types of non-contact measurements, there are *image registration* and optical flow techniques. With a camera, it is possible to calculate the movement of all the points of the structure taken up by the camera. With these techniques, while on the one hand, it is possible to obtain the displacement in numerous points of the structure without the need for complex instrumentation, on the other hand, the data obtained are affected by a high level of noise.

Among the types of contact measurements, there are *strain gauges*, which provide the strain values of the structure at the points where they are installed. With strain gauges, using shape-sensing techniques, it is possible to calculate the deformation of the structure in real time. But, if on the one hand, the data provided by the strain sensors are very precise, on the other it is necessary to install a large number of them in order to reconstruct the deformation of the structure with a certain accuracy.

The aim of this thesis is to perform a data fusion between image and strain data to improve the displacement field that would be obtained using the two techniques independently. The data fusion will be performed on two experimental tests regarding two different beams, using a camera and strain gauges.

In this thesis, image registration and shape-sensing techniques will first be illustrated. After a brief review of the instruments used for measuring strain, the descriptions of the experimental tests and algorithms developed to perform the data fusion will follow. Finally, the results of the analysis will be presented, with an evaluation of the effectiveness of the methods together with the conclusions.

1 State of the art

This chapter is divided into two main sections, in the first one shape sensing and its main techniques are shown. In the second section image registration and two related techniques, digital image correlation and Thirion's diffusion process, are exposed.

1.1 Shape sensing

The strain gauges and the optical fiber are among the types of contact measurements. These measuring instruments can be used to perform *shape sensing*: shape sensing is the real-time reconstruction of the displacement field of the structure from discrete surface strain measurements. Shape-sensing techniques have become increasingly popular in recent years. This is due to the potential of the method, which is able to evaluate in real-time the displacement and the tensional field of the structure. These characteristics make shape sensing especially suitable:

1. in the area of structural health monitoring systems (SHMS);
2. for the control and implementation of smart structures.

Using shape sensing for structural health monitoring purposes, not only allows for cheaper and more efficient maintenance procedures but also makes the structure safer [1]. By knowing the structure's stresses or strains magnitude in real-time, it's possible to make more efficient the maintenance activity by intervening only when required.
The other reason that makes shape sensing attractive is that the knowledge of the loads applied to the structure is not necessary. This is an important feature, especially in the aeronautical field where load identification is a hard task. The information required to perform shape sensing depends on the used methodologies, but every methodology needs to know:

- the discrete surface strain measurements and their locations on the structure;
- the structure boundary condition;
- the structure geometry.

Shape sensing methodologies can be grouped into the following four:

1. methods based on the numerical integration of experimental strains;
2. methods based on global or piecewise continuous basis functions;
3. methods based on Neural Networks (NN);
4. methods based on a finite-element discrete variational principle.

These methods will be illustrated individually in the order mentioned especially focusing on the quarter, being the method that will be used in the thesis.

1.1.1 Methods based on the numerical integration of experimental strains

To this category of methods belongs the Ko displacement theory, which can be applied to beams, wing boxes, and plates [2].
The basic formulation of Ko's theory, which is valid for uniform cantilever beams (i.e. the beam cross-section does not change), starts from the classical differential equation of the beam

$$\frac{d^2y}{dx^2} = \frac{M\left(x\right)}{EI} \tag{1.1}$$

where:

- y is the vertical displacement;
- x is the coordinate of the length of the beam;
- $M\left(x\right)$ is the bending moment;
- E is the Young modulus of the beam;
- I is the inertia moment of the beam section.

By combining Hooke's law and Navier's law (written in a principal inertia reference system), it can be written

$$M\left(x\right) = I\frac{\sigma\left(x\right)}{c} = EI\frac{\varepsilon\left(x\right)}{c} \tag{1.2}$$

where:

- c is the distance from the considered point of the section and the center of gravity;
- $\varepsilon\left(x\right)$ is the strain value of the bottom (or top) of the beam surface.

Substituting Equation 1.2 into Equation 1.1, lead to

$$\frac{d^2y}{dx^2} = \frac{\varepsilon\left(x\right)}{c} \tag{1.3}$$

The equation 1.3 is valid for uniform beam, but it can be also applied with adequate accuracy to no uniform beams in which the cross-section gradually change. It is noted that with a strain formulation, equation 1.3 contains only one geometric parameter of the beam (c), while the flexural stiffness EI simplifies.
Assume now that there are strain sensors installed at $n+1$ equally spaced stations along the lower or upper surface of the cantilever beam. Even though the bending strain at the free end of the beam is zero, a strain sensor (the *n-th* one) is there installed for mathematical convenience in the derivation of the spar tip slope and deflection equations. Assume that the bending moment $M\left(x\right)$ is a piecewise-linear function along the axial coordinate x. In the region

$x_{i-1} < x < x_i$ between any two adjacent strain-sensing stations, $\{x_{i-1}, x_i\}$, $M(x)$ is considered a linear function of $(x - x_{i-1})$, as

$$M(x) = M_{i-1} - (M_{i-1} - M_i)\frac{x - x_{i-1}}{\Delta l} \; ; \qquad x_{i-1} < x < x_i \tag{1.4}$$

where:

- $\{M_{i-1}, M_i\}$ are the bending moments in the two adjacent strain-sensing stations $\{x_{i-1}, x_i\}$;
- $\Delta l \left(= x_i - x_{i-1} = \frac{l}{n}\right)$ is the axial distance between two adjacent strain-sensing stations $\{x_{i-1}, x_i\}$.

In light of equation 1.2, the bending moment can be expressed in terms of the local bending strain, $\varepsilon(x)$, in the region $x_{i-1} < x < x_i$ as

$$\varepsilon(x) = \varepsilon_{i-1} - (\varepsilon_{i-1} - \varepsilon_i)\frac{x - x_{i-1}}{\Delta l} \; ; \quad x_{i-1} < x < x_i \; ; \quad \Delta l = \frac{l}{n} \tag{1.5}$$

where $\{\varepsilon_{i-1}, \varepsilon_i\}$ are the strains measured in two adjacent strain-sensing stations, $\{x_{i-1}, x_i\}$, respectively.

Slope Equations

The slope $\tan\theta(x)$ of the uniform beam in the region $x_{i-1} < x < x_i$ between two adjacent strain-sensing stations, $\{x_{i-1}, x_i\}$, can be obtained by integrating equation 1.3, with the determination of the constant of integration by enforcing the continuity of slope at the inboard adjacent strain-sensing station, x_{i-1}

$$\tan\theta(x) = \underbrace{\int_{x_{i-1}}^{x} \frac{d^2y}{dx^2}dx}_{\text{Slope increment}} + \underbrace{\tan\theta_{i-1}}_{\text{Slope at } x_{i-1}} = \int_{x_{i-1}}^{x} \frac{\varepsilon(x)}{c}dx + \tan\theta_{i-1} \; ; \quad x_{i-1} \le x \le x_i \tag{1.6}$$

where $\tan\theta_{i-1}$ (constant of integration) is the slope at the inboard adjacent strain-sensing station x_{i-1}. It's possible to calculate the $\tan\theta_i \equiv [\tan\theta_i(x)]$ expression at the strain-sensing station x_i by replacing the strain expression (equation 1.5) in equation 1.6 and integrating

$$\tan\theta_i = \frac{\Delta l}{2c}(\varepsilon_{i-1} + \varepsilon_i) + \tan\theta_{i-1} \; ; \quad (i = 1, 2, 3, ..., n) \tag{1.7}$$

Deflection Equations

The deflection $y(x)$ of the uniform beam in the region $x_{i-1} \le x \le x_i$, between two adjacent strain-sensing stations, $\{x_{i-1}, x_i\}$, can be calculated by integrating equation 1.6, with the determination of the constant of integration by enforcing the continuity of deflection at the inboard adjacent strain-sensing station, x_{i-1}

$$
\begin{aligned}
y\left(x\right) &= \underbrace{\int_{x_{i-1}}^{x} \tan\theta\left(x\right)dx +}_{\text{Integration of slope}} \underbrace{y_{i-1}}_{\text{Deflection at } x_{i-1}} \\
&= \underbrace{\int_{x_{i-1}}^{x}\int_{x_{i-1}}^{x} \frac{\varepsilon\left(x\right)}{c}dxdx +}_{\text{Deflection increment}} \underbrace{\int_{x_{i-1}}^{x} \tan\theta_{i-1}dx}_{\text{Deflection at } x \text{ due to } \tan\theta_{i-1}} + \underbrace{y_{i-1}}_{\text{Deflection at } x_{i-1}} \quad ; \quad x_{i-1} \leq x \leq x_i
\end{aligned}
\tag{1.8}
$$

where y_{i-1} (constant of integration) is the deflection at the inboard adjacent strain-sensing station x_{i-1}. It's possible to calculate the $y_i \equiv [y\left(x_i\right)]$ expression at the strain-sensing station x_i by replacing the strain expression (equation 1.5) in equation 1.8

$$
y_i = \frac{\left(\Delta l\right)^2}{6c}\left(2\varepsilon_{i-1} + \varepsilon_i\right) + y_{i-1} + \Delta l \tan\theta_{i-1}\ ; \quad \left(i = 1, 2, 3, ..., n\right) \tag{1.9}
$$

In order to calculate beam deflection it's necessary to know c. What has been written so far is applicable to cantilever beams subjected to bending, but Ko's displacements theory also provides for the case where the beam is subjected to twisting and both bending and twisting. Ko's displacements theory provides the determination of structure deformation even in the case of the tapered and lightly tapered beam. The above can be applied also to non-uniform cantilevered beam [3], i.e. beams whose cross-section slowly changes along the beam axis. In [3] is provided a procedure to calculate the deflection of a non-uniform beam without constraints such as a fuselage is. In the end, the deflection equations developed for the cantilevered beam can be used to predict the deflection of other structures, such as wing boxes and plates.

1.1.2 Methods based on global or piecewise continuous basis functions

In these types of methods, continuous piecewise or global functions are assumed to approximate the strain field. When the functions used are the structure's own modes of vibration, these methods are called *modal methods*. These are particularly attractive due to the low computational cost and the possibility to compute the structure modal characteristics with the finite element method (FEM). The basic steps of the modal method are reported [4].
Consider that the structure under consideration, e.g. a beam, has been discretized in a finite element domain, the displacement field and the strain field can be expressed as

$$
\{\delta\} = [\phi_d]\{q\} \tag{1.10}
$$

$$
\{\varepsilon\} = [\phi_s]\{q\} \tag{1.11}
$$

where:

- $\{\delta\}$ is the nodal displacements vector;
- $\{\varepsilon\}$ is the strains vector;
- $[\phi_d]$ is the modal displacements matrix;

- $[\phi_s]$ is the modal strains matrix;
- $\{q\}$ is the modal coordinates vector.

$[\phi_d]$ and $[\phi_s]$ can be computed with an eigenvalue analysis. The deformation of a structure can be approximated by the modal shape when each mode is multiple for the appropriate generalized coordinate. The approximation accuracy gets better with the increasing of considered modes. Therefore, a modal cutoff criterion has to be determined in order to select the appropriate number of modal shapes to reconstruct the displacement field accurately.
The calculation of $\{q\}$ in equation 1.11 is facilitated by the introduction of strain modes. The strain mode is typically defined as the set of strains associated with a given strain mode[4]. Referring to the equation 1.11, if the strains are known, the generalized coordinate can be calculated as

$$\{q\} = [\phi_s]^{-1} \{\varepsilon\} \tag{1.12}$$

Furthermore, by multiplying both members of equation 1.12 by $[\phi_s]^T$ and solving with respect to $\{q\}$ leads to

$$\{q\} = \left[[\phi_s]^T [\phi_s] \right]^{-1} [\phi_s]^T \{\varepsilon\} \tag{1.13}$$

Thus, the displacement field can be obtained by substituting equation 1.13 into equation 1.10,

$$\{\delta\} = [\phi_d] [\phi_s]^T [\phi_s]^{-1} [\phi_s]^T \{\varepsilon\} \tag{1.14}$$

1.1.3 Methods based on Neural Networks (NN)

Artificial neural networks consist of layers of nodes containing input layers, one or more hidden layers, and output layers.

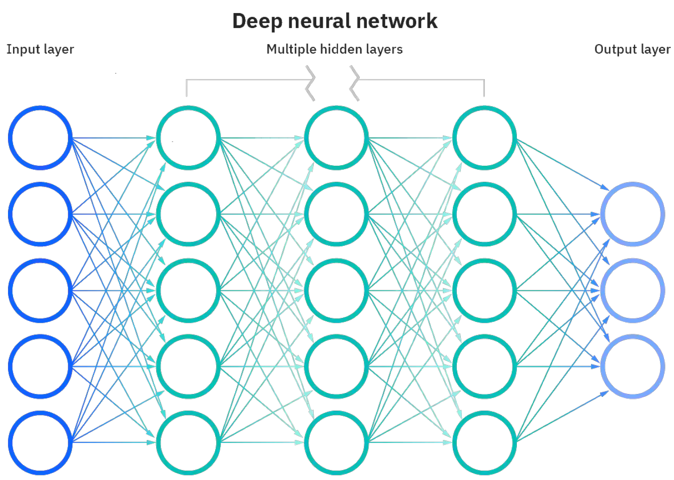

Figure 1.1: *Example of a Neural Network [35]*

In the neural network the information, in the form of patterns or signals, is transferred to neurons in the input layer, where they are processed. Each neuron is assigned a weight so that the neurons receive different importance. The weight, together with a transfer function, determines the input, where the neuron is then forwarded. In the next step, an activation function and a threshold value calculate and weigh the output value of the neuron. Depending on the information evaluation and weighting, other neurons are connected and activated to a greater or lesser extent. If the output of any individual node is above the specified threshold value, that node is activated, sending data to the next network layer. Otherwise, no data is passed to the next layer of the network. Neural networks rely on training data to learn and improve their accuracy over time. It is precisely this aspect that is one of the limitations of NN methods: some work shows that an NN model trained on the solutions of a wide range of possible disturbances is unable to estimate the solutions of problems whose inputs deviate from those of the training set. Indeed, among the main factors influencing the results are the type and quantity of training cases [5, 6].

1.1.4 Methods based on a finite-element discrete variational principle

These types of methods can be regarded as inverse finite element methods, based on the variational least-squares principle and finite element discretization [7]. The *inverse finite element method* (iFEM) has been introduced for the first time by Tessler and Spangler [8]. The formulation is based on the minimization of the least squares functional using the set of deformation measurements consistent with First-order Shear Deformation Theory (FSDT). The main advantage of the variational principle is that it is suitable for discretizations of continuous displacement finite elements C^0, thus enabling the development of robust algorithms for application to complex civil and aircraft structures.
Among the shape-sensing methods mentioned above, the iFEM methodology is the most robust and suitable approach for shape sensing because it allows the most critical challenges of general shape-sensing procedures to be faced and overcome [7]. These challenges are:

- suitability for complex boundary conditions and structural topology;
- real-time displacement field calculation;
- independence from intrinsic noise in strain measurements;
- no needs for loading and materials information.

As said it's confirmed by Gherlone et al. in [9]. In this paperwork, a wing-shaped aluminum plate is let to deform under its own weight being submitted to bending and twisting. Using experimental strain measurements as input, the deformation of the structure is reconstructed with Ko's displacements method, with the modal method, and with iFEM. The accuracy of the three methods was evaluated by introducing the percent difference of the reconstructed deflection, w^{rec} (obtained using digital image correlation), with respect to the experimentally measured one, w^{exp}:

$$\%\text{Diff}\left(w\left(j\right)\right) = 100 \cdot \left[\frac{w^{rec}\left(j\right) - w^{exp}\left(j\right)}{max\left(w^{exp}\left(j\right)\right)}\right] \tag{1.15}$$

where $max\left(w^{exp}\left(j\right)\right)$ is the maximum experimental deflection evaluated at the tip of the trailing edge, while (j) is an index ranging over the locations of the trailing edges where the deflection is evaluated. At the end of the experiment, the measured percentage difference was lower than

4% for all three methods, demonstrating that the 3 methods have comparable accuracy even in the presence of unavoidable uncertainties related to the experimental activity. However, the modal method accuracy was achieved through a preliminary FE modal analysis that required knowledge of the material properties of the structure. Furthermore, even though Ko's method was able to provide the structure deflection in the same points where the strains are measured, the iFEM was much more flexible (no limitations on boundary conditions and on the points where the displacement is reconstructed) and it didn't require any data about material properties and applied loads.
In [10], Esposito and Gherlone apply Ko's displacements method, the modal method, and the iFEM to a composite wing box undergoing bending and twisting deformations. A detailed investigation into the optimal configuration of the strain sensors for all three techniques was carried out simultaneously, and the performance of the methods were compared in terms of reconstruction accuracy and the number of sensors required. The iFEM showed to be the most accurate in the wing-box vertical displacement reconstruction. Even though it was the most accurate method it also required a higher number of strain sensors. The modal method was able to compute the structure displacement with acceptable accuracy using fewer sensors. Ko's displacements theory was able to provide a rough estimate of the deformed shape by requiring very few sensors. To complete the comparison, it was verified that the use of more sensors for the Ko displacement theory and the modal method was ineffective or even detrimental to the performance of the methods. Thus, it was shown that even with the same number of sensors, the two methods could not reach the level of accuracy achieved by iFEM.

1.2 Image registration

Although contact instruments are suitable for many applications, they have a limited frequency response and can interfere with the dynamics of the measurement object. In addition, sensors such as strain gauges and accelerometers, although very accurate, deliver data only at the location where they have been positioned. Where these factors represent a problem, non-contact methods have advantages. Among the non-contact methods, there is image registration.
Image registration is the process of overlaying images of the same scene taken at different times, from different viewpoints, and/or by different sensors. One of the images is referred to as the *moving* or *source* and the others are referred to as the *target*, *fixed*, or *sensed images*. It's used in many fields, such as computer vision, military automatic target recognition, medicine, and remote sensing [11].
Depending on the imaging procedure, image registration methodology can be divided into four categories:

- *different viewpoints (multiview analysis)* - images of the scene are quired from different viewpoints.
- *different times (multitemporal analysis)* - images of the same scene are acquired at different times, possibly under different conditions.
- *different sensors (multimodal analysis)* - images of the same scene are acquired by different sensors.
- *scene to model registration* - images of a scene and a model of the scene are registered.

The development of one universal method applicable under all conditions is unrealistic due to the variability of the image registration task. Nevertheless, image registration algorithms can be classified into two categories:

- *area-based methods (ABM)*;
- *feature-based methods (FBM)*.

Area-based matching uses the gray value of the pixels to describe matching entities. In the area-based matching algorithms, a small window of pixels in the sensed image is compared statistically with windows of the same size as the reference image. Usually, the normalized cross-correlation or least-squares technique is used to measure the degree of match. The prerequisite of ABM is that the gray level distribution of the sensed image and reference image must be similar. Very good initial approximations are required to assure convergence. ABM methods are not well adapted to the problem of multisensor image registration since the gray-level characteristics of images to be matched can vary from sensor to sensor [12].
Feature-based matching techniques do not use gray values to describe matching entities but use image features derived by a feature extraction algorithm. These features include edges, contours, surfaces, corners, line intersections, points of high curvature, statistical features such as moment invariants or centroids, and higher-level structural and syntactic descriptions [13]. The form of the description as well as the type of features used for matching depends on the task to be solved.
Area-based methods are preferably applied when the images do have not many prominent details and the distinctive information is provided by gray levels/colors rather than by local shapes and structure [11]. On the other hand, feature-based matching methods are typically applied

when the local structural information is more significant than the information carried by the image intensities. They can handle complex between-image distortions. The crucial point of all feature-based matching methods is to have discriminative and robust feature descriptors that are invariant to all assumed differences between the images.
Compared with ABM, FBM is more robust and reliable. However, FBM often requires sophisticated image processing for feature extraction and depends on the robustness of feature detection for reliable matching. As a result, the image matching precision is not as high as that of ABM [12].

In the next sections, the functioning of the *Digital Image Correlation* (DIC) technique and diffusion process based on Thirion's demons method will be presented. The DIC is an area-based method and its use in the aerospace field is continuously growing. The diffusion-based registration methods belong to the non-rigid feature-based methods. Since the data fusion performed in this work relies on one of his algorithms, its working functioning will be explained.

1.2.1 Digital image correlation

Digital image correlation algorithms are based on the tracking of information across a set of images, taken from cameras, from the reference image to pictures taken later in the test. Through this information, it is possible to trace the displacement and/or strain undergone by the structure.
DIC is becoming a trusted instrument for measuring strain and deformation in aerospace testing thanks to its accuracy and versatility. DIC can measure the behavior of a large structural element, such as full-sized rocket sections, as well as microscopic structural elements, such as microscopic fibers. Furthermore, it can be used for both rapid loads such as mechanical shocks, and quasi-static loads lasting several hours. This can be achieved through a minimal experimental setup: one camera is sufficient to completely determine the 2D displacement field, while two are needed to determine the 3D one. In the following section, the DIC's operating principle for 2D displacement will be described.

Experimental setup

As mentioned before, the equipment required to perform DIC is minimal. In figures 1.2, the experimental setup for the standard application of DIC for determining the 2D displacement field is schematized,

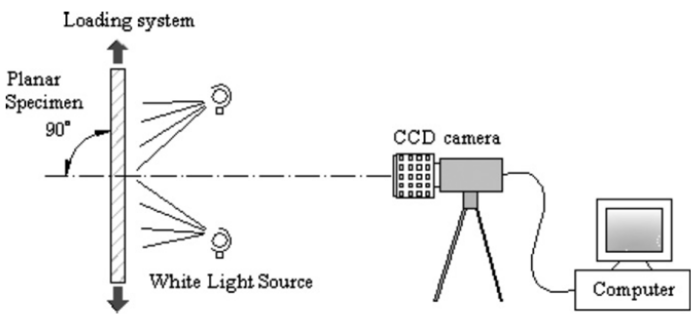

Figure 1.2: *DIC set up for 2D displacement [14]*

The surface of the specimen is illuminated by white light. The specimen surface must have a random gray intensity distribution which deforms together with the specimen surface as a carrier of deformation information. The speckle pattern can be the natural texture of the specimen surface or artificially made by spraying black and/or white paints, or other techniques. The camera is placed with its optical axis normal to the specimen surface. This implies that the charge-coupled device (CCD) sensor and the object surface should be parallel. It is of paramount importance that this condition remains verified throughout the acquisition so that out-of-plane movements are small enough to be overlooked. These could produce apparent deformations that would be added to those actually present and would be difficult to compensate for, with the effect of producing a measurement affected by an error [15]. The acquired images are processed using a computer program to obtain the desired displacement information.

Basic principles

In the routine implementation of the 2D DIC method, the definition of the region of interest (ROI) in the reference image should be specified first. The ROI is divided into evenly-spaced virtual grids, as shown in figure 1.3

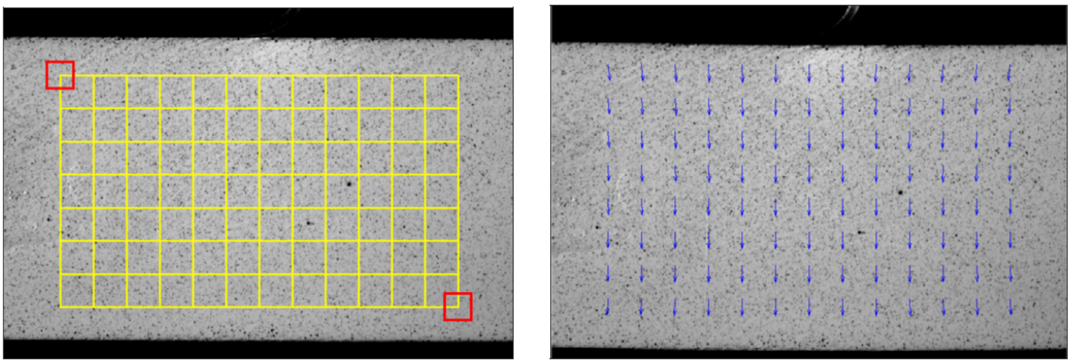

(a) Evenly-spaced virtual grids in yellow; the red squares are the subset used to compute the displacements of the grid nodes

(b) The blue arrow are the computed displacements of the grid nodes

Figure 1.3: *Example of an evenly-spaced virtual grid of the ROI [14]*

The displacements are computed at each point of the virtual grids to obtain the full-field deformation. The basic principle of 2D DIC is the matching of the same points (or pixels) between the two images recorded before and after deformation. It is therefore of primary importance to ensure a good correspondence between the points of the different images. It is immediately apparent that the use of a single pixel cannot ensure this condition, as the same grey level from which it is described in the reference image can be found several times within successive images, so unambiguousness is not guaranteed. For these reasons, the virtual subdivision of the reference image into small square areas called 'subsets' is introduced (red squares in figure 1.3). The subsets contain several pixels and therefore they are characterized by more information. It can be understood that if the surface whose displacement is to be calculated has no texture, each subset will be identical to the others and the method will not be able to find an unambiguous correspondence between a subset in the reference image and the corresponding one in the deformed one. But not only that, if ordered grids are applied to the surface, there remains the problem of non-uniqueness of subsets (aperture problem). Although a surface may have some natural texture, such as the presence of edges, rivets, or other, this is not enough to bypass the opening problem. The solution is to use a random pattern of points with sufficiently varied plots (called *speckle pattern*) to present subsets with unique characteristics within the ROI. An example of speckle patterns is shown in figure 1.4

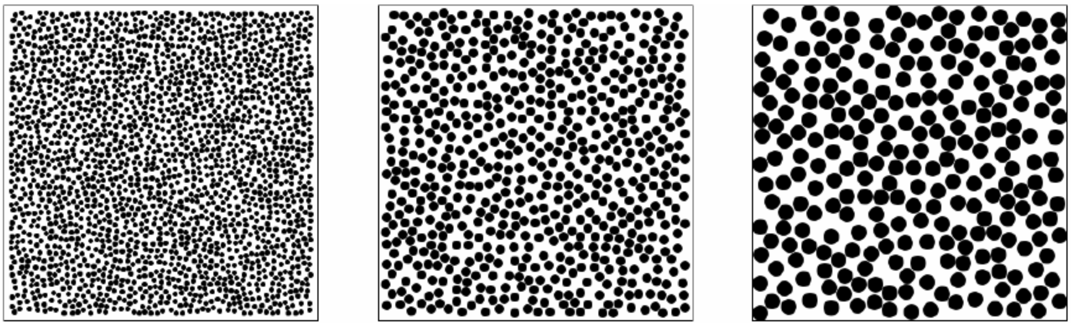

Figure 1.4: *Example of speckle patterns with different diameter sizes [16]*

Optimal patterns and subsets

Since the determination of the displacement field results in the search for subsets of the reference image in the deformed image, the importance of the use of a suitable speckle pattern is evident. As demonstrated in [17], the size of the subset (which is defined by the user), for a given speckle pattern, influences the accuracy with which displacements are determined. The main speckle pattern's features are:

- the *average size*, in terms of pixels, of the average diameter of the points constituting the speckle pattern; values recommended in the literature range from 5 px to 3 px [16, 18];
- the *coverage factor*, which is recommended to be between 40% and 70% [16];
- the *subset entropy*, for evaluating the differentiation of the intensity of the grey levels within the same subset: higher values of this lead to a lower standard deviation of the measurement [19].

In [19] it was shown how larger subsets characterized by a larger *subset entropy* reduce noise and grey intensity quantization during photographic acquisition, contributing to a decrease in the standard deviation of the displacements. On the other hand, deformation fields of small subsets can be accurately approximated by first- or second-order shape functions, whereas large subsets generally lead to large systematic approximation errors.
It follows from the above that the search for the optimal subset consists of a trade-off solution aimed at minimizing random and systematic errors.

Correlation criterion

A cross-correlation (CC) criterion or sum-squared difference (SSD) correlation criterion must be predefined to evaluate the similarity degree between the reference subset and the deformed subset. The matching procedure is completed by searching the peak position of the distribution of the correlation coefficient. Once the correlation coefficient extremum is detected, the position of the deformed subset is determined. The differences in the positions of the reference subset center and the target subset center yield the in-plane displacement vector. Let f be the reference image and g the deformed one, while (x_i, y_i) and (x'_i, y'_i) the coordinate in their reference system, the cross-correlation criterion and the sum-squared difference correlation criterion are defined, respectively as

$$C_{CC} = \sum_{i=-M}^{M} \sum_{j=-M}^{M} \left[f(x_i, y_j)\, g\left(x'_i, y'_j\right) \right] \tag{1.16}$$

$$C_{SSD} = \sum_{i=-M}^{M} \sum_{j=-M}^{M} \left[f(x_i, y_j) - g\left(x'_i, y'_j\right) \right]^2 \tag{1.17}$$

for a given subset of size $(2M + 1) \cdot (2M + 1)$. The parameters presented are sensitive to linear scaling and brightness variation, problems, especially the last one, which can easily arise during a standard test [14]. Consequently, their normalized versions (ZNCC – zero normalized cross-correlation and ZNSSD – zero normalized sum of squared differences) are preferred,

$$C_{ZNCC} = \sum_{i=-M}^{M} \sum_{j=-M}^{M} \left\{ \frac{[f(x_i, y_j) - f_m] \times \left[g(x'_i, y'_j) - g_m\right]}{\Delta f \Delta g} \right\} \tag{1.18}$$

$$C_{ZNSSD} = \sum_{i=-M}^{M} \sum_{j=-M}^{M} \left[\frac{f(x_i, y_j) - f_m}{\Delta f} - \frac{g(x'_i, y'_j) - g_m}{\Delta g} \right]^2 \tag{1.19}$$

where

$$f_m = \frac{1}{(2M+1)^2} \sum_{i=-M}^{M} \sum_{j=-M}^{M} f(x_i, y_i)\,; \quad g_m = \frac{1}{(2M+1)^2} \sum_{i=-M}^{M} \sum_{j=-M}^{M} g(x'_i, y'_i)$$

$$\Delta f = \sqrt{\sum_{i=-M}^{M} \sum_{j=-M}^{M} [f(x_i, y_i) - f_m]^2}; \quad \Delta g = \sqrt{\sum_{i=-M}^{M} \sum_{j=-M}^{M} [g(x'_i, y'_i) - g_m]^2}$$

Lastly, it is worth pointing out that these approaches, although different, are related to each other [20].

Shape functions

It must be considered that once the correspondence between the reference subset and the target subset has been found, as a result of the deformations undergone by the body under analysis, the reference subset may no longer be found to be undeformed (a condition that does not only occur for rigid displacements). It is therefore necessary to virtually deform the reference subset in order to find the best correspondence with the target subset. This induced deformation operation is carried out by means of the *shape functions*.

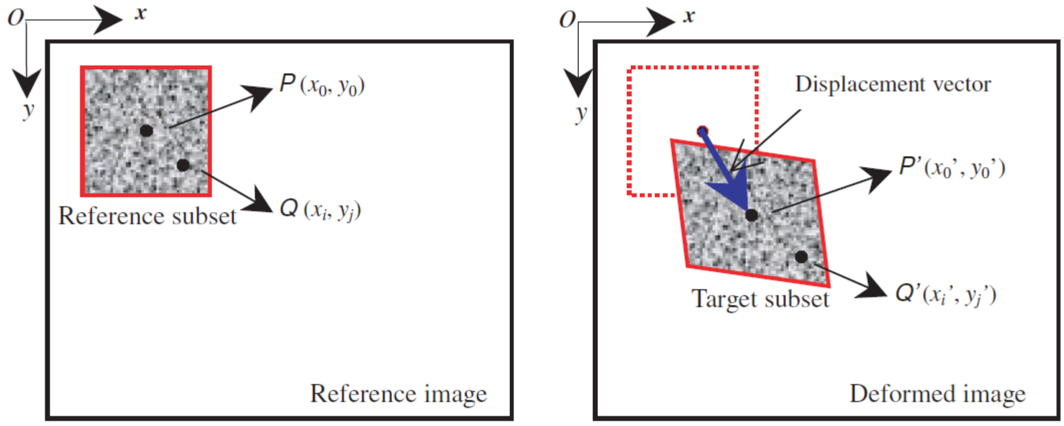

Figure 1.5: *Reference subset before and after the deformation [14]*

With reference to figure 1.5, the subset deformation induced by a shape function can be defined as:

$$\begin{aligned} x_i' &= x_i + \xi(x_i, y_j) \\ y_j' &= y_j + \eta(x_i, y_j) \end{aligned} \tag{1.20}$$

with $i, j = -M : M$. ξ and η are the analytical formulations of the shape functions [21]. The most used shape function that allows translation, rotation, shear, normal strains, and their combinations of the subset is the first-order shape function:

$$\xi_1(x_i, y_j) = u + u_x \Delta x + u_y \Delta y; \quad \eta_1(x_i, y_j) = v + v_x \Delta x + v_y \Delta y \tag{1.21}$$

where:

- $\Delta x = x_i - x_0$;
- $\Delta y = y_j - y_0$;
- u and v are are the $x-$ and $y-$ directional displacement components of the reference subset center, $P(x_0, y_0)$ (figure 1.5);
- u_x, u_y, v_x, v_y are the first-order displacement gradients of the reference subset.

Interpolation scheme

In general, after deformation, the reference subset may be located at non-integer pixel positions (i.e. subpixel positions). It is therefore necessary to apply the cross-correlation or error-minimization operation to non-integer positions, but to do so first requires an interpolation of the intensity of the subset is required. Several sub-pixel interpolation schemes have been used in the literature. However, a high-order interpolation scheme (e.g. bicubic spline interpolation or bicubic spline interpolation) is highly recommended as it provides higher registration accuracy and better algorithm convergence than simple interpolation schemes [22].

Displacement field calculation

While the calculation of displacement with 1-pixel accuracy is easily achievable due to the discrete nature of digital images, obtaining displacement with sub-pixel accuracy requires ad-hoc algorithms [23]. These algorithms need an accurate initial estimate of the displacement in order to work. In the case of small displacements, the initial displacement estimate can be determined with an accurate pixel-by-pixel search routine performed within the range specified in the deformed image. An alternative procedure consists of comparing the subsets of the reference image and the deformed image in the Fourier domain: here the correlation is calculated by means of the complex product between the Fourier spectrum of the first subset and the complex conjugate of the spectrum of the second subset. This method is particularly fast, but unfortunately only suitable for small displacements [14].

1.2.2 Image matching - Thirion Diffusion process

Thirion's Demons algorithm estimates non-rigid deformations by successively estimating force vectors that drive the deformation toward alignment, and then smoothing the force vectors by convolution with a Gaussian kernel.
The main idea behind this method is to consider the contours of the reference image (fixed image) as semi-permeable membranes. The other image (moving image), which is considered a deformable grid pattern, is able to diffuse into these interfaces through the action of effectors (demons) located within [24].
In order to be able to define Thirion's method, the optical flow method is briefly presented.

Optical flow equation

The optical flow method allows the computation of pixels velocity/displacement by comparing two temporal sequences images. In an image, each pixel has a brightness value associated with it: let s and m be the intensity brightness values of image S and M respectively. One of the widely used assumptions along the optical flow methods is to consider the intensity of the image constant in time. For small displacements, this hypothesis leads to the following equation

$$\vec{v} \cdot \vec{\nabla} s = m - s \tag{1.22}$$

where $\vec{v}$ is the velocity. Since the velocity is expressed as $\frac{\text{pixel}}{\text{frame}}$, it is considered a displacement in this application.

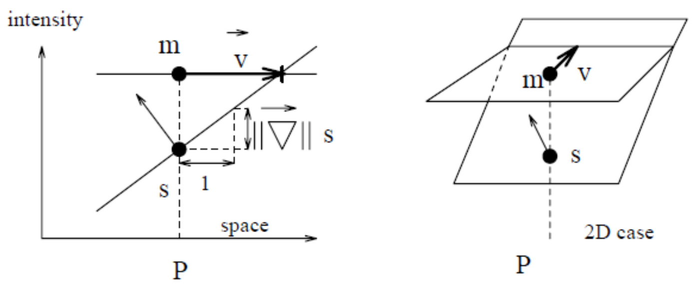

Figure 1.6: *Instantaneous velocity from image M to image S [24]*

Since there are two unknowns and one equation, another constraint is necessary. One possible solution is to consider the end point of $\vec{v}$ as the closest point of the hypersurface m, with respect to spatial (x, y, z) translations, which lead to equation

$$\vec{v} = \frac{(m - s)\,\vec{\nabla} s}{\left(\vec{\nabla} s\right)^2} \tag{1.23}$$

Since small values of $\vec{\nabla} s$ lead to high number of $\vec{v}$, the equation 1.23 is multiplyed by $\frac{\left(\vec{\nabla} s\right)^2}{\left(\left(\vec{\nabla} s\right)^2 + (m-s)^2\right)}$, leading to

$$\vec{v} = \frac{(m-s)\,\vec{\nabla} s}{\left(\vec{\nabla} s\right)^2 + (m-s)^2} \tag{1.24}$$

or to

$$\vec{v} = 0 \text{ if } \left(\vec{\nabla} s\right)^2 + (m-s)^2 < \epsilon$$

With this expression, the optical flow can be calculated in two steps:

1. compute the instantaneous optical flow for every point in S;
2. regularize the deformation field.

Matching methods using demons

Let M be the moving image, and S be the target image. It's assumed that the contour O of the scene image S is a membrane, and demons are scattered along O. It is assumed also that for every point of the contour O, the vector perpendicular to it and oriented from the inside of the object to the outside are determined.

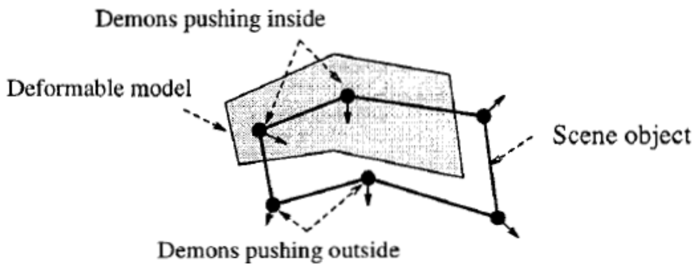

Figure 1.7: *Deformable model with demons (2D case) [25]*

M contains a deformed version $T^{-1}(O)$ of the contour O, and T is the transformation to be recovered from M to S. Different permitted deformations T can be imposed, from totally rigid to totally free.
It's assumed to know how to determine, for each point P of M, if it is *inside* or *outside* the shape $T^{-1}(O)$. The demons, scattered along O, act locally to push the model M inside O if the corresponding point of M is labeled *inside*, and outside O if it is labeled *outside*. To determine if a point P is inside or outside the shape $T^{-1}(O)$, the *iso-contours* are used. Through each point P of S where a $\vec{\nabla} s \neq 0$ goes an iso-contour $s = I$, where $I = s(P)$ is constant. This iso-contour is the interface between the *inside* regions $s < I$ and the *outside* regions s $> I$. The intensities comparison of the model M with I gives an automatic way to label the points of M as inside or as outside. $\vec{v}$ (equation 1.24) is similar to an elementary force that pushes the point P of M, along the same direction of $\vec{\nabla} s$, toward the outside (orientation in agreement with $\vec{\nabla} s$) if $m > I$, and toward the inside (orientation in agreement with $-\vec{\nabla} s$) if $m < I$. This is due to the assumption $s = m$.

In order to work, an iterative algorithm is necessary. The transformation T to be recovered from

M to S is the final transformation of a series of successive transformations $\{T_0, T_1, ..., T_i, ...\} \subset$ **T**. The space of deformations **T** can be rigid, affine, free form, etc. At each step, the deformed version $T_i(M)$ of the image M becomes $T_{i+1}(M)$. This transformation is driven by the internal forces f_{int} created by the relationships between the model points, and the external forces f_{ext} created by the interactions between M and $T_i^{-1}(S)$. The generic iterative scheme is illustrated in figure 1.8.

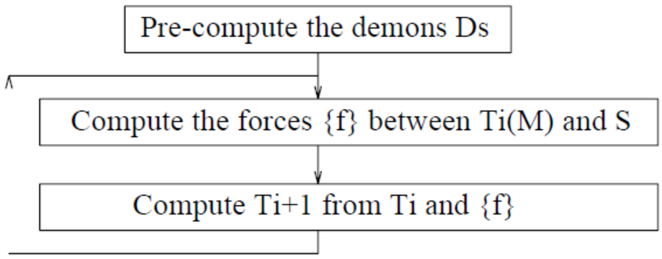

Figure 1.8: *Iterative scheme [24]*

The first step is the determination of the set of demons D_S from S: note that this selection occurs only once (the demons are external to the loop). The next two steps constitute the iterative scheme necessary to determine the final transformation T.

Demons D_S extraction

The definition of the set of demons D_S from S can be done in different ways. D_S can be all the points of the contour O, the whole grid (one demon per pixel) of S or D_S can be defined according to the segmentation of images M and S (in which case the nature of the problem changes). Each demon carries a piece of information, which can be:

- its position P in S (possibly sub-pixel);
- its intensity $s(P)$;
- its direction $s(P)$ oriented from inside to outside.

It is important to emphasize that the demon force is not limited to that provided by the optical flow. Generally, the fewer demons in the image, the more sophisticated the definition of their force can be.

Iterative part

The first step is to define an initial deformation T_0, which can be the identity transformation. After that, for each step, the internal and external forces have to be determined in order to compute the next transformation T_1. The generic iteration i consists of:

1. the determination of the elementary demon force $\vec{f_i}(P)$ for each demon $P \in D_S$;
2. the computation of the subsequent transformation T_{i+1} from T_i and the elementary demons forces.

Pyramidal iteration scheme

In the case where each pixel is a demon, the computational cost may be too onerous. This is why generally, a multi-scale scheme is adopted: a large number of iterations are performed at a low scale (coarse scale) down to a few iterations when the scale is very fine. The total calculation time will be equivalent to that of the finest scale. Gaussian smoothing is adopted to change the resolution of the scale. The effect of the Gaussian filter is similar to the average filter, with the difference that the average is not a 'net' average, but a weighted average that gives more importance to the central pixel and less and less importance as it moves away from it. For this reason, this method provides a better smoothness and preserves the edges better.

2 Formulation of the beam inverse finite element

As there are different inverse finite element algorithms that differ not only according to the developers but also according to the structure to be discretized, since the beam is the structural element that is the subject of this thesis, the formulation of the inverse finite element beam is presented. For the purpose of this thesis, iFEM formulations for the Timoshenko beam and the Bernoulli-Euler beam are presented.

2.1 Timoshenko beam element

Consider a straight isotropic beam, with a circular cross-section, Young modulus E, shear modulus G e Poisson coefficient ν [26]. The used reference system $0\,(x, y, z)$ is shown in figure 2.1.

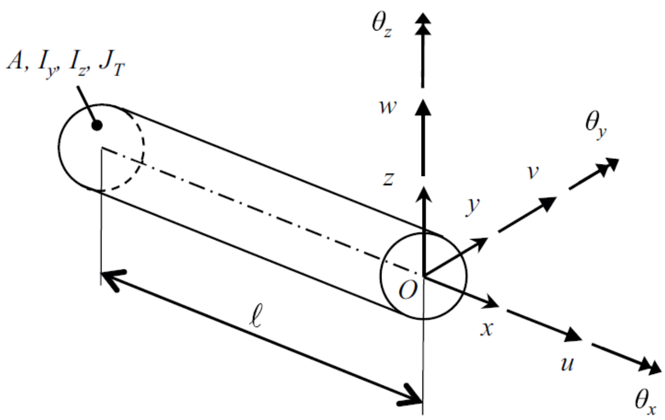

Figure 2.1: *Beam reference system* $0\,(x, y, z)$ *[26]*

Let ℓ be the frame member length, A the area of the beam cross section, I_y and I_z the moment of inertia of the cross section along the y and z axes respectively, J_T the torsion constant. The x axis coincides with the center of gravity and the shear center, while y and z are the principal axes of inertia. The following formulation neglects the axial warping due to torsion. The resulting displacement field is

$$
\begin{aligned}
u_x(x,y,z) &= u(x) + z\theta_y(x) - y\theta_z(x) \\
u_y(x,y,z) &= v(x) - z\theta_x(x) \\
u_z(x,y,z) &= w(x) + y\theta_x(x)
\end{aligned} \tag{2.1}
$$

where:

- u_x, u_y and u_z are the displacements along the axes x, y and z respectively;
- u, v e w are the shear center displacements;
- θ_x, θ_y and θ_z are the rotation along the tre axes.

The kinematic variables $\mathbf{u} \equiv [u, v, w, \theta_x, \theta_y, \theta_z]^T$ and their positive guidelines are shown in the figure 2.1. By using the geometric relationships the following linear deformations are obtained:

$$
\begin{aligned}
\varepsilon_x(x,y,z) &= e_1(x) + ze_2(x) + ye_3(x) \\
\gamma_{xz}(x,y) &= e_4(x) + ye_6(x) \\
\gamma_{xy}(x,z) &= e_5(x) - ze_6(x)
\end{aligned} \tag{2.2}
$$

where the following notation has been used:

$$
\begin{aligned}
e_1(x) &\equiv u_{,x}(x) \\
e_2(x) &\equiv \theta_{y,x}(x) \\
e_3(x) &\equiv -\theta_{z,x}(x) \\
e_4(x) &\equiv w_{,x}(x) + \theta_y(x) \\
e_5(x) &\equiv v_{,x}(x) - \theta_z(x) \\
e_6(x) &\equiv \theta_{x,x}(x)
\end{aligned} \tag{2.3}
$$

The iFEM reconstructs the deformed structural shape by minimizing the weighted least squares functional $\mathbf{\Phi}$ containing the section strains obtained through in situ strain measurements, $\mathbf{e}^{\varepsilon}$, and $\mathbf{e(u)}$ defined by equations 2.3, i.e.,

$$
\mathbf{\Phi} = ||\mathbf{e(u)} - \mathbf{e}^{\varepsilon}||^2 \tag{2.4}
$$

The kinematic variables $\mathbf{u}$ are subsequently discretized with finite elements based on shape functions $\mathbf{N}(x)$ with C^0 continuity,

$$
\mathbf{u}(x) \simeq \mathbf{u}^e(x) = \mathbf{N}(x)\mathbf{q}^e \tag{2.5}
$$

where $\mathbf{q}^e$ denotes the nodal degree of freedom (DOF) of the element. Consequently, the functional total is the sum of the N contributions of the individual elements:

$$\Phi = \sum_{e=1}^{N} \Phi^e \tag{2.6}$$

Taking into account the axial stretching, the bending, the twisting, and the transverse shearing, the element functional Φ^e is given by the scalar product of the weighting coefficients vector $\mathbf{w}^e \equiv \{w_k^e\} = \{w_1^0, w_2^0 \left(\frac{I_y^e}{A^e}\right), w_3^0 \left(\frac{I_z^e}{A^e}\right), w_4^0, w_5^0, w_6^0 \left(\frac{J_T^e}{A^e}\right)\}$ and the vector of least-squares components $\mathbf{\Phi}^e \equiv \{\Phi_k^e\}, \quad (k = 1, ..., 6)$,

$$\Phi^e \left(\mathbf{u}^e, \mathbf{e}^\varepsilon\right) \equiv \sum_{k=1}^{6} w_k^e \Phi_k^e = \mathbf{w}\Phi \tag{2.7}$$

where:

- $w_k^0 \; (k = 1, ..., 6)$ denotes the adimensional weighting coefficients;
- A^e, I_y^e, I_z^e, and J_T^e are, respectively, the cross-section area, the inertia moments along y and z axis, and the torsion constant of the element cross-section.

Different values can be assigned to the coefficient w_k^0 in order to impose a stronger or weaker correlation between the measured section-strain components and their analytical counterparts. A higher value of w_k^0 imposes a stronger correlation and vice versa. The values w_k^0 are 1 for all the inverse elements that have a strain sensor, while they are equal to 10^{-4} for the inverse element without strain data.
The six element functional components are given in Euclidean norm

$$\Phi_k^e \equiv \frac{\ell^e}{n} \sum_{i=1}^{n} \left[e_{k(i)}(\mathbf{u}^e) - e_{k(i)}^\varepsilon\right]^2 \quad (k = 1, ..., 6) \tag{2.8}$$

where ℓ^e is the element length, n is the number of positions where the section strains are evaluated; $e_{k(i)}^\varepsilon$ is the kth section strain computed from the strains measured at x_i; $e_{k(i)}$ indicates the kth section strain interpolated within the element and evaluated at the same location. By combing the equations 2.3 and 2.5, the analytic element level section strains $\mathbf{e}(\mathbf{u}^e)$ are expressed in matrix form as

$$\mathbf{e}(\mathbf{u}^e) = \mathbf{B}\left(x\right) \mathbf{q}^e \tag{2.9}$$

where the $\mathbf{B}\left(x\right)$ matrix contains the derivatives of the shape functions $\mathbf{N}\left(x\right)$. By substituting equation 2.9 into equation 2.8 and then in equation 2.7, the following quadratic form is obtained

$$\Phi^e = \frac{1}{2} \left(\mathbf{q}^e\right)^T \mathbf{k}^e \mathbf{q}^e - \left(\mathbf{q}^e\right)^T \mathbf{f}^e + \mathbf{c}^e \tag{2.10}$$

where $\mathbf{c}^e$ is a constant while $\mathbf{k}^e$ and $\mathbf{f}^e$ are defined as follows

$$\mathbf{k}^e = \sum_{k=1}^{6} w_k \mathbf{k}_k^e, \quad \mathbf{f}^e = \sum_{k=1}^{6} w_k \mathbf{f}_k^e \tag{2.11}$$

with

$$\mathbf{k}_k^e \equiv \frac{L^e}{n} \sum_{i=1}^{n} \left[\mathbf{B}_k^T(x_i)\, \mathbf{B}_k(x_i) \right], \quad \mathbf{f}_k^e \equiv \frac{L^e}{n} \sum_{i=1}^{n} \left[\mathbf{B}_k^T(x_i)\, e_k^{\varepsilon i} \right] \quad (k = 1, ..., 6) \tag{2.12}$$

Note that $\mathbf{k}^e$ resembles the stiffness matrix of an element in the direct finite element method and that $\mathbf{f}^e$ resembles the load's vector. $\mathbf{k}^e$ depends from the measure points locations, x_i, and their number n, while $\mathbf{f}^e$ depends from the measured strain values [27]. By minimising the element functional $\mathbf{\Phi}^e$ with respect to $\mathbf{q}^e$, the matrix element results in the equation $\mathbf{k}^e\mathbf{q}^e = \mathbf{f}^e$. Assembling the contributions of the finite elements, taking into account the appropriate coordinate transformations, and specifying the problem-dependent displacement boundary conditions, results in a system of non-singular algebraic equations of the form

$$\mathbf{K}\mathbf{q} = \mathbf{F} \tag{2.13}$$

where $\mathbf{K}$ is a non-singular system matrix provided that at least a minimum number of strain gauges, $n = n_{min}$, is used, i.e. $n_{min} = 1$ and 2, respectively, for constant and linearly distributed strains of the element section [26]. The solutions of the equation 2.13 for the displacement degrees of freedom, $\mathbf{q}$, are efficient. The matrix $\mathbf{K}$ is inverted only once because it remains unchanged for a given distribution of strain sensors and is independent of the measured strain values. The vector $\mathbf{F}$, however, depends on the measured strain values; therefore, with each update of the strain measurement during deformation, the matrix-vector multiplication, $\mathbf{K}^{-1}\mathbf{F}$, gives rise to the vector of unknown degrees of freedom, $\mathbf{q}$.

For the structural elements of the frame loaded only by forces and moments at the free end, it can be shown that the section strains show the following distribution: e_1, e_4, e_5 and e_6 are constant, while e_2 and e_3 are linear [27]. It follows from the equation 2.3 that u and θ_x are linear, θ_y and θ_z parabolic, v and w cubic. Thus, the following interpolations are adopted,

$$\begin{aligned}
u(x) &= \sum_{i=1,2} L_i^{(1)}(x)\, u_i \\
\theta_x(x) &= \sum_{i=1,2} L_i^{(1)}(x)\, \theta_{xi} \\
\theta_y(x) &= \sum_{j=1,r,2} L_j^{(2)}(x)\, \theta_{yj} \\
\theta_z(x) &= \sum_{j=1,r,2} L_j^{(2)}(x)\, \theta_{zj} \\
v(x) &= \sum_{i=1,2} L_i^{(1)}(x)\, v_i - \sum_{j=1,r,2} N_j^{(3)}(x)\, \theta_{zj} \\
w(x) &= \sum_{i=1,2} L_i^{(1)}(x)\, w_i + \sum_{j=1,r,2} N_j^{(3)}(x)\, \theta_{yj}
\end{aligned} \tag{2.14}$$

where the subscripts $1, r$ and 2 denote, respectively, the positions along the length of the beam at the left-end, middle, and right end of the node (see figure 2.2).

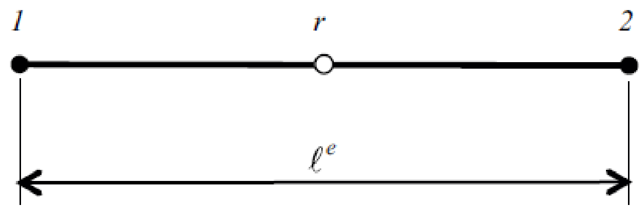

Figure 2.2: *Beam inverse finite element geometry and nodes [26]*

$L_i^{(1)}(x)\,(i=1,2)$ are linear Lagrange polynomials; $L_j^{(2)}(x)\,(j=1,r,2)$ are quadratic Lagrange polynomials. The cubic polynomials $N_j^{(3)}(x)\,(j=1,r,2)$ are obtained from standard cubic Lagrange polynomials by forcing the transverse shear deformations of the section (e_4 and e_5) to be constant along the element. The L_i, L_j, N_j expression are reported in appendix A. The inverse beam element has 14 degrees of freedom: 6 at each end node plus 2 rotations θ_{yr} and θ_{zr} at the mid-span. By solving the equation system of the element $\mathbf{k}^e\mathbf{q}^e = \mathbf{f}^e$ exactly with respect to the external DOFs, the two internal rotational degrees of freedom are condensed, resulting in a topology of elements with two nodes/twelve degrees of freedom.

2.1.1 Estimating strain measures

In order to implement iFEM, it is necessary to calculate the six sectional strain measurements of the beam (equation 2.3). These measures are calculated using the experimental linear strain measurements made on the surface of the beam. The calculation of the strain measurements depends on the beam cross-section: here, the procedure valid for any type of cross-section is given [28]. To this end, consider a prismatic beam with a generic cross-section, subjected to axial, transverse, and torsional loads at the free end. Figure 2.3 shows the generic airfoil-shaped beam with its reference system (figure 2.3(a)), the coordinate c that originates at the trailing edge of the profile (figure 2.3(b)), and a strain gauge measuring the generic strain, ε^*, placed on the surface of the beam with orientation β with respect to the x longitudinal axis of the beam (figure 2.3(c)).

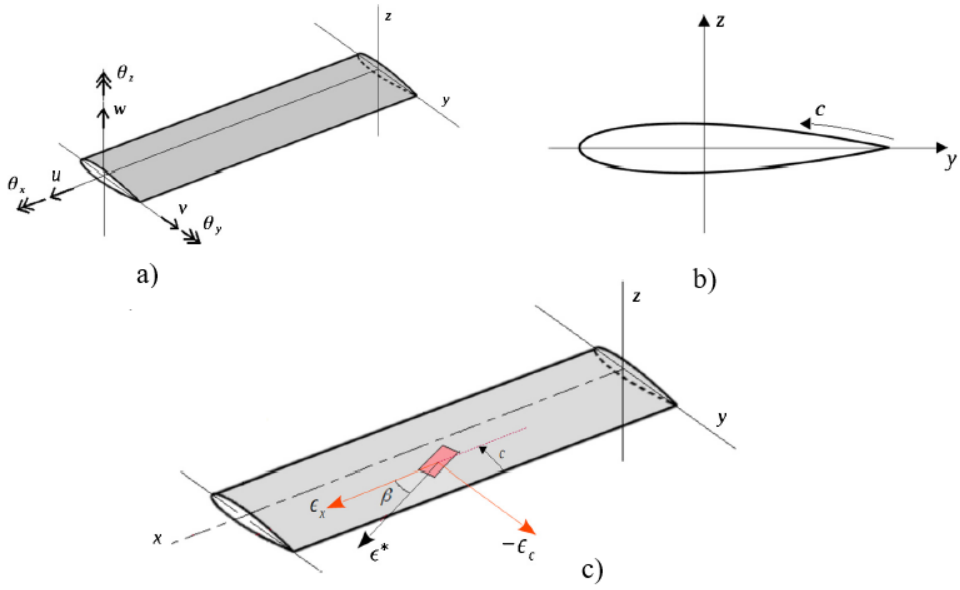

Figure 2.3: *(a) Beam geometry and kinematic variables, (b) beam cross section with the parameter c indicating the distance along the perimeter, (c) strain gauge placed on the surface of the beam, oriented at an angle β with respect to the axis of the beam [28]*

The strain intensity, ε^*, can be expressed in terms of the axial strain, ε_x, the tangential strain ε_c, and the tangential shear strain, γ_{xc}, on the perimeter of the beam section. Using a compatible strain-tensor transformation, this strain can be expressed as [27],

$$\varepsilon^* (x, c, \beta) = \varepsilon_x (x, c) \cos^2 \beta + \varepsilon_c (x, c) \sin^2 \beta + \gamma_{xc} (x, c) \cos \beta \sin \beta \tag{2.15}$$

Equation 2.15 can be further simplified [27],

$$\varepsilon^* (x, c, \beta) = \varepsilon_x (x, c) \left(\cos^2 \beta - \nu \sin^2 \beta \right) + \gamma_{xc} (x, c) \cos \beta \sin \beta \tag{2.16}$$

The axial strain, $\varepsilon_x (x, c)$ and the tangential shear strain, $\gamma_{xc} (x, c)$ shoul be rapresented in terms of the strain measures. The axial strain, $\varepsilon_x (x, c)$, can be expressed as,

$$\varepsilon_x (x, c) = e_1 (x) + e_2 (x) z (c) + e_3 (x) y (c) \tag{2.17}$$

The tangential shear strain $\gamma_{xc} (x, c)$ can be expressed as the superposition of strains due to transverse and torsional loads. If the beam is subjected to transverse or torsional loads, the shear strain is not constant over the beam section, but changes depending on the coordinate c. The variation of the tangential shear strain due to a transverse load acting along the z-axis can be expressed by the product of the shear strain variation function, $f_1 (c)$, and the maximum tangential shear strain, $\gamma^z_{xc,max}$, which represents the magnitude of the variation. Similarly, the variation in tangential shear strain due to a transverse load acting along the y-axis can be expressed by the product of the shear strain variation function, $f_2 (c)$, and the maximum tangential

shear strain, $\gamma^{y}_{xc,max}$, representing the intensity of the variation.
In the case of torsional loads acting at the tip of the beam, the variation of the tangential shear strain is expressed as the product of the torsional strain measure, e_6, and the function $f_3\left(c\right)$, which represents the variation of the tangential shear strain associated with a unit degree of torsion ($e_6 = 1$).
Through the superposition of effects, the total change in tangential shear strain γ_{xc} can be expressed as,

$$\gamma_{xc}\left(x,c\right) = \gamma^{z}_{xc,max}\left(x\right) f_1\left(c\right) + \gamma^{y}_{xc,max}\left(x\right) f_2\left(c\right) + e_6\left(x\right) f_3\left(c\right) \tag{2.18}$$

A very important aspect concerns the way in which it is possible to relate the maximum tangential shear strains, $\{\gamma^{y}_{xc,max}, \gamma^{z}_{xc,max}\}$, which are measured experimentally, with the cross-sectional strain measurements, $\{e_4, e_5\}$, which are based on the Timoshenko beam theory. In fact, while the 3D beam predicts that transverse shear strains vary along the cross-section, the Timoshenko beam assumes that these strains are constant for each cross-section. To relate these strains, in the case of the cantilever beam loaded at the free end with a load directed towards the z-axis, the shear strain energy per unit length in the mid-beam cross-section (to avoid end effects) of the 3D beam is equated with a similar case for the Timoshenko beam. For the Timoshenko beam, the shear strain energy per unit length, ϕ^{Tim}_{SE}, is the same for each section of the beam. In the present case, ϕ^{Tim}_{SE} can be defined as,

$$\phi^{Tim}_{SE} = \frac{F_z^2}{2AG} \tag{2.19}$$

The two shear strain energies can be equalized using a coefficient, k_{tz}, the classical shear correction factor, defined as the ratio between the two quantities,

$$k_{tz} = \frac{\phi^{Tim}_{SE}}{\phi^{FE}_{SE}} = \frac{F_z^2}{2AG\phi^{FE}_{SE}} = \frac{F_z/GA}{e_4} \tag{2.20}$$

where ϕ^{FE}_{SE} is the shear strain energy calculated using a high-fidelity 3D finite element model.
The coefficient, k_{ty}, is calculated similarly in the case where the load is applied along the y axis,

$$k_{ty} = \frac{\phi^{Tim}_{SE}}{\phi^{FE}_{SE}} = \frac{F_y^2}{2AG\phi^{FE}_{SE}} = \frac{F_y/GA}{e_5} \tag{2.21}$$

It is now possible to relate $\{e_4, e_5\}$ with $\{\gamma^{y}_{xc,max}\, \gamma^{z}_{xc,max}\}$, using the coefficients $\{k_{\varepsilon y}, k_{\varepsilon z}\}$, defined as the ratio between the two,,

$$\begin{aligned} k_{\varepsilon z} &= \frac{e_4}{\gamma^{z}_{xc,max}} = \frac{F_z/GA}{k_{tz}\gamma^{z}_{xc,max}} \\ k_{\varepsilon y} &= \frac{e_5}{\gamma^{y}_{xc,max}} = \frac{F_y/GA}{k_{ty}\gamma^{y}_{xc,max}} \end{aligned} \tag{2.22}$$

The coefficients $\{k_{ty}, k_{\varepsilon y}, k_{tz}, k_{\varepsilon z}\}$ are a function only of the shape of the beam section. It is now possible to express the tangential shear strain along the perimeter of the beam in terms of the shear coefficients as,

$$\gamma_{xc}(x,c) = \frac{1}{k_{\varepsilon z}} e_4(x) f_1(c) + \frac{1}{k_{\varepsilon y}} e_5(x) f_2(c) + e_6(x) f_3(c) \tag{2.23}$$

Finally, by substituting the equations 2.17 and 2.23 into the equation 2.16, it is possible to express the experimental strain measurements as a function of the section strain measurements,

$$\begin{aligned} \varepsilon^*(x,c,\beta) &= (e_1(x) + e_2(x) z(c) + e_3(x) y(c)) \left[\cos^2\beta - \nu \sin^2\beta\right] + \\ &+ \left(\frac{1}{k_{\varepsilon z}} e_4(x) f_1(c) + \frac{1}{k_{\varepsilon y}} e_5(x) f_2(c) + e_6(x) f_3(c)\right) \cos\beta \sin\beta \end{aligned} \tag{2.24}$$

The equation 2.24 constitutes an algebraic linear equation with six unknowns, so it requires six experimental strain measurements referring to the same cross-section for its resolution.

2.2 Bernoulli-Euler beam element

Consider a straight isotropic beam with Young modulus E, shear modulus G e Poisson coefficient ν [29]. The beam has a rectangular cross-section and the used reference system (x, y, z) is shown in figure 2.4.

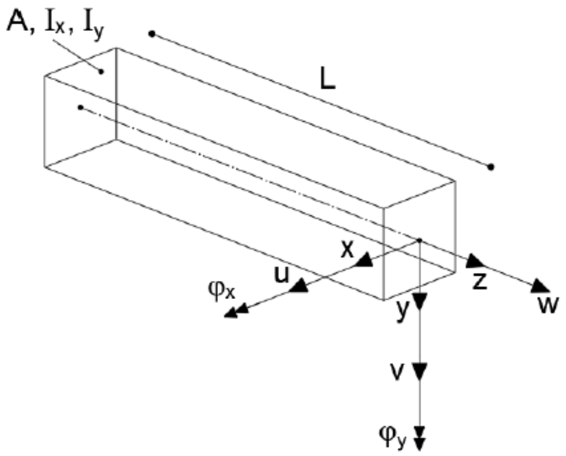

Figure 2.4: *Beam reference system* (x, y, z) *[29]*

Let L be the frame member length, A the area of the beam cross section, I_y and I_x the moment of inertia of the cross section along the y and x axes respectively. The x axis coincides with the center of gravity and the shear center, while y and z are the principal axes of inertia. The following formulation neglects the axial warping due to torsion. The resulting displacement field is

$$
\begin{aligned}
u_z(x,y,z) &= w(z) + y\phi_x(z) - x\phi_y(z) \\
u_y(x,y,z) &= v(z) \\
u_x(x,y,z) &= u(z)
\end{aligned}
\tag{2.25}
$$

where:

- u_x, u_y and u_z are the displacements along the axes x, y and z respectively;
- w, v e u are the shear center displacements;
- ϕ_x and ϕ_y are the rotation around the x and y axis, repsectively.

The kinematic variables $\mathbf{u} = [w, v, \phi_x, u, \phi_y]^T$ and their positive guidelines are shown in figure 2.4. By using the geometric relationships the following linear strains are obtained:

$$
\begin{aligned}
\varepsilon_z(x,y,z) &= w_{,z}(z) + y\phi_{x,z}(z) - x\phi_{y,z}(z) \\
\gamma_{zx}(z) &= u_{,z}(z) - \phi_y(z) = 0 \\
\gamma_{zy}(z) &= v_{,z}(z) + \phi_x(z) = 0
\end{aligned}
\tag{2.26}
$$

The transverse shear strains are zero, in accordance with the Bernoulli-Euler theory which predicts that the deformed beam sections remain flat and orthogonal to the beam axis.
The axial strain, ε_{z0}, and the two curvatures χ_x and χ_y referring to the x and y axes respectively, are introduced,

$$
\begin{aligned}
\varepsilon_{z0} &\equiv \frac{dw}{dz} \\
\chi_x &\equiv \phi_{x,z} = -\frac{d^2v}{dz^2} \\
\chi_y &\equiv \phi_{y,z} = \frac{d^2u}{dz^2}
\end{aligned}
\tag{2.27}
$$

The axial strain component, $\varepsilon_z(x,y,z)$, can be expressed as a function of sectional strains $\mathbf{e(u)} = \{\varepsilon_{z0}, \chi_x, \chi_y\}^T$, as

$$
\varepsilon_z(x,y,z) = \varepsilon_{z0}(z) + y\chi_z(z) - x\chi_y(z)
\tag{2.28}
$$

Similarly to the Timoshenko beam element, the iFEM reconstructs the deformed structural shape by minimizing the weighted least squares functional $\mathbf{\Phi}$ containing the section strains obtained through in situ strain measurements, $\mathbf{e}^{\varepsilon}$, and $\mathbf{e(u)}$, defined by equations 2.27 i.e.,

$$
\mathbf{\Phi}(\mathbf{u}) = ||\mathbf{e(u)} - \mathbf{e}^{\varepsilon}||^2
\tag{2.29}
$$

The kinematic variables $\mathbf{u}$ are subsequently discretized with finite elements based on shape functions $\mathbf{N}(x)$ of degree consistent with the behaviour of the beam,

$$\mathbf{u}(z) \simeq \mathbf{u}^e(z) = \mathbf{N}(z)\mathbf{q}^e \tag{2.30}$$

where $\mathbf{q}^e$ denotes the nodal degree of freedom (DOF) of the element. Consequently, the functional total is the sum of the N contributions of the individual elements:

$$\Phi = \sum_{e=1}^{N} \Phi^e \tag{2.31}$$

Taking into account the axial stretching and the two curvatures, the element functional Φ^e to be minimized is defined as,

$$\begin{aligned}
\Phi^e_{\varepsilon z} &\equiv \frac{l^e}{n}\sum_{i=1}^{n}\left(\varepsilon_{z0}(z_i) - \varepsilon^{\varepsilon}_{zo_i}\right)^2 \\
\Phi^e_{\chi x} &\equiv \frac{I^e_x l^e}{A^e n}\sum_{i=1}^{n}\left(\chi_x(z_i) - \chi^{\varepsilon}_{x_i}\right)^2 \\
\Phi^e_{\chi y} &\equiv \frac{I^e_y l^e}{A^e n}\sum_{i=1}^{n}\left(\chi_y(z_i) - \chi^{\varepsilon}_{y_i}\right)^2
\end{aligned} \tag{2.32}$$

where:

- n is the number of the axial locations where the section strains are evaluated, with coordinates z_i $(0 \leq z_i \leq l^e)$;
- l^e, A^e, I^e_x and I^e_y are, respectively, the length of the element, the area, and the inertia moments with respect to the x and y axes of the section, respectively.

By combing the equations 2.27 and 2.30, the analytic element level section strains $\mathbf{e}(\mathbf{u}^e)$ are expressed in matrix form as

$$\mathbf{e}(\mathbf{u}^e) = \mathbf{B}(z)\,\mathbf{q}^e \tag{2.33}$$

where the $\mathbf{B}(z)$ matrix contains the derivatives of the shape functions $\mathbf{N}(z)$. By substituting equation 2.33 into equation 2.32 and then adding all the contributions, the following form is obtained

$$\frac{\mathbf{\Phi}^e}{2} = \frac{1}{2}(\mathbf{q}^e)^T\mathbf{k}^e\mathbf{q}^e - (\mathbf{q}^e)^T\{\mathbf{f}^e\} + c \tag{2.34}$$

where $\mathbf{k}^e$ is the sum of

$$
\begin{aligned}
\mathbf{k}^e_{\varepsilon_z} &= \frac{l^e}{n}\sum_{i=1}^{n}\left[\mathbf{B}^T_{\varepsilon_z}(z_i)\,\mathbf{B}_{\varepsilon_z}(z_i)\right] \\
\mathbf{k}^e_{\chi x} &= \frac{I^e_x l^e}{A^e n}\sum_{i=1}^{n}\left[\mathbf{B}^T_{\chi x}(z_i)\,\mathbf{B}_{\chi z}(z_i)\right] \\
\mathbf{k}^e_{\chi y} &= \frac{I^e_y l^e}{A^e n}\sum_{i=1}^{n}\left[\mathbf{B}^T_{\chi y}(z_i)\,\mathbf{B}_{\chi y}(z_i)\right]
\end{aligned} \tag{2.35}
$$

and $\mathbf{f}^e$ is the sum of

$$
\begin{aligned}
\mathbf{f}^e_{\varepsilon_z} &= \frac{l^e}{n}\sum_{i=1}^{n}\left[\mathbf{B}^T_{\varepsilon_z}(z_i)\,\varepsilon^{\varepsilon}_{zo_i}\right] \\
\mathbf{f}^e_{\chi z} &= \frac{I^e_x l^e}{A^e n}\sum_{i=1}^{n}\left[\mathbf{B}^T_{\chi x}(z_i)\,\chi^{\varepsilon}_{x_i}\right] \\
\mathbf{f}^e_{\chi y} &= \frac{I^e_y l^e}{A^e n}\sum_{i=1}^{n}\left[\mathbf{B}^T_{\chi y}(z_i)\,\chi^{\varepsilon}_{y_i}\right]
\end{aligned} \tag{2.36}
$$

The considerations on the matrices $[\mathbf{k}^e]$ and $[\mathbf{f}^e]$ are analogous to those in the treatment of the Timoshenko beam element. Moreover, proceeding in a similar way as in the previous treatment yields the same equation,

$$\mathbf{Kq} = \mathbf{F} \tag{2.37}$$

2.2.1 Element shape functions

The element shape functions definition is based on the degree of interpolation required: continuity of order C^{j-1} must be guaranteed on the element interface, where j is the maximum order of derivation of the displacements in the variational formulation (equation 2.27). Being $j = 1$ for axial displacement and $j = 2$ for the two transverse displacements, C^0 and C^1-continuity must be ensured for axial and transverse displacements, respectively. In this section, the inverse element called 0^{th} order element is defined. The interpolation has been realized through the use of Hermite polynomials in terms of non-dimensional coordinates $\xi = (z/l^e) \in [0, 1]$, where $z \in [0, l^e]$ and l^e indicates the element length.
In figure 2.5 is presented the configuration of the 0^{th} order element. This one is characterized by two nodes 1 ($\xi = 0$) and 2 ($\xi = 1$) with ten degrees of freedom.

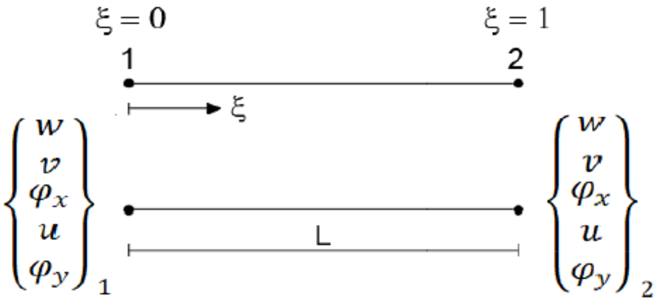

Figure 2.5: 0^{th} *order element [29]*

The formulation presented is consistent with the equilibrium equations in the case of concentrated forces and moments applied to the end nodes. From the constitutive equations, the resulting forces and moments are,

$$\begin{aligned} N &= EA\,\varepsilon_{z0} \\ M_x &= EI_x\,\chi_x \\ M_y &= EI_y\,\chi_y \end{aligned} \tag{2.38}$$

The equation 2.38 shows that the axial strain ε_{z0} is constant, while the curvatures χ are linear. It follows that w is linear, while u and v are cubic. Then, the shape functions of w are obtained considering the Hermite polynomial defined on two nodes ensuring the continuity of the single function, while the shape functions of u and v are obtained considering both the continuity of the function and of the derivative. The following set of interpolation relations is obtained:

$$\begin{aligned} w(\xi) &= \sum_{i=1}^{2} H_{0i}^{(0)}(\xi)\,w_i \\ v(\xi) &= \sum_{i=1}^{2} H_{0i}^{(1)}v_i + H_{1i}^{(1)}(\xi)\,\phi_{xi} \\ u(\xi) &= \sum_{i=1}^{2} H_{0i}^{(1)}u_i + H_{1i}^{(1)}(\xi)\,\phi_{yi} \end{aligned} \tag{2.39}$$

where $\mathbf{H}_{0i}^{(0)}\,(i = 1, 2)$ are the linear Lagrange polynomials, whereas $\mathbf{H}_{ki}^{(1)}\,(i = 1, 2; k = 0, 1)$ are the cubic Hermite polynomials.

2.2.2 Estimating strain measures

Similarly to the Timoshenko beam element, in order to implement iFEM, it is necessary to calculate the sectional strain measurements of the beam. Unlike before, the sectional strains are 3, not 6. This simplifies the problem because only 3 experimental strain measurements are required for each section to determine the sectional strains **e(u)**. Consider a generic axial co-ordinate of the beam z_i, at which 3 strain gauges are mounted at co-ordinates x_1 and y_i $(i = 1, 2, 3)$ (figure 2.6).

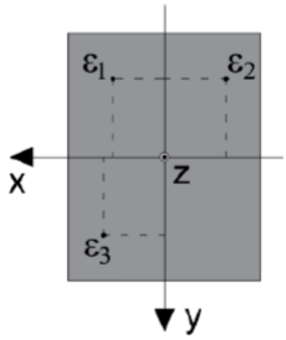

Figure 2.6: *Strain gauge coordinate system [29]*

The equation relating the axial strain $\varepsilon^{\varepsilon}_{z,i}$ at the z_i coordinate to the sectional strains, is

$$\varepsilon^{\varepsilon}_{z,i} = \varepsilon^{\varepsilon}_{z0} + y_i \chi^{\varepsilon}_x - x_i \chi^{\varepsilon}_y \tag{2.40}$$

3 Strain measuring sensors

In this section, a description of the fiber Bragg grating and strain gauges is presented.

3.1 Fiber Bragg Grating

As already mentioned, the discrete surface strain measurements can be provided by strain gauges and/or fiber Bragg grating. Even though only strain gauges have been used for the experimental tests, here is briefly reported the fiber Bragg working principle since its use is rapidly increasing in the aeronautic field.

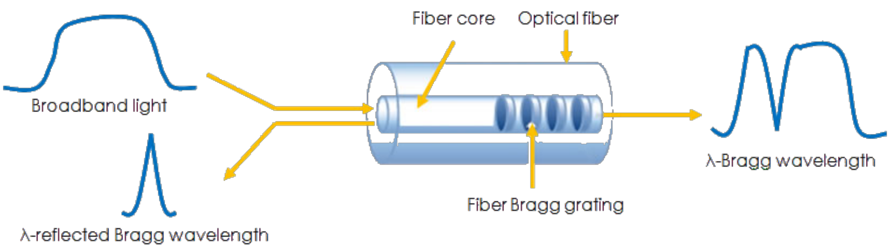

Figure 3.1: *Bragg fiber [36]*

The optical strain gauges consist of optical fibers containing an internal Bragg grating. The optical fiber is similar to the normal fiber used for telecommunications and can be very long and have many measuring points distributed along its length. The fiber consists of two layers: the core and the cladding. The fiber can be made of silica or polymeric material [30]. In the first case, the core is drugged with germanium in order to increase the refractive index n_1 while the cladding is drugged with boron in order to decrease the refractive index n_2. Due to the refractive index discontinuity between the core and cladding, reflection phenomena occur.

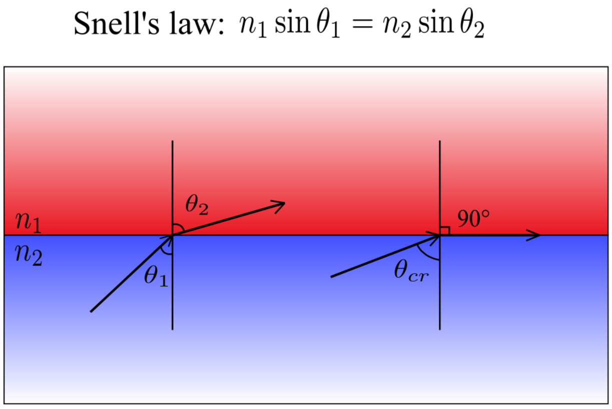

Figure 3.2: *Snell's Law*

For the Snell's law, $n_1 \sin\theta_1 = n_2 \sin\theta_2$. If $n_1 > n_2$ and $\theta_1 > \theta_{cr}$ (where $\theta_{cr} = \arcsin\frac{n_2}{n_1}$), total internal reflection occurs. By exploiting this physical principle, the light remains within the core. In the core of the optical fiber is installed the fiber Bragg grating (FBG), whose length varies between 0.1 and $10\,\mathrm{mm}$. They are realized by means of appropriate local modulation of the refractive index of the core of a photosensitive optical fiber, carried out by means of an energy source such as UV radiation. When an incident spectrum of light propagates through the grating, a specific wavelength named the Bragg wavelength is reflected back, while the rest of the spectrum is transmitted unaffected (the attenuation is minimum at the wavelength $1.550\,\mathrm{nm}$ and is equal to $0.2\,\mathrm{dB\,km^{-1}}$) [31]. When an external axial strain is induced, the FBG reacts accordingly causing a proportional shift in the reflected Bragg wavelength which takes a longer or shorter time to complete the entire round trip: from this time, the strain can be traced.
The reasons why Bragg fiber is widely used for structural health monitoring of aircraft composites are:

- they are very well suited to be embedded into composite materials without altering their mechanical performances, thanks to their lightweight and small dimensions;
- the possibility of inscribing hundreds of Bragg gratings in a single optical fiber, allowing the measurement of the strains on many points of the structure or/and serial multiplex ability;
- they are characterized by a long lifetime (more than 20 years).
- they are stable over time (no calibration required) and do not suffer from corrosion.
- immunity against electromagnetic radiation and insensitivity to radio frequency interference.

Although difficulties remain associated with the process of embedding fibers into composites, the above-mentioned characteristics make Bragg fiber excellent for monitoring the strain and/or tensional state of composite materials whose non-homogenous nature leads to complex and not yet perfectly understood degradation and failure processes [1].

3.2 Strain Gauge

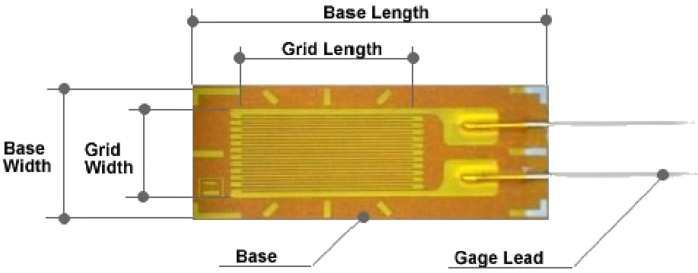

Figure 3.3: *An electric strain gauge [37]*

The strain gauge consists of a grid of very thin metallic wire rigidly applied on a plastic material support. The strain gauge is glued integrally on the structure surface. When the surface experiments deform due to loads applied to it, the mechanic deformation induces a variation in the dimensions of the grid which causes a change in the electrical resistance. Then the voltage measurement is gathered using data acquisition thanks to the gauges lead welded to the sensitive element of the base. The law that rules the change from mechanical strain to electrical variation is the Ohm'law.

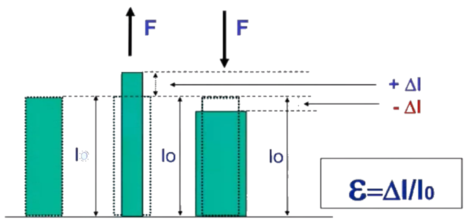

Figure 3.4: *Mechanical principle [30]*

Consider that the strain gauge is glued integrally to the structure, and let l_0 be the grid length [30]. When a force is applied to the structure, the strain gauge grid undergoes the same strain, ε, as the structure. Ohm's second law states that the resistance R of a conducting wire is directly proportional to its length l_0 and inversely proportional to its cross-sectional area A

$$R = \rho \frac{l_0}{A} \tag{3.1}$$

where ρ is a constant of proportionality known as resistivity. This depends on the material the wire is made of and its temperature. The strain gauge resistance variation can be expressed as

$$\Delta R = \frac{\Delta \rho}{\rho_0} + \frac{\Delta l}{l_0} - \frac{\Delta A}{A_0} \tag{3.2}$$

The resistance variation can be related to the strain of the grid; in order to do this, it must be ensured that the cross-section A and the resistivity of the material ρ vary as little as possible.

This is why efforts are made to make a long and thin conductor: in this way, during mechanical deformation, a large change in length and a small change in cross-sectional area are obtained. Furthermore, in order to have an important and sufficient change in R for the measurement, a certain length of the conductor is required: in fact, the grid is created by folding the conductor to have a sufficiently large length. This allows for both a significant change in resistance and a localized measurement of strain.
Let's introduce the gauge factor S_A: it is the ratio of the relative change in electrical resistance R, to the mechanical strain ε

$$S_A = \frac{\frac{\Delta R}{R}}{\frac{\Delta L}{L}} = \frac{\frac{\Delta R}{R}}{\varepsilon} = 1 + 2\nu + \frac{\frac{\Delta\rho}{\rho}}{\varepsilon} \tag{3.3}$$

The gauge factor value depends on the material used for the manufacture of the strain gauge; for metal strain gauges its value is between 2 and 4.
To evaluate the strain ε, it's necessary to compute the ratio $\frac{\Delta R}{R}$. In order to do this, it is necessary to use an instrument known as an ohmmeter which allows for measuring the resistance of the conductor. However, because it is a very imprecise measure it is preferred to measure the voltage applied at the ends of the strain gauge, which is much more precise, easy, and simple to measure. The strain gauge must be inserted into a circuit known as a Wheatstone bridge, which allows the resistance variation to be measured indirectly by appreciating the voltage variations at the ends of the circuit. A Wheatstone bridge scheme is reported in figure 3.5.

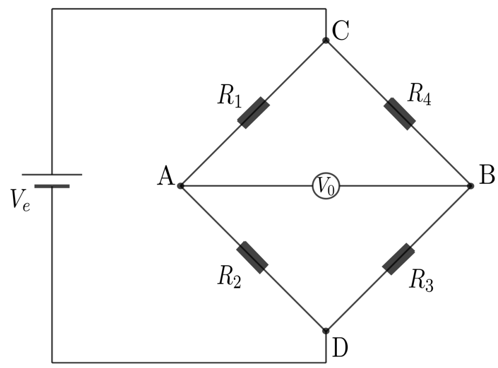

Figure 3.5: *Wheatstone bridge*

In the Wheatstone bridge there are 4 resistances connected in a rhomboid shape. The system is supplied at terminals **C** and **D** with a known voltage V_e, while a voltage V_0 is measured at the terminals **A** and **B**. If the resistance values are all the same, the voltage V_0 is zero and in this case, the bridge is said to be *balanced*. More in general, the bridge is balanced if the following equation is respected

$$R_1 R_3 = R_2 R_4 \tag{3.4}$$

If one of these four resistances is replaced with the strain gauge grid, which is in fact a resistance, as its resistance changes due to mechanical stress acting on the structure, an unbalancing of the bridge is obtained. Knowing the applied voltage V_e and by reading the voltage V_0, it's possible to correlate the change in strain gauge resistance with its strain. The relationship between the four resistance and the two voltages for the Wheatstone bridge is

$$\frac{V_0}{V_e} = \frac{R_1 R_3 - R_2 R_4}{(R_1 + R_2)(R_3 + R_4)} \tag{3.5}$$

By performing a differential variation of the $\frac{V_0}{V_e}$ ratio, it is possible to obtain a direct proportionality between the variations of the individual resistance in proportion to the voltage V_0

$$\frac{V_0}{V_e} = \frac{1}{4}\left[\frac{\Delta R_1}{R_1} - \frac{\Delta R_2}{R_2} + \frac{\Delta R_3}{R_3} - \frac{\Delta R_4}{R_4}\right] = \frac{S_A}{4}\left[\varepsilon_1 - \varepsilon_2 + \varepsilon_3 - \varepsilon_4\right] \tag{3.6}$$

where it has been used the equation 3.3 to express the relantioship between gauge factor S_A, strain ε and change in electrical resistance $\frac{\Delta R}{R}$. The equation 3.6 is valid in the case all four resistances have been replaced with strain gauges.
Let's consider the typically used configurations.

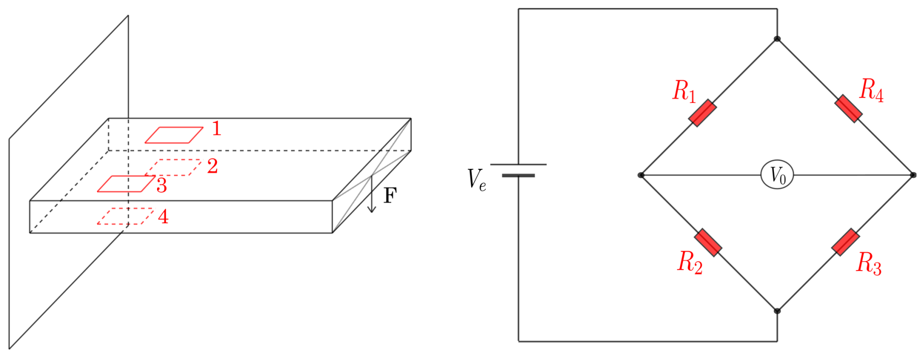

Figure 3.6: *Full bridge configuration*

In figure 3.6 is presented the full bridge configuration, which is the case where all the resistances have been replaced by the strain gauges (the resistances replaced by strain gauges are colored red in the Wheatstone Bridge). The concentrated load is applied in the free end of the beam in its center of gravity, leading to the strain gauges 1-2-3-4 to measure the same strain (in absolute value)

$$\varepsilon_1 = \varepsilon_3 = -\varepsilon_2 = -\varepsilon_4$$

Substuting the strain gauges strains in equation 3.6 leads to

$$\frac{V_0}{V_e} = \frac{S_A}{4}\left[\varepsilon_1 - \varepsilon_2 + \varepsilon_3 - \varepsilon_4\right] = \frac{S_A}{4}\left[\varepsilon_1 - (-\varepsilon_1) + \varepsilon_1 - (-\varepsilon_1)\right] = \frac{S_A}{4}\left[4\varepsilon\right] = S_A\varepsilon \tag{3.7}$$

where the following statment $\varepsilon_1 \equiv \varepsilon$ has been applied. The full bridge configuration enables gaining the maximum ratio value $\frac{V_0}{V_e}$. Attention must be paid to the strain gauges placement in order to get an unbalanced bridge. If strain gauges 2 and 3 were reversed, this would result in a balanced bridge and no strain could be measured.

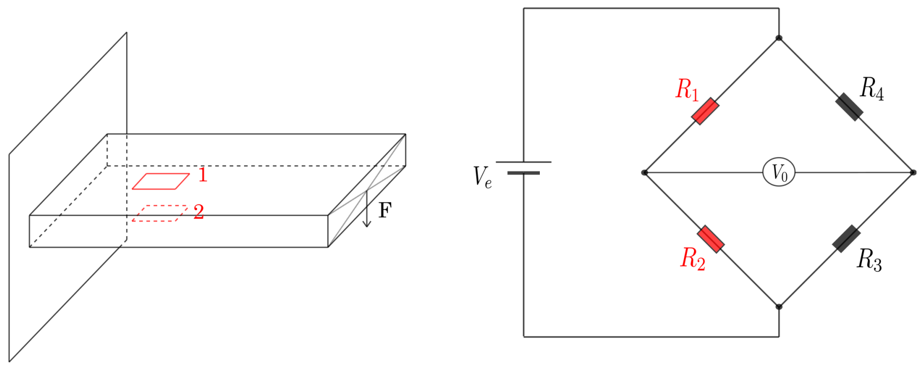

Figure 3.7: *Half bridge configuration (type II)*

Use the half-bridge configuration (type II) (figure 3.7) leads to the following $\frac{V_0}{V_e}$ ratio

$$\frac{V_0}{V_e} = \frac{S_A}{4}\left[\varepsilon_1 - \varepsilon_2\right] = \frac{S_A}{4}\left[\varepsilon_1 - (-\varepsilon_1)\right] = \frac{S_A}{4}\left[2\varepsilon\right] = \frac{S_A}{2}\varepsilon \tag{3.8}$$

When strain gauges are used, another important factor to consider is temperature compensation. Let's consider the quarter bridge configuration in figure 3.8, assuming that only strain gauge 1 is connected to the Wheatstone bridge.

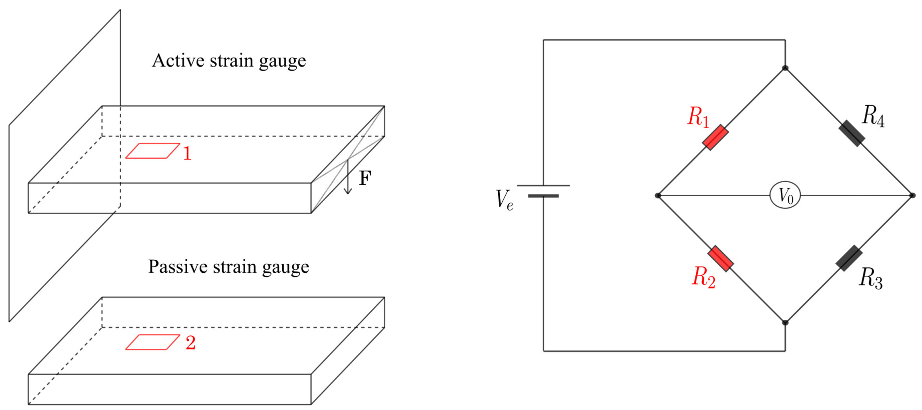

Figure 3.8: *Quarter bridge configuration*

In this case the strain gauge 1 measure both the mechanical ($\bar{\varepsilon}$) and the thermal strain (ε^T)

$$\varepsilon_1 = \bar{\varepsilon} + \varepsilon^T \tag{3.9}$$

Using equation 3.6 adapted for the quarter-bridge configuration and substituting the equation 3.9, leads to

$$\frac{V_0}{V_e} = \frac{S_A}{4}\left[\varepsilon_1\right] = \frac{S_A}{4}\left[\bar{\varepsilon} + \varepsilon^T\right] \tag{3.10}$$

With this kind of configuration both the thermal and the mechanical strain are measured. This is why the used quarter-bridge configuration that provides the temperature compensation is the one illustrated in figure 3.8. Here the strain gauge 2 is called *passive strain gauge* since it's glued on an unloaded structure that is made of the same material as the structure whose strain is to be calculated. The strains measured by the strain gauges 1 and 2 are

$$\varepsilon_1 = \bar{\varepsilon} + \varepsilon^T; \quad \varepsilon_2 = \varepsilon^T \tag{3.11}$$

Substituting equation 3.11 in equation 3.6,

$$\frac{V_0}{V_e} = \frac{S_A}{4}\left[\varepsilon_1 - \varepsilon_2\right] = \frac{S_A}{4}\left[\bar{\varepsilon} + \varepsilon^T - \varepsilon^T\right] = \frac{S_A}{4}\bar{\varepsilon} \tag{3.12}$$

The full-bridge and half-bridge configurations shown before already provide temperature compensation. In figure 3.9 is reported the half-bridge configuration used for the first experimental test.

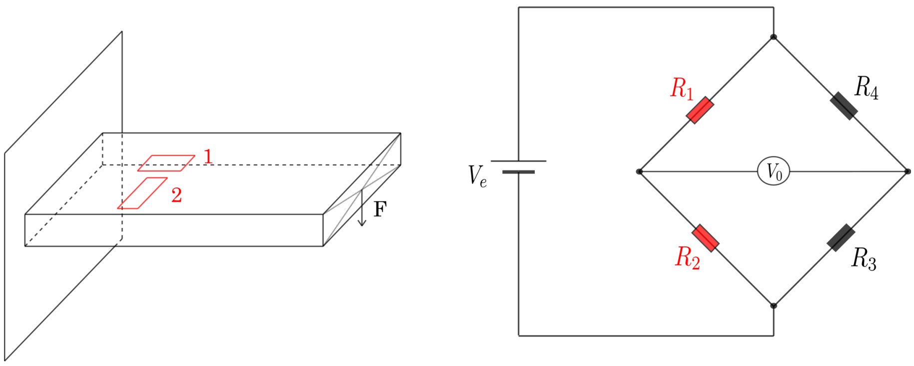

Figure 3.9: *Half bridge configuration (type I)*

The strain gauges 1 and 2 are both active, with the difference that strain gauge 1 is mounted in the direction of axial strain and strain gauge 2 acts as a Poisson gage and is mounted perpendicular to the principal axis of strain. This configuration allows for temperature compensation and for a $\frac{V_0}{V_e}$ ratio greater than the quarter-bridge configuration but less than the half-bridge type II configuration,

$$\frac{V_0}{V_e} = \frac{S_A}{4}\left[\varepsilon_1 - \varepsilon_2\right] = \frac{S_A}{4}\left[\varepsilon - (-\nu\varepsilon)\right] = \frac{S_A}{4}(1+\nu)\,\varepsilon \tag{3.13}$$

4 Experimental tests

Two different experimental tests have been carried out. First, the two experimental tests will be described as their relative setups, subsequently, the data fusion methods will be presented together with the developed algorithms.

4.1 Experiment 1

In the development of a new method, it is a good rule to start with very simple case studies and then gradually increase their complexity. The easiest case study, which was actually applied, is the loading of a beam with static loads. The first trial tests have been performed at George Mason University, in the Advanced Infrastructure Monitoring (AIM) Lab. The beam used in the test was made of architectural 6063 Aluminum, manufactured through the extrusion process followed by artificial aging. The beam's geometric dimensions and its material properties are reported in table 4.1, while the beam and its principal reference system are reported in figure 4.1.

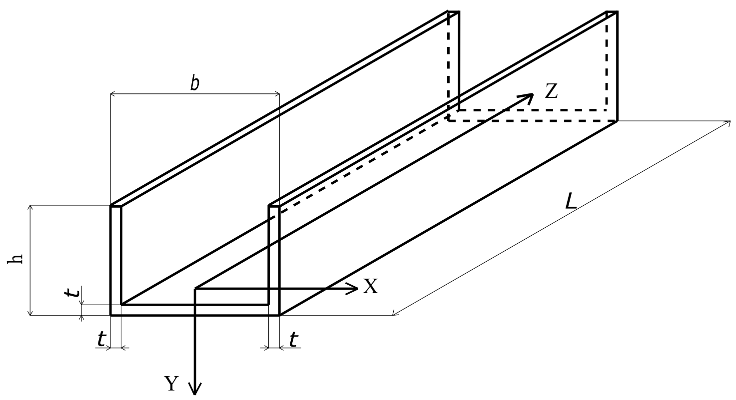

Figure 4.1: *Beam geometric dimensions*

$b = 50.80\,\mathrm{mm}$
$h = 18.50\,\mathrm{mm}$
$t = 1.60\,\mathrm{mm}$
$L = 2414.6\,\mathrm{mm}$
$E = 68\,900\,\mathrm{MPa}$
$\nu = 0.33$

Table 4.1: *Beam geometric properties and material characteristics*

Initially, the experiment was conceived as a test in which to perform a data fusion between different techniques and measurements, these were:

- strains provided by strain gauges;
- local displacements provided by video and photogrammetric techniques;
- global displacements provided by photogrammetric techniques.

To the list above should be added also the laser sensor, but since only one sensor was available, this was used to check whether the behavior of the experimental beam was in line with that of the analytical beam. However, since the photogrammetric technique based on the *Structure from Motion* (SfM) algorithm was very time-consuming for the 3D reconstruction of the beam's displacement field, it was decided downstream of the experiment to exclude it from the data fusion.

4.1.1 Experimental setup

Six strain gauges were installed on the beam in the half-bridge type I configuration (figure 3.9), for a total of 3 strain local values along the beam. The strain gauges were installed at the beam locations $\frac{L}{4}$, $\frac{L}{2}$ e $\frac{3L}{4}$ and then they were connected to the acquisition system NI cDAQ-9188 through a C module series. In figure 4.2 is reported the beam cross section in the inertial reference system,

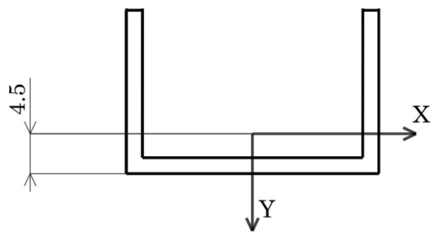

Figure 4.2: *Beam cross-section in main inertia reference system*

The type I half-bridge configuration was chosen because it was the best compromise between the simplicity of strain gauge installation and high V_0/V_e gain. In the case of the type II half-bridge configuration, in order to record the highest $\frac{V_0}{V_e}$ value, one strain gauge should have been placed at the bottom of the beam (horizontal element) while the second strain gauge should have been placed at the same distance from the neutral axis as the first strain gauge in order to record the same strain (on the vertical element). To avoid errors caused by incorrect positioning of the second strain gauge, it was decided to apply the Type I configuration. However, in order to be able to use this type of configuration, it was also necessary to provide the data acquisition system with the material's Poisson coefficient ($\nu = 0.33$).
Next, taking care to cover the strain gauges with tapes, the beam was painted. The paint was applied to all surfaces of the beam by means of small drops of three different colors. The painting was performed in order to apply the global photogrammetry and the optical flow techniques, which require *texture* presence to be able to work. Even though these two techniques were not been used, the presence of texture improved and helped the image registration method.
After applying a stabilizer and allowing the paint to dry, the beam was placed on the support system. Four holes were drilled on the beam, two at each end so that it could be mechanically connected (via bolt) to the nub of a standard structural pivot (figure 4.3).

Figure 4.3: *Structural pivot [38]*

The nub was connected to the support system through his arms. The structural pivot is the element that allows the beam to be constrained as a hinge or as a clamp. Referring to the figure 4.4, depending on how tightly the screw was tightened, the pivot was made more or less able to rotate. If the screw was loosely screwed in, the simulated constraint was close to that of the hinge; if the screw was fully screwed in, the simulated constraint was that of the clamp.

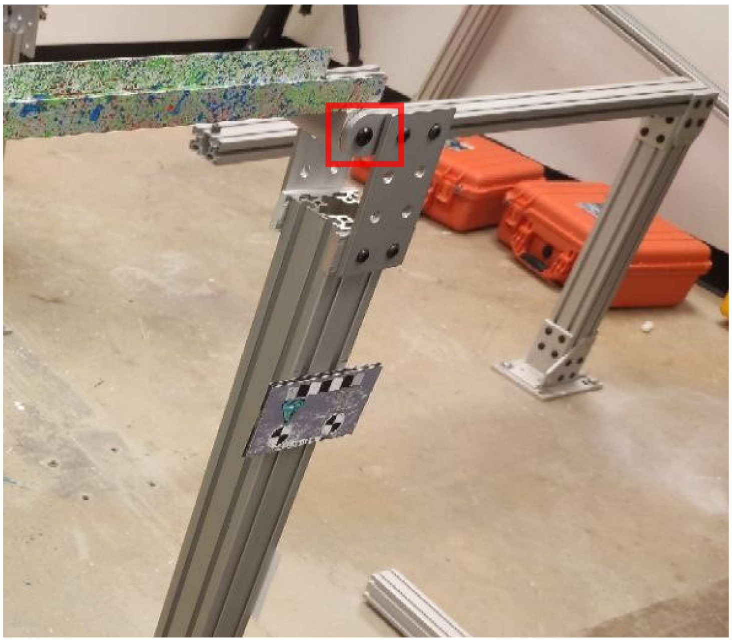

Figure 4.4: *Structural pivot - beam*

To simulate the roller constraint, two rotating plastic elements were mounted on the vertical support. These element are reported in figure 4.5

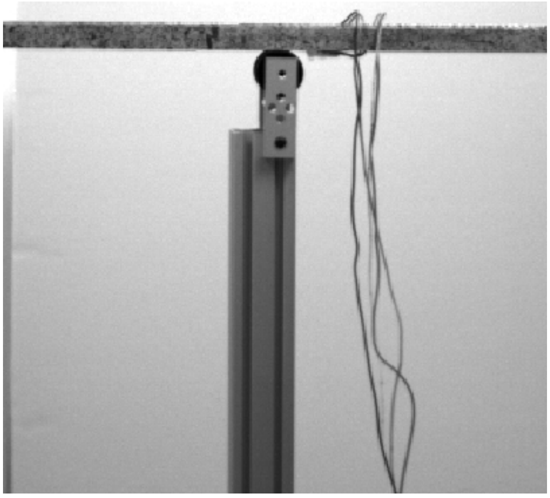

Figure 4.5: *Roller constraint*

The other measuring sensor in the experiment, apart from strain gauges, was the laser sensor. The laser sensor adopted was the optoNCDT 1420; it can measure a maximum displacement of $10\,\mathrm{mm}$, with a sampling frequency of up to $4\,\mathrm{kHz}$. Only one laser sensor was available and it was placed on a support system so that it was close enough to the beam.

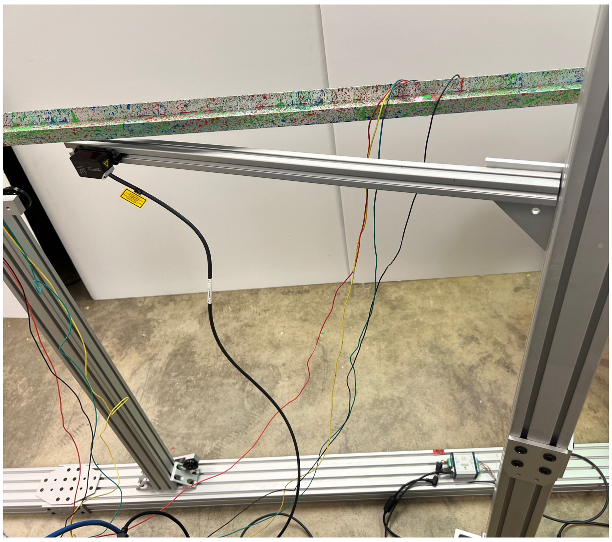

Figure 4.6: *Laser sensor on its support*

Once the beam had been placed on the support system and the position of the latter had been decided, the camera was positioned to video record the beam during the load application phase. The camera, of the Ueye industrial family, was placed on a tripod which ensured the maintenance of the position.

Figure 4.7: *Camera on its support*

A whiteboard was placed behind the beam so as to increase the contrast between the background and the beam, making it easier for the image-to-image matching (IIM) algorithms to calculate the displacement. The final setup is reported in figure 4.8.

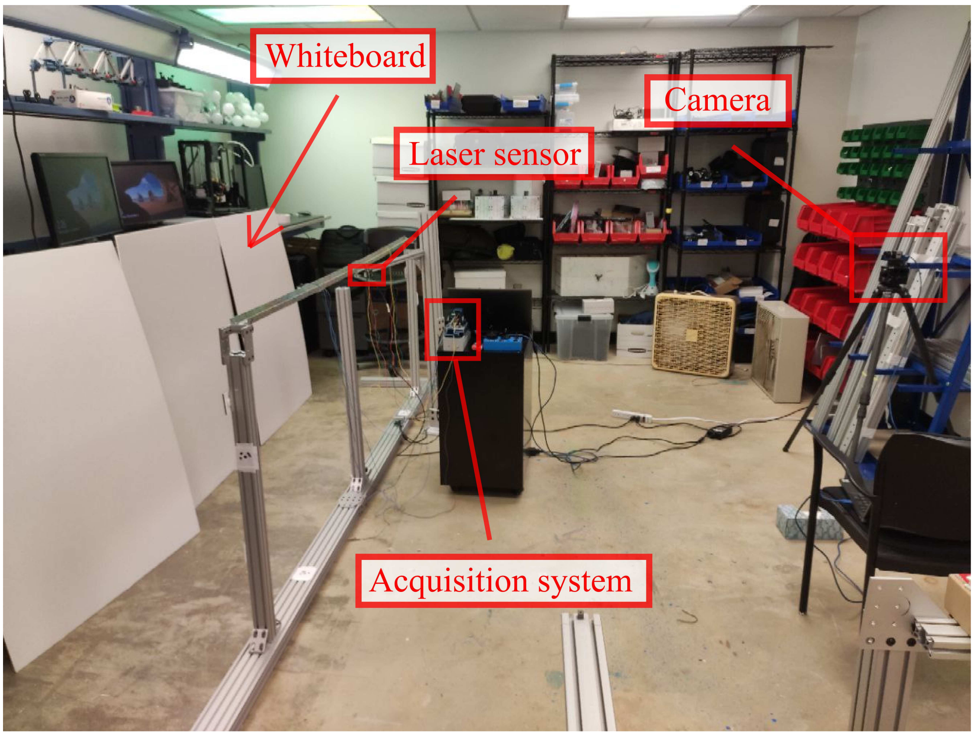

Figure 4.8: *Experiment 1 setup*

4.1.2 Loads and boundary conditions

Once the set-up was completed, the tests could be carried out. Each test was performed with the following procedure:

1. at time $t = 0\,\text{sec}$, recording was started with the video camera, as the laser sensor and strain gauges samplings;
2. at $t = 3\,\text{sec}$ the beam was loaded;
3. at $t = 6\,\text{sec}$ the beam was unloaded,
4. at $t = 10\,\text{sec}$ the recording and the samplings ended.

The reason why only 10 seconds were used to make the videos is due to the software used for recording the strain data, which acted for a maximum of 10 seconds. It should be noted that the procedure above described was repeated three times for each test. Since loading was done by placing weights on the beam or on supports attached to it, there were the risks of:

- placing the weight in a position different from the agreed one;
- introducing undesired dynamic effects.

By performing this test only once, there would have been a risk of making such errors without realizing it. Instead, by executing it three times, it was ensured that the measurements were consistent with each other and that neither of the two errors mentioned above was committed. Each load condition analyzed is shown in the table 4.2.
Note that for loads greater than $0.5\,\text{kg}$, the approximation symbol '$\simeq$' appears for the point of load application and for the position of the roller. The reason is the following: for loads equal to or less than $0.5\,\text{kg}$, weights were available that could simply be placed on the beam. In figure 4.9 is shown one of these weights caught on camera.

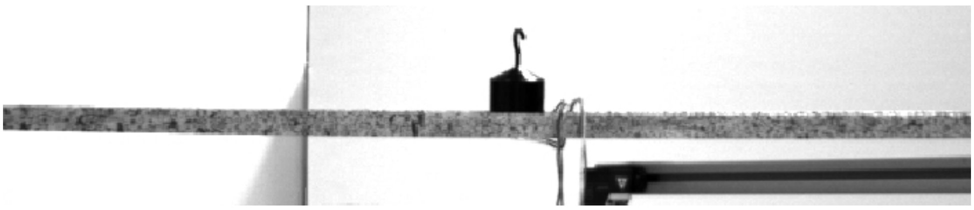

Figure 4.9: *Kind of weight used for the test*

<table>
<tr><th>Case Study</th><th>Load ($F = mg$)</th><th>Load application points</th><th>Constraints</th></tr>
<tr><td rowspan="3">1</td><td>1. $m = 0.05\,\mathrm{kg}$</td><td rowspan="3">$\frac{L}{2}$</td><td rowspan="3">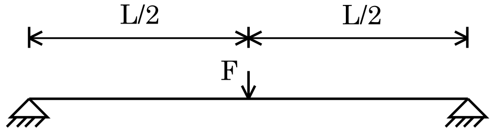</td></tr>
<tr><td>2. $m = 0.2\,\mathrm{kg}$</td></tr>
<tr><td>3. $m = 0.5\,\mathrm{kg}$</td></tr>
<tr><td>2</td><td>$m = 0.2\,\mathrm{kg}$</td><td>$\frac{L}{4}$, $\frac{3L}{4}$</td><td>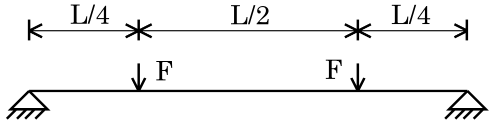</td></tr>
<tr><td rowspan="3">3</td><td>1. $m = 6\,\mathrm{kg}$</td><td>$\simeq \frac{L}{4}$, $\simeq \frac{3L}{4}$</td><td>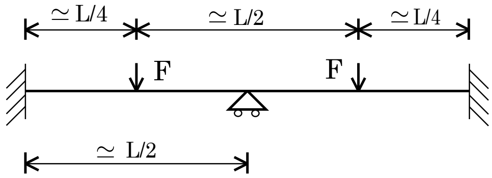</td></tr>
<tr><td>2. $m = 6\,\mathrm{kg}$</td><td>$\simeq \frac{3L}{4}$</td><td>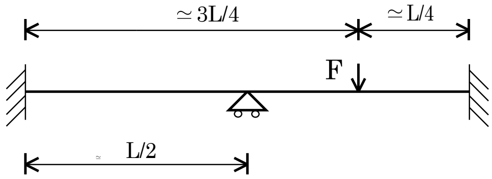</td></tr>
<tr><td>3. $m = 0.5\,\mathrm{kg}$</td><td>$\frac{L}{2}$</td><td>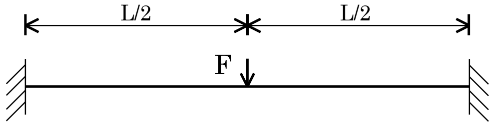</td></tr>
<tr><td rowspan="2">4</td><td>1. $m = 6\,\mathrm{kg}$</td><td>$\simeq \frac{L}{4}$, $\simeq \frac{3L}{4}$</td><td>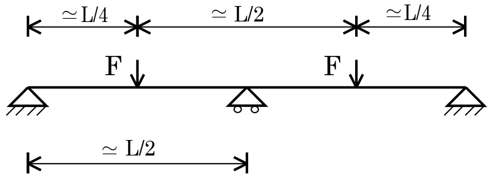</td></tr>
<tr><td>2. $m = 6\,\mathrm{kg}$</td><td>$\simeq \frac{3L}{4}$</td><td>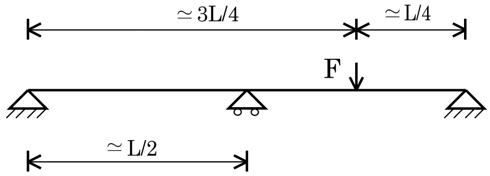</td></tr>
</table>

Table 4.2: *Case studies*

In the case of higher loads, the loads were applied by means of disc weights placed on a support that was attached with bands to a plastic element that was placed on the beam. To avoid placing the plastic element over the electrical cables of the strain gauges, and thus to avoid compromising their connection to the data acquisition system, they were placed 2 centimeters away from the indicated positions in table 4.2, precisely at $z = 622.3\,\mathrm{mm}$ and $z = 1792.3\,\mathrm{mm}$, while the roller was placed at $z = 1187.45\,\mathrm{mm}$

Once the experiments had been performed, the videos were stored, while the strain gauge strains and laser displacements were saved in Excel files.

4.2 Experiment 2

The second test has been conducted at the LAQ-AERMEC laboratory of the Mechanical and Aerospace Engineering Department of the Politecnico of Torino. The experiment was performed on a *C* shaped beam, made of architectural 6063 Aluminum, clamped at one end, and loaded in the free end. Loading the beam at a point other than the shear center (SC) would cause the beam to twist. Wanting to investigate the case of pure bending, the beam was loaded at the shear center. The beam's geometric dimensions and material properties are reported in table 4.3, while a beam sketch is reported in figure 4.10.

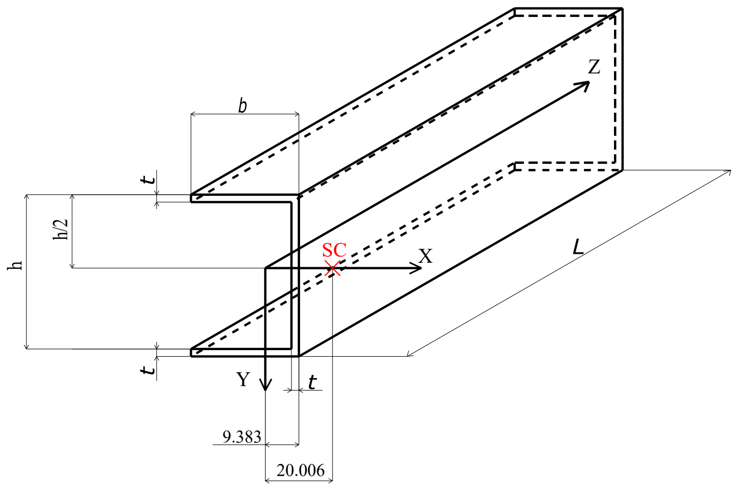

Figure 4.10: *Beam geometric dimensions*

$b = 30.13\,\mathrm{mm}$
$h = 45.20\,\mathrm{mm}$
$t = 2.08\,\mathrm{mm}$
$L = 1100\,\mathrm{mm}$
$E = 68\,030\,\mathrm{MPa}$
$\nu = 0.335$

Table 4.3: *Beam geometric properties and material characteristics*

4.2.1 Experimental setup

The second experimental test was carried out after both the first test and the writing of the algorithm. This is why the test was set up in such a way as to eliminate the criticalities that occurred in the first experiment. These are given at the end of subsection 6.1.4 and are reported here:

1. having only one accurate experimental measurement of beam displacement;
2. using an insufficient number of strain gauges to apply iFEM;
3. not having any strain gauges in the vicinity of the constraints;
4. constraints being far from the ideal ones;

5. having taken only half of the beam with the video camera.

To compensate for the reduced number of strain gauges in the first experiment, 14 were installed in the second. Two axial strain gauges were placed $12\,\mathrm{mm}$ away from the clamp, one on the upper horizontal flange and one on the lower, while the others were installed, along $45°$ directions, at the beam sections $\frac{L}{6}, \frac{L}{3}, \frac{2L}{3}, \frac{5L}{6}$. Three strain gauges were installed at each of the four stations. The positions of the strain gauges along the beam and on the section are schematized in figure 4.11, where red is used to mark the axial strain gauges and blue to mark the strain gauges oriented at $45°$. All strain gauges were connected to the MGCplus HBM acquisition system.

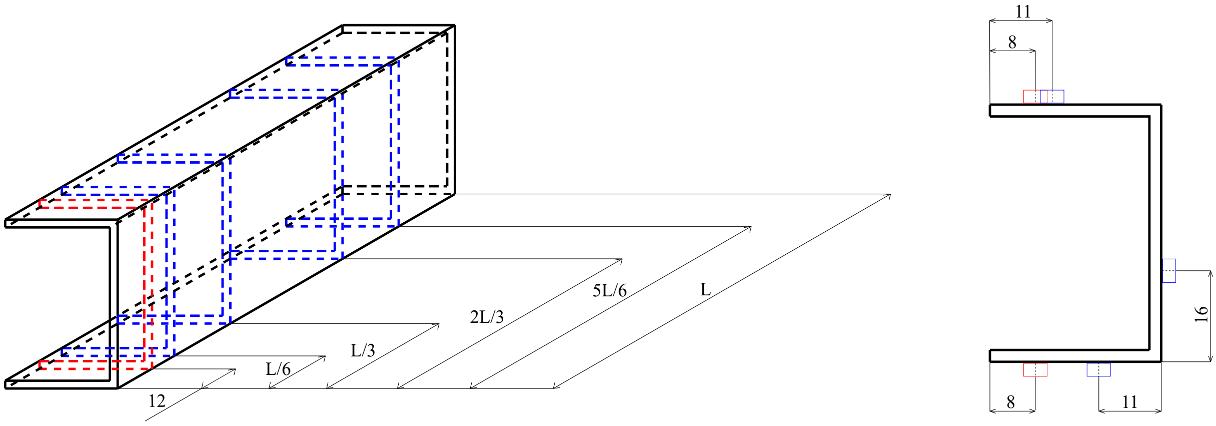

Figure 4.11: *Strain gauges locations*

With this number of strain gauges available, it was possible to apply iFEM and also correct the zero strain to the clamp constraint, the latter resulting from the double derivation of the displacement function $v(z)$ obtained by smoothing spline.
Since the displacements had to be computed from the *image-to-image matching* (IIM) method, the beam was painted to give texture. Different attempts were made to find the most suitable texture: after the preliminary selection, the beam was first painted with a matt white color to remove the reflective effect due to the aluminum metal surface, after a black color pattern was applied using a spray can. Unlike the previous experiment, the beam was not painted in its entirety. In fact, the speckle pattern suitable for the use of the DIC 3D was applied to a portion of the free end of the beam.

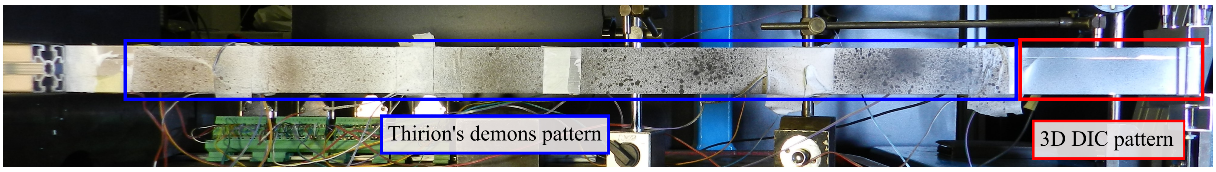

Figure 4.12: *Beam pattern for Thirion's demons algorithm and 3D DIC*

This choice was made in order to have more experimental measurements of the beam displacement available, which are essential for evaluating the final accuracy of the beam shape reconstruction methods.
In this experiment, to simulate the clamp constraint, the beam was placed between two very heavy metal blocks, which can be seen in figure 4.13. In order to prevent these elements from

crushing the beam, the beam section was reinforced with wooden pieces placed inside it, and blunt aeronautical aluminum elements were placed adjacent to the beam.

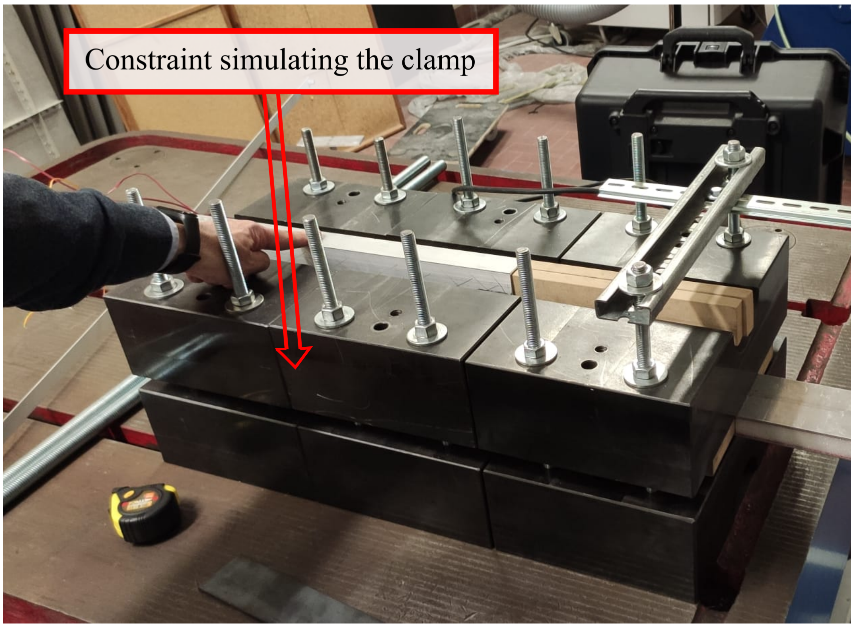

Figure 4.13: *Clamp constraint*

In addition to the DIC, two Linear Variable Displacement Transducers (LVDTs), *W1* and *W2*, were mounted at the free end of the beam at two different locations of the section. In this way, in addition to providing the tip displacement, the two LVDTs ensured that the beam was loaded at the shear center.

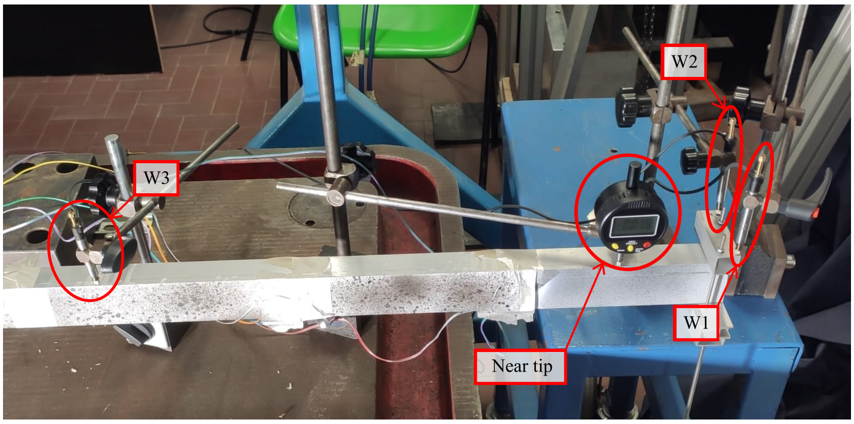

Figure 4.14: *LVDTs used in the test*

As can be seen from figure 4.14, two more LVDTs were mounted on the beam, labeled as *W3* and *LVDT near tip*. The LVDT *W3* was placed at $z = \frac{L}{2}$; the *LVDT near tip* was placed at $z = 1004\,\mathrm{mm}$. A marker was drawn below the latter: by monitoring the displacements of this point with the DIC, it was possible to check whether the displacements calculated by the DIC were correct and in line with those calculated by the LVDT.

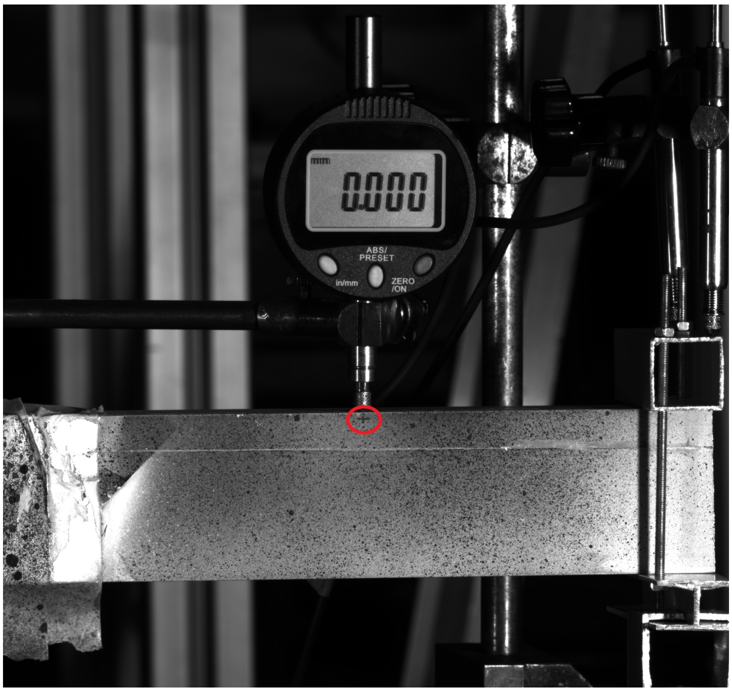

Figure 4.15: *Image taken by DIC - Marker under the LVDT*

The loading system used to load the beam is shown in figure 4.16,

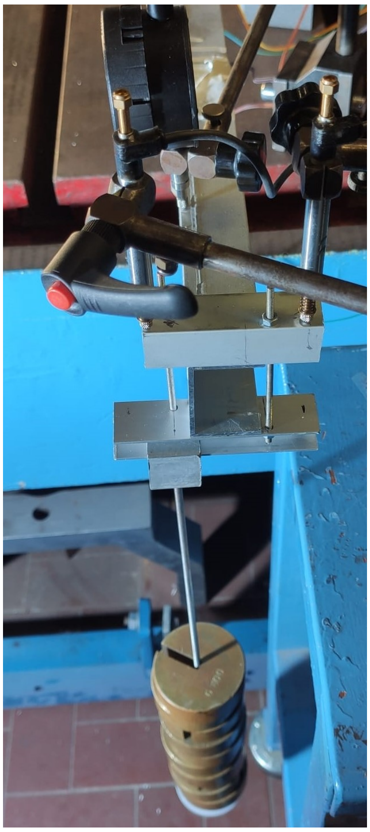

Figure 4.16: *Loading system*

Loading was achieved by placing metal discs on the base of a rod, with the latter being connected to the beam via a crossbar. By translating the loading system onto the crossbar and reading the displacement provided by the two LVDTs at the free end in real time, the position of the shear center could be identified. Unfortunately, loading the beam exactly at the shear center is very difficult, and failure to achieve this condition results in the beam twisting.
Once the beam was constrained, the loading system, and all the various sensors mounted, the 3 cameras were positioned: one camera was used to apply the image-to-image matching (IIM) technique, and the other 2 to use the 3D DIC. The arrangement of the cameras, together with that of the lights that illuminated the beam, is shown in figure 4.17

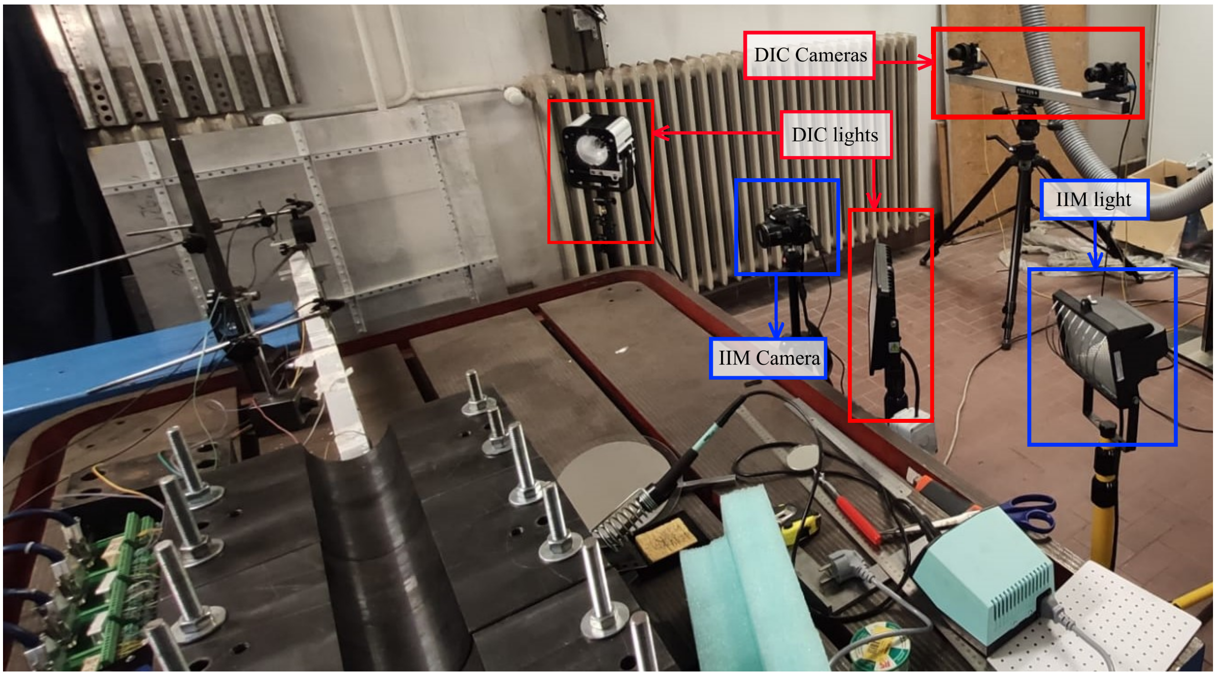

Figure 4.17: *Cameras and lights for DIC and IIM techniques*

While the two light sources of DIC mainly illuminated the ROI of DIC, the third light source served to illuminate the remaining part of the beam that was not illuminated by the other two. Furthermore, while the camera of the IIM was placed at a distance such that the entire beam surface was taken up and parallel to the CCD sensor, the cameras of the DIC were slightly inclined, since for the 3D DIC not only perpendicularity is not required, but it is recommended that the two cameras have between them an angle between $15°$ and $30°$. In this experiment, a relative angle of $18°$ was achieved.
Finally, to facilitate the IIM method to calculate displacements, a blackboard was placed behind the beam to increase its contrast with the background (figures 4.18),

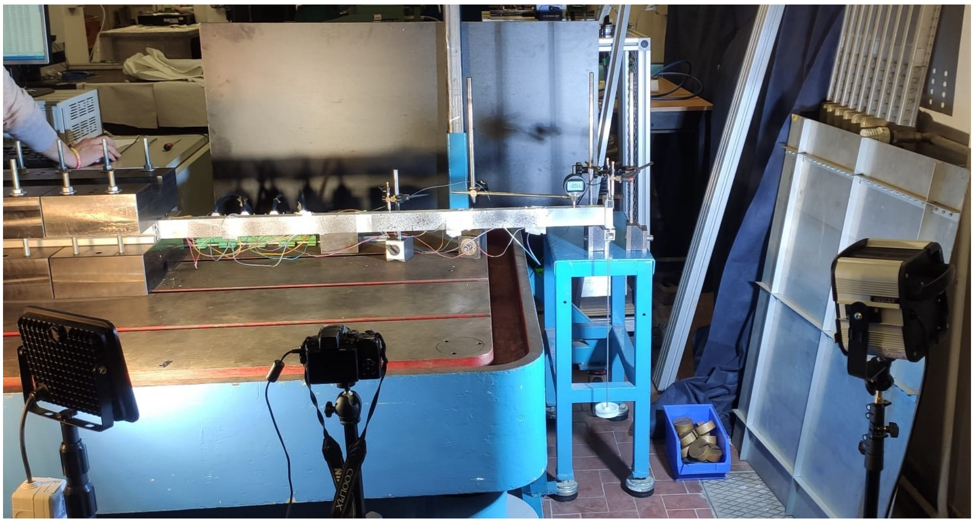

Figure 4.18: *Blackboard in the background*

4.2.2 Loads and boundary conditions

In this second experiment, the cantilever beam condition was analyzed, being a type of problem not analyzed in the previous experiment and presenting the clamp constraint, which constitutes the main problem when using smoothing splines. Six tests were performed, loading from $0\,\mathrm{kg}$ up to $5\,\mathrm{kg}$. Pictures were taken each time the beam was loaded with $1\,\mathrm{kg}$, and in the case of the IIM camera, pictures with a different exposure value (EV) were taken for each loading condition. In particular, negative exposure values (underexposure) were chosen as the light sources illuminating the beam, especially in the ROI of the DIC, greatly increased the brightness level.
All information from the individual tests is schematically presented in the table 4.4

Test	Black Board	Load range	Camera exposure $[EV]$
1	No	$[0;4]$ *Kg*	0, -0.3, -1.0
2	Yes	$[0;5]$ *Kg*	0, -0.3, -1.0
3	Yes	$[0;5]$ *Kg*	0, -0.3, -1.0
4	Yes	$[0;5]$ *Kg*	0, -0.3
5 Loading	Yes	$[0;5]$ *Kg*	0, -0.3
5 Unloading	Yes	$[5;0]$ *Kg*	-0.7

Table 4.4: *Case studies*

5 Data fusion: developed algorithms

At the end of the first experimental activity, two data fusion typologies were developed. Both data fusion methods were developed in such a way as to exploit the numerosity of the displacement data provided by the image registration method and then mitigate the noise through strain gauge measurements. Furthermore, with a view to data fusion with iFEM, the method was made compatible by preserving two main characteristics of the former, i.e. the independence of the loads acting on the structure and the material it is made of. The main steps of the two data fusion methods are shown in figure 5.1.

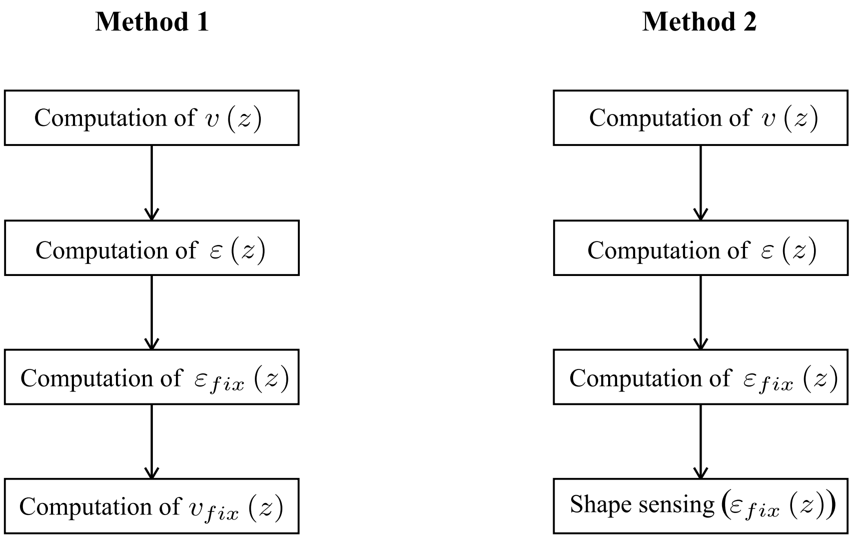

Figure 5.1: *Data fusion methods*

The *first method* consists of the computation of beam displacement field $v\,(z)$ from *image-to-image matching* (IIM); then the beam longitudinal strain field $\varepsilon\,(z)$ is computed via derivation of $v\,(z)$. Once $\varepsilon\,(z)$ is calculated, its trend is improved thanks to the strains provided by strain gauges. At this point, the new beam displacement field $v_{fix}\,(z)$ is computed through the integration of the $\varepsilon_{fix}\,(z)$ function. The idea behind this method is that IIM data are noisy while the strain gauge measurements are more accurate. Therefore, by integrating the strain field properly corrected with the values measured by the strain gauges, less noise and more accurate results can be obtained.
The *second method* is identical to the first one except for the last step. Instead of using integration to determine $v_{fix}\,(z)$, the strain field $\varepsilon_{fix}\,(z)$ is used to perform shape sensing via iFEM. This procedure works very well with iFEM. In equation 2.7 the weighting coefficients vector w_k^0 has been introduced, and it was also said that for inverse finite elements without strain data,

their value is imposed to be low (10^{-4}). Back to the second method, even though the strain field $\varepsilon_{fix}(z)$ is affected by noise, its strain values can be used for elements that don't have strain measurements. For iFEM purposes is better to provide less precise values with the appropriate weighting factor than not at all.
Due to the poor number of strain gauges present in the first experiment, shape sensing wasn't applicable. Therefore, the second and the third method have been applied only to the second experimental test.
In the next sections, a detailed explanation of the functioning of the algorithms developed for each of the two methods will be provided.

5.1 First method

To make it easier to understand the procedure adopted, as the algorithm is explained intermediate results of case study 3.3 of the first experiment (table 4.2) are shown. At the end of the explanation, the changes made to the algorithm to perform the second experiment are shown.

5.1.1 Computation of $v(z)$

The computation of the displacement field $v(z)$ is the same for all three methodologies.

Image pre-processing

The displacement function $v(z)$ calculation starts from the video or images. Since the videos contain the loading and unloading process of the beam, for each video 2 frames are selected: one in which the beam is unloaded and the other in which it is loaded.

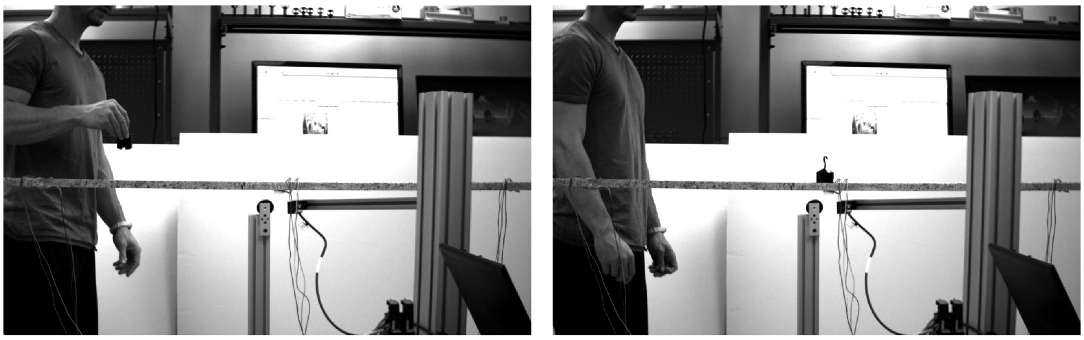

(a) Unloaded beam (b) Loaded beam

Figure 5.2: *Frames taken from the video*

As it can be seen in figure 5.2, due to the small size of the laboratory, the camera was only able to frame half of the beam, from section $\frac{L}{2}$ to section $\frac{3L}{4}$. Calculating the displacement of the beam by applying IIM functions would not be effective, or the data thus obtained would be too noisy. This is why image pre-processing is necessary. Four main operations are performed:

1. image cutting;
2. selection of the ROI;

3. black weight remotion;
4. correct illumination differences between the two images.

The purpose of the first and second operations is the same, i.e. to focus the displacement calculation on the beam only. While image cutting is performed more roughly removing entire portions of the image, ROI selection is performed more precisely and is carried out by a function created specifically for each case study via the *Image Segmenter App* in Matlab [32]. It is at this phase that any occlusions, such as the laser support system, are removed. It is specified that although these operations are performed on both images, they are defined from the image of the unloaded beam. Therefore, the only information needed to correctly perform the first two steps of image pre-processing are the shape of the structure before loading and the intensity of the expected displacement: if the cutting operation is too pronounced, there is a risk of cutting off portions of the beam in the loaded image.
The third operation is only performed for cases where the load is applied with weights equal to or less than $0.5\,\mathrm{kg}$. These are removed to facilitate IIM, as the weights are only present in the frame in which the beam is loaded.
The last step is a common pre-processing step in the IIM algorithms and it's performed using histogram matching.

(a) Unloaded beam

(b) Loaded beam

Figure 5.3: *Post-processed frames*

Calculation of punctual displacements

Having pre-processed the images, the pixel windows whose displacement is to be calculated are selected. The reason for not selecting a single pixel is always data noise. In fact, it is common practice to calculate the displacement of a window of pixels and to refer the calculated displacement to the central pixel of the window. In this operation, the assumption made is that neighboring pixels undergo the same displacement. There are three aspects to consider:

- select frame pixels of the unloaded beam;
- select an odd number of pixels constituting the window in both horizontal and vertical directions;
- select the pixels that belong to the beam.

Each pixel window consists horizontally of 7 pixels, and vertically of a number of 15 or 17.

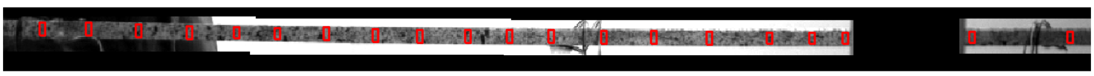

Figure 5.4: *Pixel windows*

Once the image processing phase is complete, the displacements of all image points, in terms of pixels, are calculated with the IIM algorithm using the Matlab function **imregdemons**. The Matlab command provided is

$$D = \textbf{imregdemons}\left(loaded, unloaded, [500, 400, 200], 'AccumulatedFieldSmoothing', 1.3\right)$$

where:

- *loaded* and *unloaded* are the loaded and unloaded processed images respectively;
- $[500, 400, 200]$ are the number of pyramid iterations performed: 500 at low quality, 400 at medium quality, and 200 at high quality. Pyramid iteration substantially reduces calculation time;
- $('AccumulatedFieldSmoothing', 1.3)$ is the smoothing applied at each iteration. The *imregdemons* function applies the standard deviation of the Gaussian smoothing to regularize the accumulated field at each iteration; 1.3 is its value [32].

To work, input images must be converted to greyscale, which is done via the Matlab function **im2gray**.
The *imregdemons* function is based on Thirion's demons method: the function receives the two images as input and estimates the displacement field D that aligns the loaded beam with the unloaded beam. As output, the function provides the displacement matrix D; this matrix has a number of rows and columns equal to the number of pixels of the input images, and a number of dimensions equal to the displacement field to be calculated. In the present case, the matrix D is two-dimensional, but the function can also be used to calculate displacements in space.
Let M be the number of pixels in the vertical direction and N the number of pixels in the horizontal direction, the matrix:

- $D(M, N, 1)$ contains the displacements of all pixels of the deformed beam image in the z direction;
- $D(M, N, 2)$ contains the displacements of all pixels of the deformed beam image in the y direction;

Since one is only interested in the vertical displacements, only the $D(M, N, 2)$ matrix was used.
Having selected the pixel windows and knowing the displacement of each pixel in the image, the displacement of the pixel windows is calculated. The displacement of each pixel is referred to as the central pixel of the window in terms of the median, as it provides better results than other operators.
Since the calculated displacements are referred to in terms of pixels, a pixel-displacement conversion in millimeters is performed using the following proportion

$$Displacement_{pixel} : N_{pixel} = y : \frac{L}{2}$$

where N_{pixel} is the number of pixels which corresponds to half beam length $\left(\frac{L}{2}\right)$, while y is the displacement expressed in millimeters.
Since the displacement data in possession only refer to the section $\left[\frac{L}{4}; \frac{3L}{4}\right]$, it is assumed that at

the ends of the beam ($z = 0$ and $z = L$), the displacements are zero. The assumption is that the experimental hinge or clamp constraints are ideal. The calculated displacements are shown in figure 5.5.

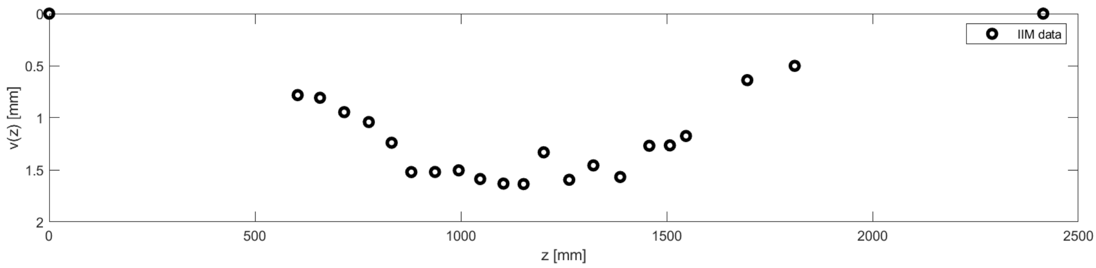

Figure 5.5: *Displacement punctual data*

Displacement interpolation

Having to calculate the function $v(z)$, the data found have to be interpolated. The interpolating function must fulfill the following characteristics:

- interpolation of data without a priori knowledge of the applied loads;
- noise removal.

With reference to image 5.5, it can be seen that the displacements obtained are very noisy, which is why an exact interpolation would not be able to provide an accurate $v(z)$ function. The functions that are able to fulfill the mentioned conditions are the *smoothing spline*. The smoothing splines are continuous piece-wise polynomials (of degree 3 or 5) in the defined interval that do not perfectly interpolate the input data as the coefficients describing them are determined by minimizing the sum of two terms,

$$\underbrace{p \sum_{i=0}^{n} w_i \left(y_i - s\left(z_i\right)\right)^2}_{\text{errore measure}} + (1-p) \underbrace{\int \lambda\left(t\right) \left(\frac{d^2 s}{dz^2}\right)^2 dz}_{\text{roughness measure}} \tag{5.1}$$

where:

- z_i e y_i are respectively the z-coordinate and the displacement v of the ith element of the image data vector;
- $n + 1$ is the number of elements of the vector;
- $s(z_i)$ is the smoothing spline interpolating the data z_i;
- w_i are the weighting coefficient values;
- λ is the regulation parameter;
- p is the smoothing parameter.

The p parameter can assume values between 0 and 1 ($0 \leq p \leq 1$):

- if $p = 0$ one obtains a least-squares interpolation. The error due to the interpolation is the highest and as a result the smoothest function there is, i.e. a straight line;

- if $p = 1$ the cubic spline is obtained. The error due to the 'roughness' of the function disappears, and perfect interpolation is obtained [32].

A very important aspect is that the minimization of the two terms in equation 5.1 for a fixed λ on the space of all continuously differentiable functions leads to a unique solution, and this solution is a natural cubic spline with knots at the data points [33]. Recall that the natural spline is a function whose second derivative cancels at the extremes of the interval. This aspect is particularly disadvantageous for the analyses in question since by estimating the displacement with smoothing splines and then deriving twice to obtain the strains, these will always be zero at the extremes. The problem is due to the fact that if there are clamps, where one would expect a maximum or at least high strain, this is actually zero. For this reason, countermeasures must be taken to overcome this limit. More information on how smoothing splines are calculated can be found in Appendix B.
The smoothing spline in Matlab are obtained using the **fit** function,

$$[curve, \tilde{}\ , output] = \textbf{fit}\,(z, y, 'smoothingspline')$$

where:

- z and y are the input data;
- *curve* is a *cfit* object;
- *output* is a structure array that contains the used smoothing parameter and the residuals.

Using the command *coeffvals* $=$ **coeffvalues**$(curve)$, the output *coeffvals* is a structure array that contains the degree of the polynomials used for interpolation, the polynomial coefficients for each interval, and the breakpoints of each interval. Since the degree of the polynomials used for interpolation is known a priori (they are all third-degree polynomials), the polynomial coefficients and the breakpoints allow the computation of $v(z)$.
Applying smoothing spline to the displacement data results in the following interpolation,

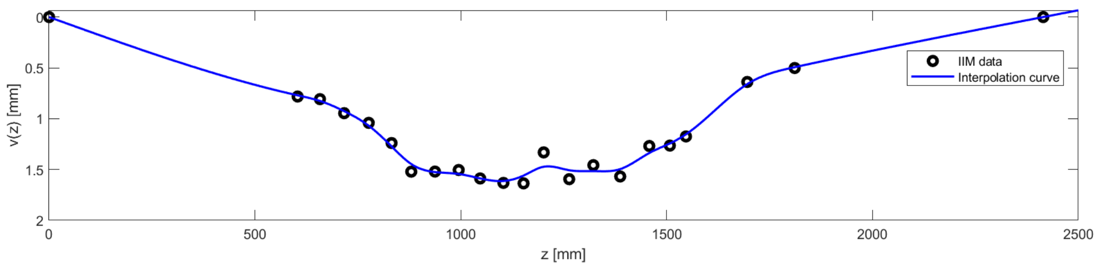

Figure 5.6: *First Interpolation*

Since some data are so noisy that they worsen the interpolation, they are removed by evaluating the residuals. The residual $i-th$, res_i, is defined as the difference between the interpolating function curve, $s(z_i)$, in the datum z_i and the displacement of the datum $y(z_i)$,

$$res_i = s(z_i) - y(z_i)$$

The residuals are used to perform an iterative interpolation by means of spline smoothing. The steps of the algorithm are described in figure 5.7,

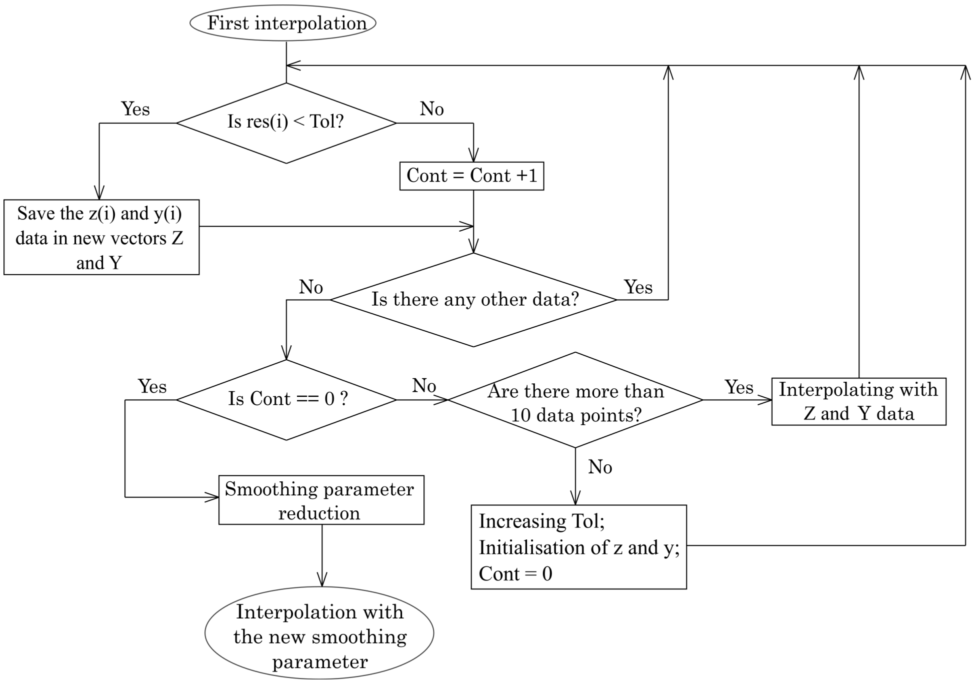

Figure 5.7: *Displacement calculation flowchart*

An initial interpolation is performed by querying the residuals in the output. Then all residuals are reviewed: if they are greater than a certain tolerance $(0.05\,\mathrm{mm})$ then the data associated with the residuals are discarded, otherwise, they are kept. This cycle is executed until the interpolation is such that there are no more residues greater than the set tolerance. This iterative interpolation removes excessively noisy data that would worsen the interpolating function $f(z)$. It may happen that after each interpolation there is at least one residue until only one input data remains. To avoid this happening, a minimum number of points for which interpolation is performed is defined: 10 for both experiments. If the number of points available is less than this threshold, then the tolerance is increased of $0.01\,\mathrm{mm}$. For this reason, the initial input data are stored in variables before starting the interpolation so that the cycle can start again with a higher tolerance and the starting data.
At the end of the interpolation, the smoothing parameter used is queried, reduced, and the interpolation is performed with the new smoothing parameter, this time provided as input with the following command,

$$[curve, \tilde{}\,, output] = \mathbf{fit}\,(z, y, 'smoothingspline', 'SmoothingParam', p)$$

This operation causes the error due to the fitting of the data (equation 5.1) slightly to increase, while the error due to the roughness of the function is greatly reduced. The choice of losing precision in the IIM data but obtaining a more smooth function allows the accuracy of the strain field to be increased. Furthermore, this choice is also motivated by the fact that the displacement of the beam will be improved with the information provided by the strain gauges, so it is preferred to lose the accuracy of the displacements provided by the IIM if this results in an improvement of the strain field. At the end of the iterations, the following interpolating function $v(z)$ is derived,

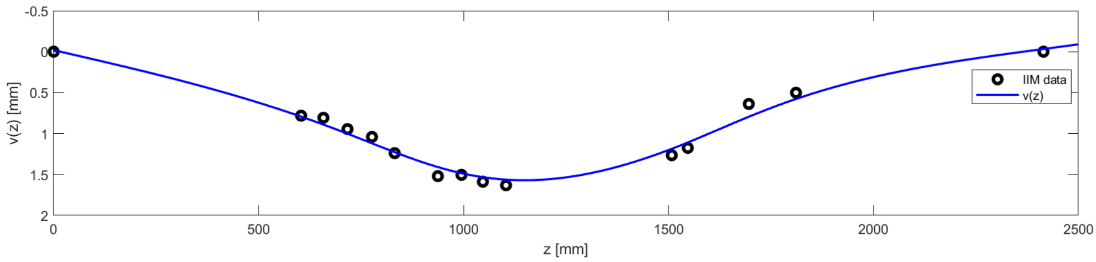

Figure 5.8: *$v(z)$ displacement function*

5.1.2 Computation of $\varepsilon(z)$

The output of the final interpolation is a data structure containing the coefficients of the polynomials used for the interpolation, their degree, and the intervals in which they are defined. In order to go from displacements to strains, it is necessary to derive these polynomials but to do so, the law that links them must be defined. The strains can be expressed by combining Hooke's law with Navier's law in the case of principal axes of inertia, these being known,

$$\varepsilon_z = \frac{N_z(z)}{EA} + \frac{M_x(z)}{EI_x}Y - \frac{M_y(z)}{EI_y}X \tag{5.2}$$

with:

- A the cross-sectional area;
- I_x and I_y respectively, the moments of inertia of the section about the x-axis and the y-axis;
- $N_z(z)$ the axial force;
- $M_x(z)$ and $M_y(z)$ the bending moments about the x and y axes;
- X and Y the distances from the origin of the principal reference system along the X and Y axes, respectively.

Since the beam is only loaded with shear forces acting in the y direction, $N_z(z)$ and $M_y(z)$ are zero. Hence Navier's law reduces to

$$\varepsilon_z(z) = \frac{M_x(z)}{EI_x}Y \tag{5.3}$$

The displacements are introduced by means of the beam's elastic line equation if the deflection due to shear forces and normal stress is neglected. This assumption is valid because for slender beams it is the bending moment that constitutes the major contribution. The equation of the elastic line is

$$M_x(z) \approx -EI_x\frac{d^2v}{dz^2} \tag{5.4}$$

where the approximation symbol is due to the assumptions made. Substituting the bending moment expression in the equation 5.4 into the equation 5.3 yields the displacement-strain relationship sought

$$\frac{d^2v}{dz^2} = -\frac{\varepsilon(z)}{Y} \tag{5.5}$$

Knowing the displacement-strain relationship and the functions describing the displacement, the strain field $\varepsilon_z(z)$ is obtained.

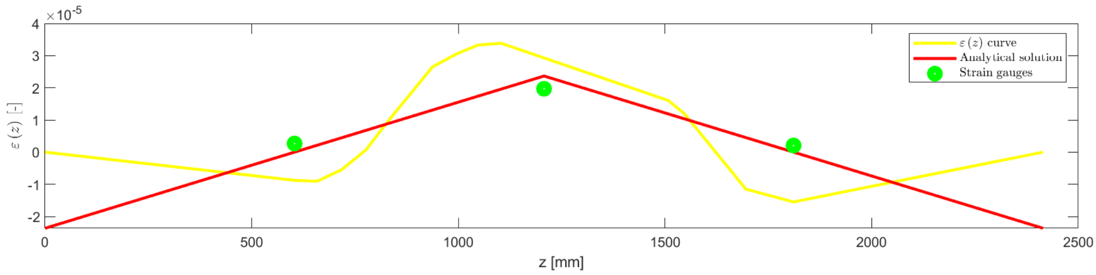

Figure 5.9: *$\varepsilon(z)$ strain function*

It is observed that since the smoothing splines are continuous cubic polynomials at intervals, the deformations are continuous straight lines at intervals. It is also noted that smoothing splines always have zero-second derivatives at the extremes of the interval, which leads to high errors in the case of clamp constraint.

5.1.3 Computation of $\varepsilon_{fix}(z)$

In order to correct the strain field $\varepsilon(z)$ by means of the values provided by the strain gauges, an interpolation by means of smoothing splines is again performed, but this time in a different way. In figure 5.10 is shown the flowchart of the used algorithm.

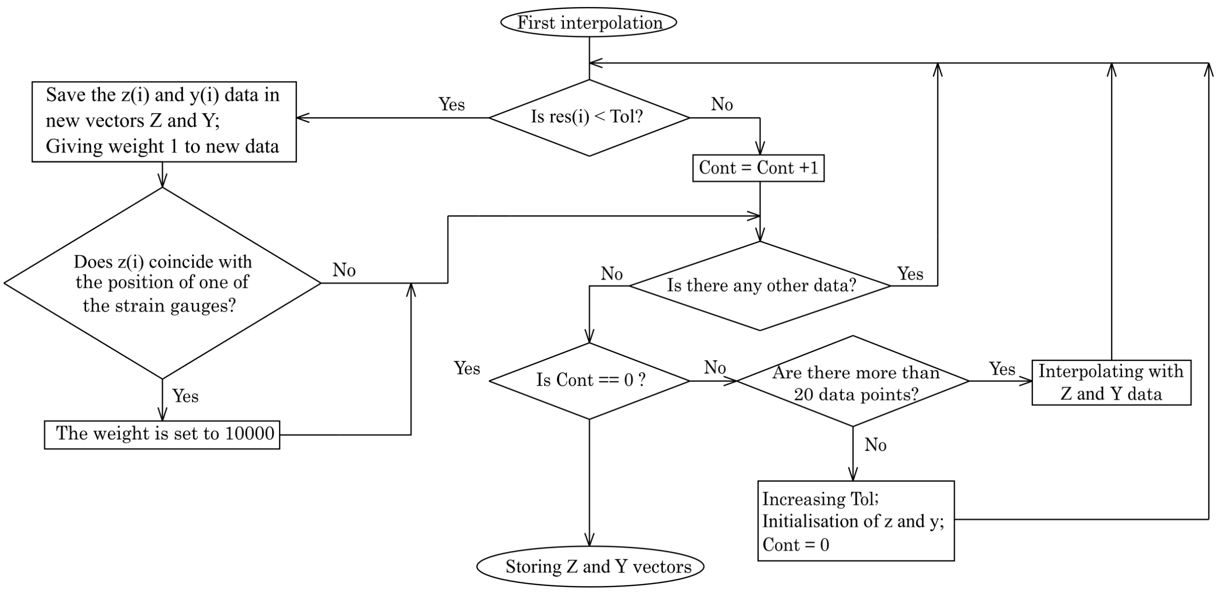

Figure 5.10: *Strain field correction flowchart*

The input data for the interpolation are extrapolated from the function $\varepsilon(z)$. The values $\varepsilon(z)$ are chosen so that the abscissae z are spaced by a constant value equal to $\frac{L}{32}$. In this way, 33 input values are obtained. At this point, the values of the function $\varepsilon(z)$ at the abscissae $\frac{L}{4}$, $\frac{L}{2}$ and $\frac{3L}{4}$ are substituted with the corresponding values of the strain gauges. Before performing the first interpolation, the vector of weights W is defined: this vector has the same dimension as the data to be interpolated and is worth 1 everywhere except where there are strain gauge values, where it is worth 10000. By interpolating with the smoothing splines and forcing them to pass through the strain gauge value, the strain field improves and any $\varepsilon(z)$ value that worsened the trend is removed. To perform this interpolation, the following Matlab command has been used,

$$[curve, \tilde{}\ , output] = \mathbf{fit}\,(z, y, 'smoothingspline', 'Weight', W) \tag{5.6}$$

It should be specified that the purpose of this interpolation is to improve the strain field $\varepsilon(z)$ by removing values too far from the strain gauge values.

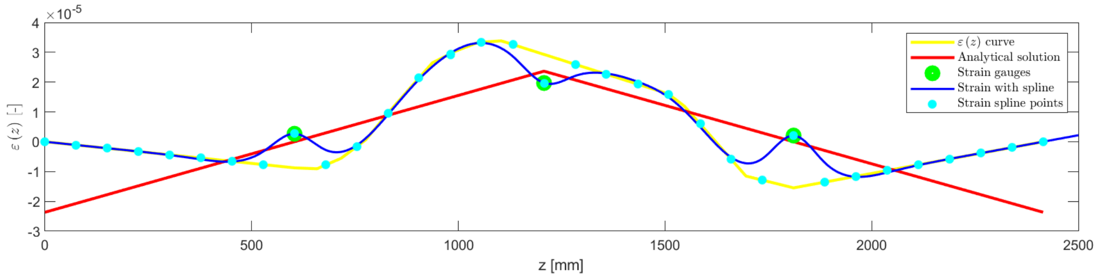

Figure 5.11: $\varepsilon_{fix}(z)$: *First interpolation*

In figure 5.11:

- the yellow curve is the strain field $\varepsilon(z)$ derived from the displacements function $v(z)$;
- the red curve is the strain analytical solution;
- the green dots are the strain gauge values;
- the light-blue dots are the input data used for the first interpolation;
- the blue curve is the first smoothing spline that fits the data.

By the very way this procedure is constructed, the correction takes place mostly around the strain gauges. Another important aspect is that the output of this operation is not the smoothing spline but the final data z and y of the iterative interpolation. The latter is constructed identically to that used to calculate the displacement field except for one aspect: the dimensions and values of the vector of weights are also updated so that the strain gauges always weigh 10000, and the others weigh 1.
At the end of the interpolation, the vectors z and ε_{fix} are obtained which define the corrected strain field $\varepsilon_{fix}(z)$. Since the final objective is to calculate the displacement field $v_{fix}(z)$, the function $\varepsilon_{fix}(z)$ is defined so that it is integrable. To this end, it is necessary to know the individual functions constituting $\varepsilon_{fix}(z)$ and the traits in which they are defined. Being given the vectors z and ε_{fix} and knowing that $\varepsilon_{fix}(z)$ has a linear trend at intervals, it is sufficient to check in which points the slope change occurs at and memorize them. Then it is sufficient to calculate the straight lines that pass between the points just calculated.

The Matlab function **ischange** is used to recognize the points at which the data change their slope. By calculating the straight lines passing through these points, the trend described in figure 5.12 is obtained,

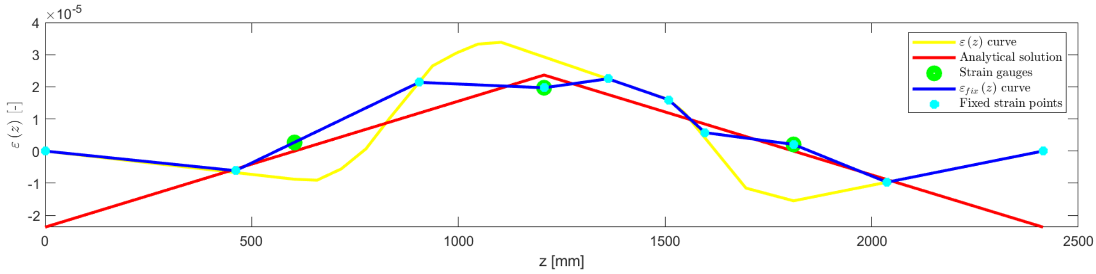

Figure 5.12: $\varepsilon_{fix}(z)$ *strain function*

In figure 5.12 the yellow curve is the strain field $\varepsilon(z)$ derived from the displacements function $v(z)$, while the blue curve is the corrected strain curve $\varepsilon_{fix}(z)$. Even after calculating $\varepsilon_{fix}(z)$, the strains at the extremes continue to be zero.

5.1.4 Computation of $v_{fix}(z)$

Once $\varepsilon_{fix}(z)$ has been calculated, it is possible to integrate it to calculate the corrected displacement function $v_{fix}(z)$. $\varepsilon_{fix}(z)$ is a linear function in traits, so each trait $\varepsilon_{fix,i}(z)$ is defined, in the interval $z \in [z_i; z_{i+1}]$, as follows:

$$\varepsilon_{fix,i}(z) = a_i'z + b_i' \tag{5.7}$$

where:

- a_i' is the angular coefficient;
- b_i' is the known term.

By double integrating the equation 5.5 for the *i-th* trait, the following is written

$$v_{fix,i}(z) = -\frac{\varepsilon_{fix,i}(z)}{Y}\frac{z^2}{2} + C_i z + D_i \tag{5.8}$$

This expression is valid for every subdomain of definition of $\varepsilon_{fix}(z)$. Furthermore, by substituting the equation 5.7 in the equation 5.8

$$v_{fix,i}(z) = a_i\frac{z^3}{6} + b_i\frac{z^2}{2} + C_i z + D_i \tag{5.9}$$

where:

- $a_i = -\frac{a_i'}{Y}$ is known;
- $b_i = -\frac{b_i'}{Y}$ is known.

The double integration of the single trait $\varepsilon_{fix,i}(z)$ leads to the appearance of the 2 constants C_i and D_i. Let N be the number of sections into which $\varepsilon_{fix}(z)$ is constituted, then there are $2 \cdot N$ unknowns over the entire interval, so $2 \cdot N$ conditions are required to solve the integration. The conditions are:

1. 2 boundary conditions ($v_{fix}(z = 0) = 0$ and $v_{fix}(z = L) = 0$);
2. $N - 1$ continuity conditions of the displacement $v_{fix}(z)$;
3. $N - 1$ continuity conditions of the displacement derivative $v'_{fix}(z)$;

While condition 2 guarantees that the displacement is equal at each node connecting two straight lines, condition 3 guarantees that the slope is also equal at that point. Therefore

$$2 + (N - 1) \cdot 2 = 2 \cdot N$$

conditions are available.
Assume to be in the first section $N = 1$, at the point location $z = z_2$. Conditions 2 and 3 are written:

$$\begin{cases} v_1(z = z_2) = v_2(z = z_2) \\ v'_1(z = z_2) = v'_2(z = z_2) \end{cases} \tag{5.10}$$

from which explicating:

$$\begin{cases} a_1\frac{z_2^3}{6} + b_1\frac{z_2^2}{2} + C_1 z_2 + D_1 & = a_2\frac{z_2^3}{6} + b_2\frac{z_2^2}{2} + C_2 z_2 + D_2 \\ a_1\frac{z_2^2}{2} + b_1 z_2 + C_1 & = a_2\frac{z_2^2}{2} + b_2 z_2 + C_2 \end{cases} \tag{5.11}$$

Rearranging so that the unknowns (integration constants) are at the first member and the known terms at the second, leads to

$$\begin{cases} C_1 z_2 + D_1 - C_2 z_2 - D_2 & = a_2\frac{z_2^3}{6} + b_2\frac{z_2^2}{2} - a_1\frac{z_2^3}{6} - b_1\frac{z_2^2}{2} \\ C_1 - C_2 & = a_2\frac{z_2^2}{2} + b_2 z_2 - a_1\frac{z_2^2}{2} - b_1 z_2 \end{cases} \tag{5.12}$$

Since these conditions are written for every breakpoint (except $z = 0$ and $z = L$), a linear system of the type $[A]\{x\} = \{s\}$ is constructed, with:

- $[A]$ matrix of the coefficients of the unknowns;
- $\{s\}$ vector of known terms;
- $\{x\}$ vector of unknowns.

Solving the system yields the integration constants of each section, and thus the displacement field $v_{fix}(z)$ is obtained

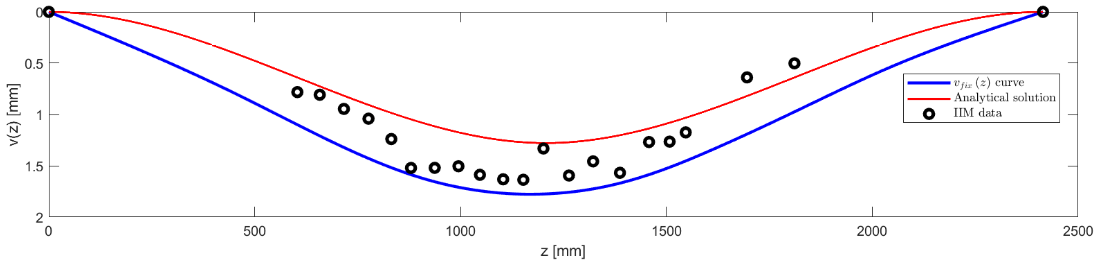

Figure 5.13: v_{fiz} *displacement function*

In the case where the roller is also present, the problem has an internal hyperstaticity. Hyperstaticity implies that an additional condition must be imposed in the location of the roller, which can be either that the displacement is zero at $z = z_{roller}$, or that the displacement is equal to that provided by the interpolating function $v(z)$ in $z = z_{roller}$ (chosen condition), where z_{roller} is the location of the roller. Consequently, the number of constants to be determined is always $2 \cdot N$, while the number of conditions becomes $(2 \cdot N + 1)$. The resulting displacement field $v_{fix}(z)$ will have 3 different types of errors depending on the $(2 \cdot N + 1)_{th}$ condition that is **not** imposed. Let $v_{roller-1}(z)$ and $v_{roller}(z)$ be the displacement functions in the sections before and after the breakpoint z_{roller} respectively, then the 3 conditions that can be imposed in z_{roller} are:

1. continuity of the displacement $v_{roller-1}(z_{roller}) = v_{roller}(z_{roller})$;
2. continuity of rotation $v'_{roller-1}(z_{roller}) = v'_{roller}(z_{roller})$;
3. displacement provided by the function $v(z) \rightarrow v_{roller-1} = v(z_{roller})$.

If condition 1 is not imposed, then there would be a discontinuity of the displacement, while the slope of the sections $v_{roller-1}(z)$ and $v_{roller}(z)$ would be respected.
If condition 2 is not imposed, the displacements would be continuous and equal to $v(z_{roller})$, but z_{roller} would be an angular point.
If condition 3 is not imposed, the displacement and the rotation at z_{roller} would be continuous, but the value of the displacement at that point would be that resulting from the integration.
In the case where the strain field to be integrated $\varepsilon_{fix}(z)$ is the correct one, the resulting displacement field $v_{fix}(z)$ would be the correct one even if $2 \cdot N$ conditions were used. In the present case, the strains $\varepsilon_{fix}(z)$ are not the exact ones, so it is necessary to remove one of the 3 conditions mentioned above. After testing the integration in all 3 ways, it was observed that the best choice is to exclude condition number 2, as the errors made in the other two cases are far greater.

A final observation concerns cases where the beam is clamped at both ends. In these cases, the beam is twice hyperstatic (3 times, if the roller is also present). In these cases too, it was decided to impose the condition of zero displacements and not zero rotations as boundary conditions.

5.1.5 Changes for the second experiment

For the second experiment, some modifications due to the different kind of problem were made to the algorithm.

The first change concerned the choice of pixels whose displacement was to be calculated using the IIM method. When the beam was painted, paper tapes were placed both on the strain gauges to prevent the paint from getting on them and on some sections of the beam to collect the strain gauge cables in order to limit their bulk. As some of the cables became disconnected during this procedure, once the beam was tied down, the tapes were removed so that the connection between the strain gauges and the electrical cables could be re-established. As a result, at the root of the beam, there was a portion of the surface that was free of paint. In contrast, the free end of the beam, despite being painted, is highly overexposed due to the light required for the DIC technique. These two regions have been highlighted with red rectangles in figure 5.14.

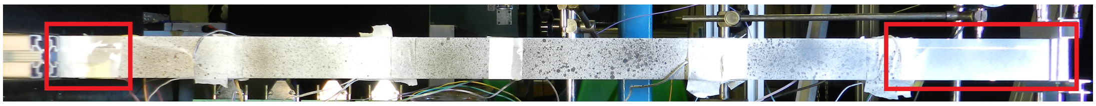

Figure 5.14: *Image took by the IIM camera from test 1*

Calculating the displacement of the beam at $z = 0\,\mathrm{mm}$ would be very difficult, especially because of the high pixel intensity due to reflection. For this reason, a zero displacement was assumed at $z = 0\,\mathrm{mm}$. On the other hand, excessive brightness in the ROI of DIC not only makes it impossible to calculate the displacements in this region, which are out of scale, but also worsens the entire correspondence between the undeformed and deformed image. For this reason, this region was masked, as can be seen in figure 5.15.

Figure 5.15: *Experiment 2 - Pre-processed image*

By excluding this area with a mask, the IIM method improves with more precise calculated displacements; however, the displacements are calculated on a lower domain of $z \in [0; L]$. In order to overcome this problem, a zero strain has been assumed at the free end of the beam: in this way, the integer domain of the beam $(z \in [0; L])$ is re-established. The algorithm presented was developed to reconstruct the deformation of the structure without any assumptions about the loads. Instead, the above hypothesis presupposes knowledge of the loads acting on the structure. Unfortunately, this choice was made necessary due to the presence of very bright light, the latter being essential for the DIC to function correctly. On the other hand, if the DIC had not been necessary, this problem would not have arisen. Furthermore, the imposition of zero strain on the tip fits perfectly into the strain correction phase.
In this experiment, all strain gauges were oriented along $\pm 45°$ directions, except for the root strain gauges. The strain-displacement relationship (equation 5.5) allows to derive the axial strain field $\varepsilon(z)$ from the displacement field $v(z)$. In order to improve the strain field, strain measurements must be reported in terms of axial strains, and not along $\pm 45°$ directions. This conversion was done by solving the equation 2.24, which is given here, for each strain measurement station,

$$\begin{aligned}\varepsilon^*(x,c,\beta) &= (e_1(x)+e_2(x)z(c)+e_3(x)y(c))\left[\cos^2\beta-\nu\sin^2\beta\right]+\\&+\left(\frac{1}{k_{\varepsilon z}}e_4(x)f_1(c)+\frac{1}{k_{\varepsilon y}}e_5(x)f_2(c)+e_6(x)f_3(c)\right)\cos\beta\sin\beta\end{aligned}$$

To solve the single equation, 6 strain measurements are required for each section, but only 3 are available in the experimental test. But, having loaded the beam in the shear center along the x-axis, the terms $e_3(x), e_5(x)$ and $e_6(x)$ are zero. Therefore the equation 2.24 is simplified and becomes,

$$\varepsilon^*(x,c,\beta)=(e_1(x)+e_2(x)z(c))\left[\cos^2\beta-\nu\sin^2\beta\right]+\left(\frac{1}{k_{\varepsilon z}}e_4(x)f_1(c)\right)\cos\beta\sin\beta \tag{5.13}$$

Since there are 3 strain gauges in each strain measurement section, it is possible to determine $e_1(x), e_2(x)$ and $e_3(x)$ by imposing a linear system. Once these are computed, it is possible to determine $\varepsilon^*(x,c,\beta)$ for any value of β. Since one is interested in the axial strains, the following is written,

$$\varepsilon^*(x,c,0^\circ)=e_1(x)+e_2(x)z(c) \tag{5.14}$$

The equation 5.14 is written in the reference system of figure 2.1. By readjusting the equation 5.14 to the reference system of the problem under consideration (figure 4.10), it becomes

$$\varepsilon^*(z,x,0^\circ)=e_1(z)-e_2(z)y(x) \tag{5.15}$$

Knowing the values of e_1 and e_2 for each section where the strain gauges are positioned $\left(\frac{L}{6};\frac{L}{3};\frac{2L}{3};\frac{5L}{6}\right)$, and knowing the z-coordinate of the strain gauges, the strain gauge measurements at 45° are converted to measurements at 0°.

In the strain correction phase, the clamp strain was corrected: having available the strain measurements ε_1 and ε_2 calculated at $z_1 = 12\,\mathrm{mm}$ and $z_2 = \frac{L}{6}$, respectively, by extending the line passing through the pairs of points $(z_1,\varepsilon_1)-(z_2,\varepsilon_2)$, the strain in the clamped section was computed. Finally, to make the strain correction effective, a weight of 10000, for the weighted interpolation purpose, is also associated to the strains in the clamp section and the free end. In this way, strain measurements at the clamped and free end are treated as if they were strain gauge measurements. If this was not done in this way, on the one hand, the strain at the clamped section could take on values halfway between the real value and the null value, thus committing high errors; on the other hand, there would be the risk that the iterative correction could remove the strain at the free end, with the consequence of obtaining a displacement and strain field defined on a domain lower than that $z \in [0; L]$.
The last modification made to the algorithm for the second experiment concerns the definition of the linear system for the double integration of $\varepsilon_{fix}(z)$. In this case, the boundary conditions are no longer those of simple support but those of clamp, so the boundary conditions change and become,

$$\underbrace{v_{fix}\left(z=0\right)=v_{fix}\left(z=L\right)=0}_{\text{simply supported beam}} \Rightarrow \underbrace{v_{fix}\left(z=0\right)=v'_{fix}\left(z=0\right)=0}_{\text{clamped beam}}$$

5.2 Second method

The second method differs from the first after the calculation of the strain field $\varepsilon_{fix}(z)$. Once the latter has been calculated, it is possible to feed the iFEM not only with the values provided by the strain gauges but also with other values provided by the function $\varepsilon_{fix}(z)$. This type of data fusion goes well with the iFEM for two reasons:

1. with the same number of strain gauges, with data fusion it is possible to provide the iFEM with a larger number of sections providing more strain measurements;
2. even if the strain field $\varepsilon_{fix}(z)$ is not as accurate as the strain gauges, through the appropriate choice of the error coefficients w_k^0 it is possible to assign to the strain gauges a unit weight and to the measurements coming from the field $\varepsilon_{fix}(z)$ a lower weight, to take into account the different level of fidelity of the two types of strains.

5.2.1 Shape sensing $(\varepsilon_{fix}(z))$

Once the strain field $\varepsilon_{fix}(z)$ has been calculated, multiple analyses using iFEM could be performed by varying the type of inverse finite element, the number of mesh elements, the number of sections along which the strains could be evaluated and the weight coefficient associated with the sectional strains. The analyses were performed for Test 3 in the case of $m = 5\,\mathrm{kg}$.

Bernoulli-Euler beam inverse element

In the case of the Bernoulli-Euler beam, the characteristics of the iFEM analysis are shown in the table 5.1.

Case	Bernoulli-Euler Element	Sections z_i	Weight = 1	Weight = 0.5	Weight = 0.1
1	1	L/3, 2L/3	L/3, 2L/3	-	-
2	1	L/6, 5L/6	L/6, 5L/6	-	-
3	2	L/6, L/3, 2L/3, 5L/6	L/6, L/3, 2L/3, 5L/6	-	-
4,5	2	L/12, L/4, L/3, 5L/12, 7L/12, 2L/3, 3L/4, 11L/12	L/3, 2L/3	L/12, L/4, 5L/12, 7L/12, 3L/4, 11L/12	
6,7	2	L/12, L/6, L/4, 5L/12, 7L/12, 3L/4, 5L/6, 11L/12	L/6, 5L/6	L/12, L/4, 5L/12, 7L/12, 3L/4, 11L/12	
8,9	2	L/12, L/6, L/3, L/4, 5L/12, 7L/12, 2L/3, 3L/4, 5L/6, 11L/12	L/6, L/3, 2L/3, 5L/6	L/12, L/4, 5L/12, 7L/12, 3L/4, 11L/12	
10,11	3	L/12, L/6, L/3, L/4, 5L/12, 7L/12, 2L/3, 3L/4, 5L/6, 11L/12	L/6, L/3, 2L/3, 5L/6	L/12, L/4, 5L/12, 7L/12, 3L/4, 11L/12	

Table 5.1: *iFEM - Bernoulli-Euler beam*

In cases 1 to 3, no data fusion was performed, but iFEM was applied with the measurements provided by the strain gauges to the indicated sections. Furthermore, while in case 3 all strain gauge measurements were used, in cases 1 and 2 the strain gauges on the innermost and outermost sections were used, respectively. In these cases (1:3), all strain gauges were always assigned a unit weight.

Cases 4 to 11 were performed using data fusion. In all cases, a unit weight was always associated with the sectional strains at the strain gauges; at all other stations, a weight of 0.1 or 0.5 was associated. It should be noted that the sectional strains to which a lower weight was associated are precisely those derived from the strain field $\varepsilon_{fix}(z)$ at z_i positions other than the strain gauges. The difference between cases 4,5 and 6,7 are the sectional strains to which a unit weight has been associated, where the inner sections have been chosen for cases 4,5 and the outer sections for cases 6,7.

In cases 8 to 11, the same sections are used, 2 more ($z = \left(\frac{L}{3}, \frac{2L}{3}\right)$) than in cases 4 to 7. The difference between cases 8,9 and 10,11 is the number of beam elements utilized, 2 and 3 respectively.

Timoshenko beam inverse element

To use the IFEM with the Timoshenko beam element, it is necessary to provide each section z_i with six strain values. Although only 3 strain gauge measurements were available on each section, in section 5.1.5 it was seen how this problem can be bypassed. The cases analyzed with the IFEM of Timoshenko beam elements are shown in table 5.2.

Timoshenko Elements	Sections z_i	Weight = 1
1	L/3, 2L/3	L/3, 2L/3
2	L/6, L/3, 2L/3, 5L/6	L/6, L/3, 2L/3, 5L/6

Table 5.2: *iFEM - Timoshenko beam*

There are two cases analyzed. In the first, there is a single Timoshenko element with two sections, which are the internal ones; in the second, there are two elements and four sections are used.

6 Results

Once the experiments were performed, the experimental measurements provided by the sensors were processed and reported in the following sections.

6.1 Experiment 1

In the first experiment, strains were measured by strain gauges and local displacement by a laser sensor. For each case study (refer to table 4.2), tables are provided showing the values experimentally measured by the sensors, the theoretical values provided by beam theory, and the relative percentage error between the experimental and theoretical measurements. The relative percentage error, *err%*, is calculated as follow: let S_{exp} and S_{th} be the experimental and theoretical measurements respectively, then

$$err\% = \frac{S_{exp} - S_{th}}{S_{th}} \cdot 100 \tag{6.1}$$

Before reporting the results provided by the experimental measurements, it is necessary to specify that the beam, even when not subjected to concentrated loads, was obviously subjected to the weight force. Concerning the strain measurements, these were obtained by performing the difference between the beam strain in the loaded condition ε_{loaded} (which accounted for the concentrated load and the weight force) and that in the unloaded condition $\varepsilon_{unloaded}$ (weight force only),

$$\varepsilon = \varepsilon_{loaded} - \varepsilon_{unloaded} = \varepsilon_{concentrated\ load} + \varepsilon_{force\ weight} - \varepsilon_{weightforce} = \varepsilon_{concentrated\ load} \tag{6.2}$$

In this way, only the strain due to the concentrated force is measured.
For displacements, the procedure is conceptually the same, with the difference that the measurement provided by the laser sensor is its distance from the object on which the ray impinges. Therefore, as the beam is loaded, the distance to the sensor is reduced. To record a positive displacement was written,

$$y = y_{unloaded} - y_{loaded} = y_{concentrated\ load} \tag{6.3}$$

6.1.1 Experimental measurements

Each experiment of table 4.2 was repeated 3 times: this means that the reported measurements are average values.

Measurement	Location	Experimental value	Theoretical value	*err%*
Strain	$L/4$	$2.27\frac{\mu m}{m}$	$2.37\frac{\mu m}{m}$	-4.2%
Strain	$L/2$	$4.60\frac{\mu m}{m}$	$4.73\frac{\mu m}{m}$	-2.7%
Strain	$3L/4$	$2.23\frac{\mu m}{m}$	$2.37\frac{\mu m}{m}$	-5.9%
Displacement	$L/2$	$0.53\,\mathrm{mm}$	$0.51\,\mathrm{mm}$	-3.9%

Table 6.1: *Case study 01 - Subcase 1*

Measurement	Location	Experimental value	Theoretical value	*err%*
Strain	$L/4$	$9.63\frac{\mu m}{m}$	$9.46\frac{\mu m}{m}$	1.8%
Strain	$L/2$	$16.6\frac{\mu m}{m}$	$18.9\frac{\mu m}{m}$	-12.2%
Strain	$3L/4$	$9.73\frac{\mu m}{m}$	$9.46\frac{\mu m}{m}$	2.8%
Displacement	$L/2$	$2.09\,\mathrm{mm}$	$2.04\,\mathrm{mm}$	2.4%

Table 6.2: *Case study 01 - Subcase 2*

Measurement	Location	Experimental value	Theoretical value	*err%*
Strain	$L/4$	$24.3\frac{\mu m}{m}$	$23.7\frac{\mu m}{m}$	2.5%
Strain	$L/2$	$42.7\frac{\mu m}{m}$	$47.3\frac{\mu m}{m}$	-9.7%
Strain	$3L/4$	$24.6\frac{\mu m}{m}$	$23.7\frac{\mu m}{m}$	3.8%
Displacement	$L/2$	$5.16\,\mathrm{mm}$	$5.11\,\mathrm{mm}$	1.0%

Table 6.3: *Case study 01 - Subcase 3*

Measurement	Location	Experimental value	Theoretical value	*err%*
Strain	$L/4$	$14.8\frac{\mu m}{m}$	$18.9\frac{\mu m}{m}$	-21.7%
Strain	$L/2$	$19.9\frac{\mu m}{m}$	$18.9\frac{\mu m}{m}$	5.3%
Strain	$3L/4$	$18.5\frac{\mu m}{m}$	$18.9\frac{\mu m}{m}$	-2.1%
Displacement	$L/2$	$2.85\,\mathrm{mm}$	$2.81\,\mathrm{mm}$	1.4%

Table 6.4: *Case study 02*

Measurement	Location	Experimental value	Theoretical value	*err%*
Strain	$L/4$	$79.2\frac{\mu m}{m}$	$132\frac{\mu m}{m}$	-40.0%
Strain	$L/2$	$-89.5\frac{\mu m}{m}$	$-138\frac{\mu m}{m}$	-35.14%
Strain	$3L/4$	$101\frac{\mu m}{m}$	$137\frac{\mu m}{m}$	-26.3%
Displacement	$1839.9\,\mathrm{mm}$	$2.2\,\mathrm{mm}$	$2\,\mathrm{mm}$	10.0%

Table 6.5: *Case study 03 - Subcase 1*

Measurement	Location	Experimental value	Theoretical value	*err%*
Strain	$L/4$	$-32.9\frac{\mu m}{m}$	$-19.7\frac{\mu m}{m}$	67.0%
Strain	$L/2$	$-36.8\frac{\mu m}{m}$	$-65.3\frac{\mu m}{m}$	-43.5%
Strain	$3L/4$	$126\frac{\mu m}{m}$	$154\frac{\mu m}{m}$	-18.2%
Displacement	1839.9 mm	3.23 mm	2.71 mm	19.2%

Table 6.6: *Case study 03 - Subcase 2*

Measurement	Location	Experimental value	Theoretical value	*err%*
Strain	$L/4$	$2.67\frac{\mu m}{m}$	$0.00\frac{\mu m}{m}$	-
Strain	$L/2$	$19.7\frac{\mu m}{m}$	$23.7\frac{\mu m}{m}$	-16.9%
Strain	$3L/4$	$2.07\frac{\mu m}{m}$	$0.00\frac{\mu m}{m}$	-
Displacement	1260.5 mm	1.72 mm	1.27 mm	35.4%

Table 6.7: *Case study 03 - Subcase 3*

Measurement	Location	Experimental value	Theoretical value	*err%*
Strain	$L/4$	$71.5\frac{\mu m}{m}$	$162\frac{\mu m}{m}$	-55.2%
Strain	$L/2$	$-104\frac{\mu m}{m}$	$-204\frac{\mu m}{m}$	-49.0%
Strain	$3L/4$	$173\frac{\mu m}{m}$	$176\frac{\mu m}{m}$	-1.7%
Displacement	1839.9 mm	3.24 mm	3.65 mm	-11.2%

Table 6.8: *Case study 04 - Subcase 1*

Measurement	Location	Experimental value	Theoretical value	*err%*
Strain	$L/4$	$-48.5\frac{\mu m}{m}$	$-56.7\frac{\mu m}{m}$	-14.5%
Strain	$L/2$	$-46.2\frac{\mu m}{m}$	$-100\frac{\mu m}{m}$	-53.8%
Strain	$3L/4$	$210\frac{\mu m}{m}$	$228\frac{\mu m}{m}$	-7.9%
Displacement	1839.9 mm	5.02 mm	5.8 mm	-13.4%

Table 6.9: *Case study 04 - Subcase 2*

The experimentally measured strains for case study 1.1 (table 6.1) are shown for completeness. In this test, due to a small load, the strains are very low, and consequently, the accuracy of the strain gauges cannot be too precise. Nevertheless, comparing the measured values with the theoretical values reveals that their measurements are correct.
Looking at the relative percentage errors, it can be seen that only for case studies 01 and 02 the experimental measurements are in agreement with the theoretical values: the largest error is committed in case study 02 where there is an error of $|21.7\%|$ on only one strain gauge. In all the other case studies, the errors committed on displacement and strain are both quite high.
The cause of the deviation from the theoretical behavior is the fact that it was not possible to reproduce experimentally ideal clamp and roller constraints. Furthermore, having only one displacement measurement which is provided by the laser sensor, it was decided not to consider case studies 03 and 04 in the evaluation of the accuracy of method 1 as the displacements measured by the laser sensor differ too much from the analytical ones.

Another aspect to be highlighted is that in case studies 1, 2, and 3.1, due to the symmetry of the boundary conditions and loads, one would have expected the lateral strain gauges placed at $z = \frac{L}{4}$ and $z = \frac{3L}{4}$ provided the same value. Indeed, in case 2, all 3 strain gauges should have measured the same strain. The causes of these incorrect measurements may be due to:

- an incorrect alignment and/or positioning of the strain gauges;
- an incorrect positioning of weights on the beam.

The most plausible cause is the first.

6.1.2 Parametric smoothing parameter analysis

It has been said that the reduction of the smoothing parameter allows for a better strain field reconstruction. In order to select the appropriate smoothing parameter p value, parametric analyses were performed for case studies 01 and 02. In each of them, the smoothing parameter was reduced by a factor, the *smoothing parameter reduction factor* (K), ranging from 1 to 500. The best smoothing parameter p was selected as the one that allowed to compute a displacement as close as possible to that provided by the laser sensor. Below are reported the displacements computed at $z = \frac{L}{2}$ per study cases 01 and 02 as changes in K.

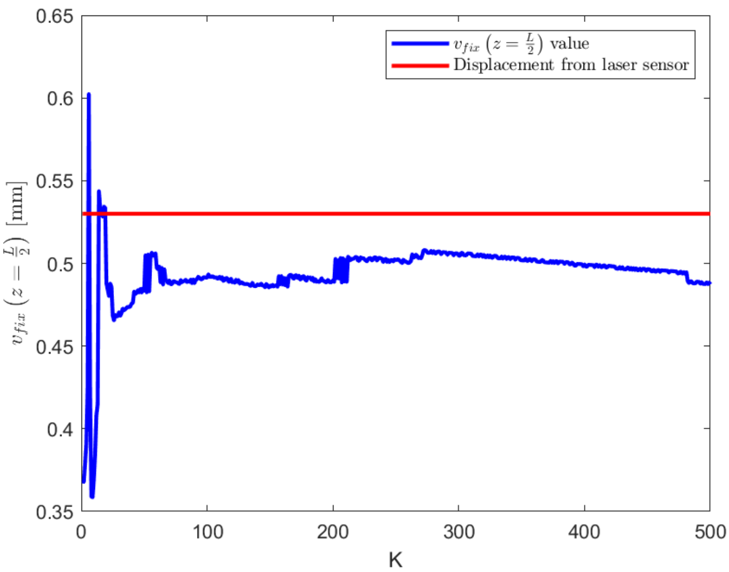

Figure 6.1: *Case study 01 subcase 1: best* $K = 17$

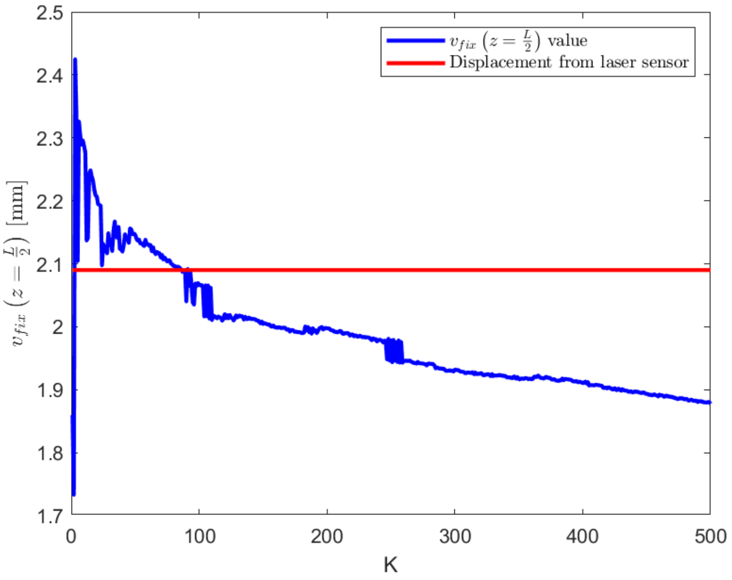

Figure 6.2: *Case study 01 subcase 2: best* $K = 88$

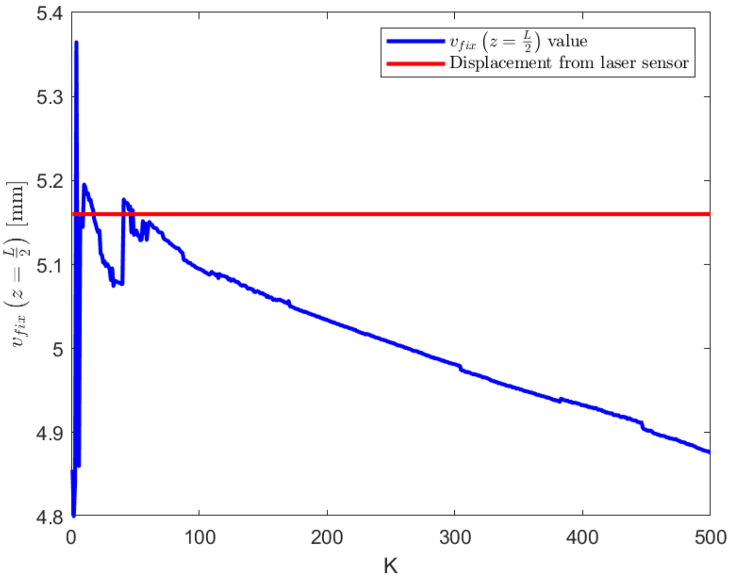

Figure 6.3: *Case study 01 subcase 3: best* $K = 7$

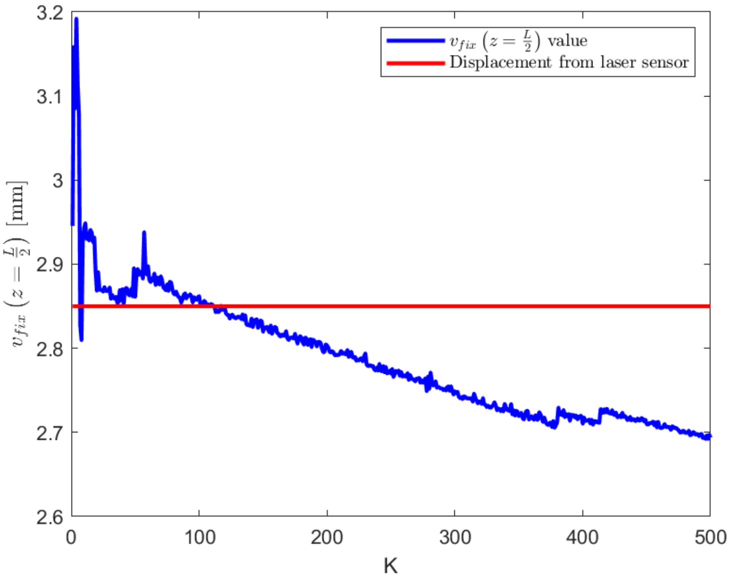

Figure 6.4: *Case study 02: best* $K = 108$

Unfortunately, the best K changes depending on the problem. Referring to the figures 6.1:6.4, two main aspects can be observed:

- for low K (< 30), the trend is swinging and unpredictable;
- as K increases (and therefore as p decreases) the error committed tends to increase.

Therefore, the best K is to be found between these two regions. The idea is to select, for each case study, all Ks for which the modulus of the absolute error committed with respect to the laser measurement is less than an imposed tolerance $(0.1\,\mathrm{mm})$. Once these Ks have been found, the one common to all case studies is sought and used for the analyses. Carrying out the above, the selected range is

$$51 \leq K \leq 87; \quad k = 57 \text{ excluded}$$

and $K = 80$ is the selected value.
The choice of the tolerance of $0.1\,\mathrm{mm}$ is due to the following considerations. Table 6.10 shows the errors made between the displacements provided by the IIM method and those provided by the laser sensor,

Case Study	Error	Error [pixel]
1.1	$-0.141\,\mathrm{mm}$	-0.130
1.2	$-0.254\,\mathrm{mm}$	-0.234
1.3	$-0.200\,\mathrm{mm}$	-0.184
2	$-0.053\,\mathrm{mm}$	-0.049

Table 6.10: *Errors between displacements provided by the IIM method and those provided by the sensor laser*

The average error committed is $-0.162\,\mathrm{mm}$. Since interpolation by smoothing splines reduces the noise of the data, the tolerance was set to a lower value.

6.1.3 Method 1 results

Below are reported the corrected displacement function $v_{fix}(z)$ and the corrected strain function $\varepsilon_{fix}(z)$ for each case study. Even though case studies 03 and 04 were not used to evaluate the developed method's goodness, their results make it possible to qualitatively observe how the algorithm acts for boundary conditions more complex than simple support. The functions $v_{fix}(z)$ and $\varepsilon_{fix}(z)$ are reported together with the analytical solution and the discrete data derived from the IIM algorithm.

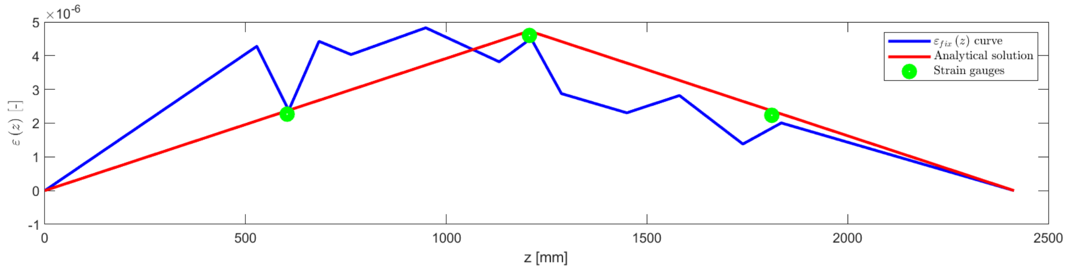

(a) $\varepsilon_{fix}(z)$ *strain function*

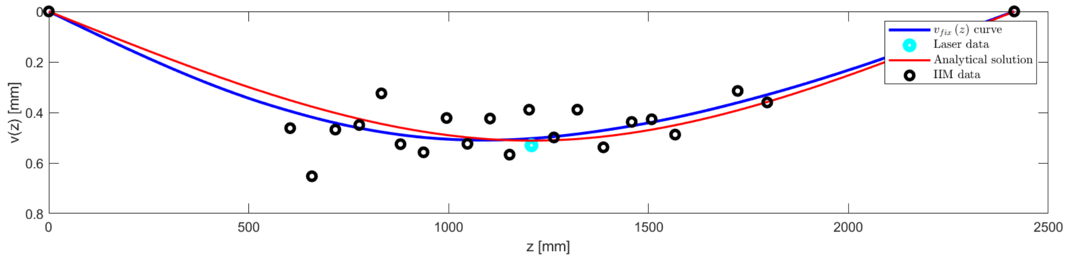

(b) $v_{fix}(z)$ *displacement function*

Figure 6.5: *Case 01 - Subcase 1*

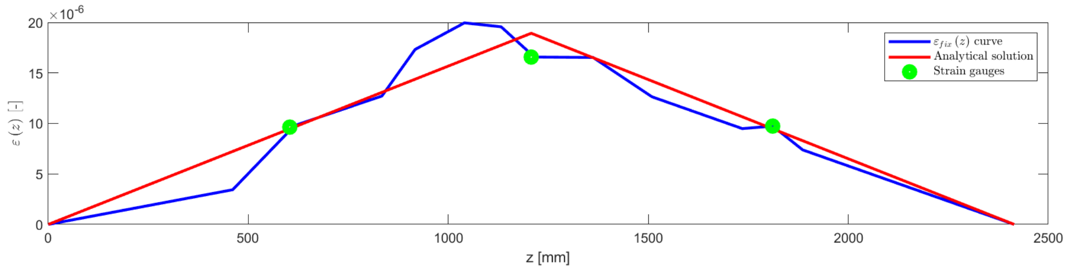

(a) $\varepsilon_{fix}(z)$ *strain function*

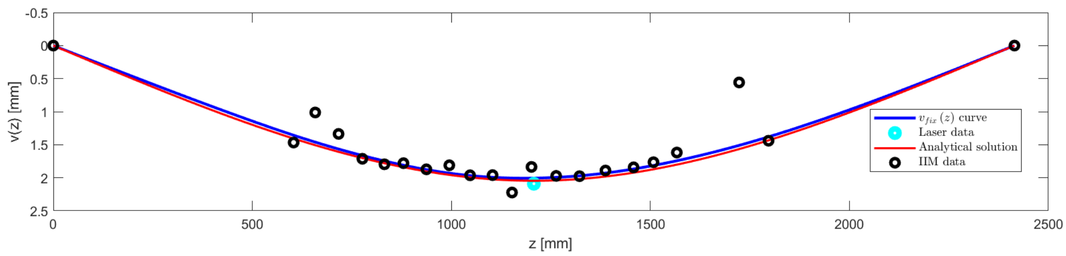

(b) $v_{fix}(z)$ *displacement function*

Figure 6.6: *Case 01 - Subcase 2*

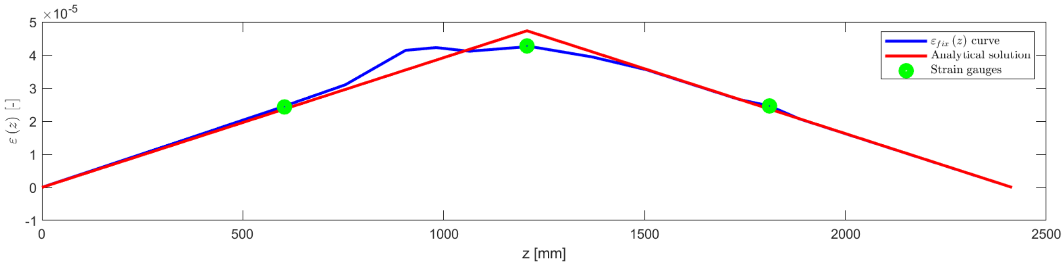

(a) $\varepsilon_{fix}(z)$ *strain function*

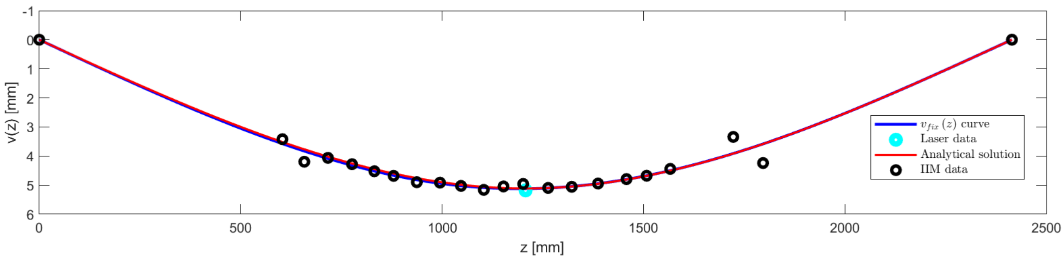

(b) $v_{fix}(z)$ *displacement function*

Figure 6.7: *Case 01 - Subcase 3*

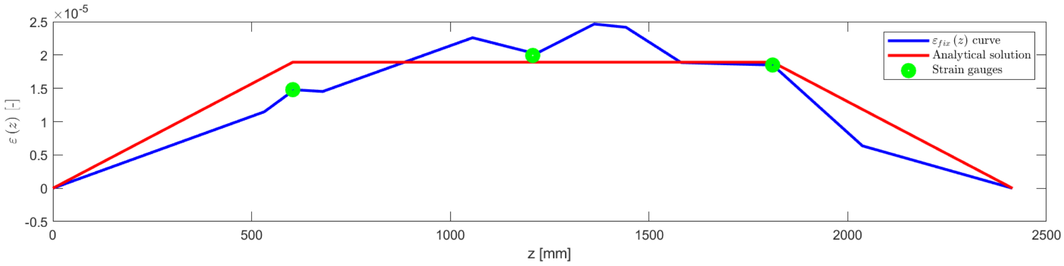

(a) $\varepsilon_{fix}(z)$ *strain function*

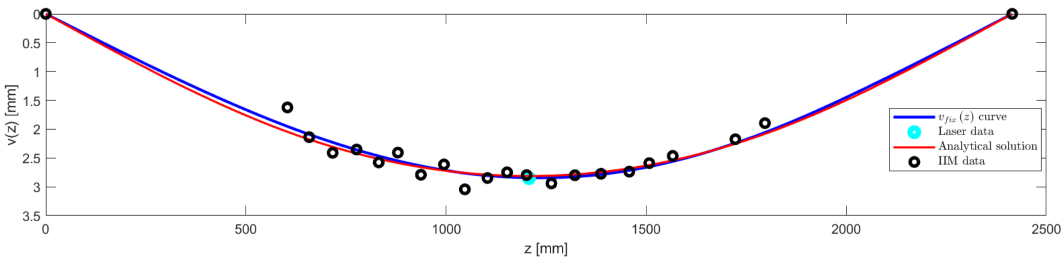

(b) $v_{fix}(z)$ *displacement function*

Figure 6.8: *Case 02*

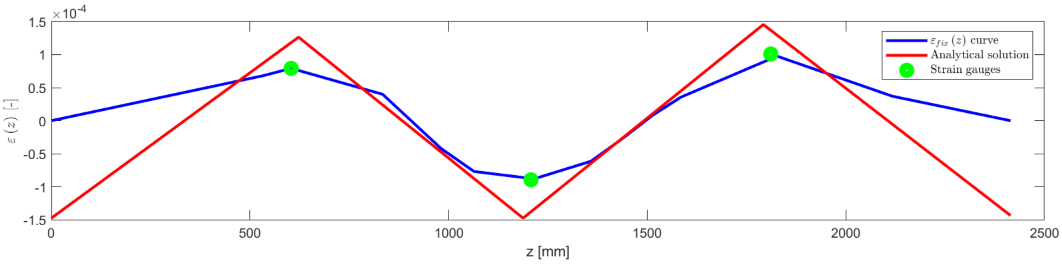

(a) $\varepsilon_{fix}(z)$ *strain function*

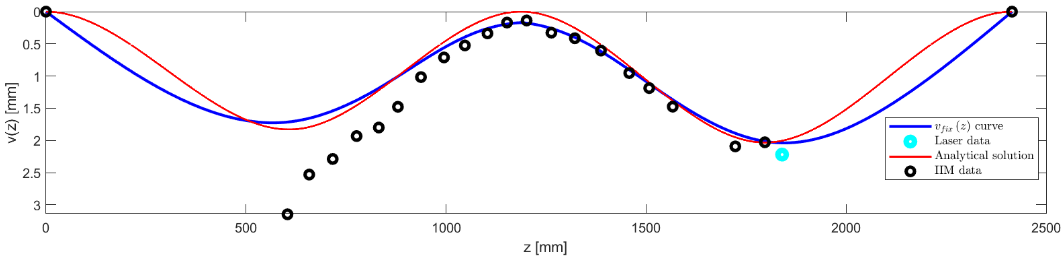

(b) $v_{fix}(z)$ *displacement function*

Figure 6.9: *Case 03 - Subcase 1*

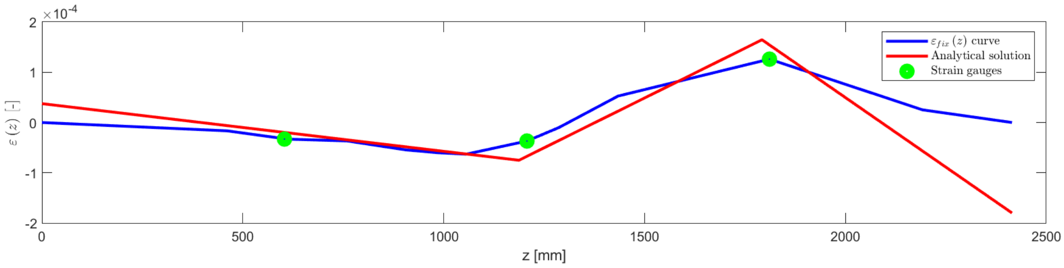

(a) $\varepsilon_{fix}(z)$ *strain function*

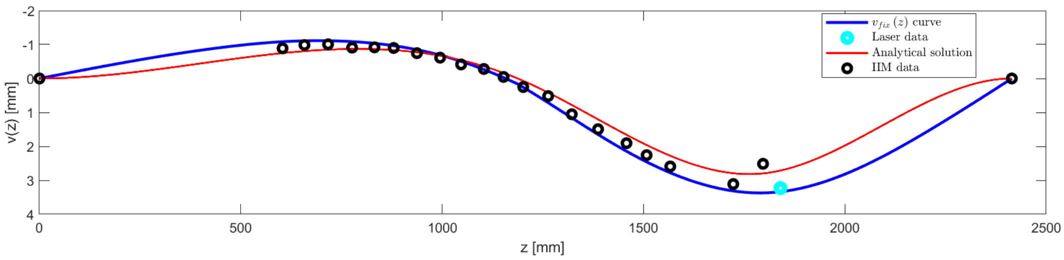

(b) $v_{fix}(z)$ *displacement function*

Figure 6.10: *Case 03 - Subcase 2*

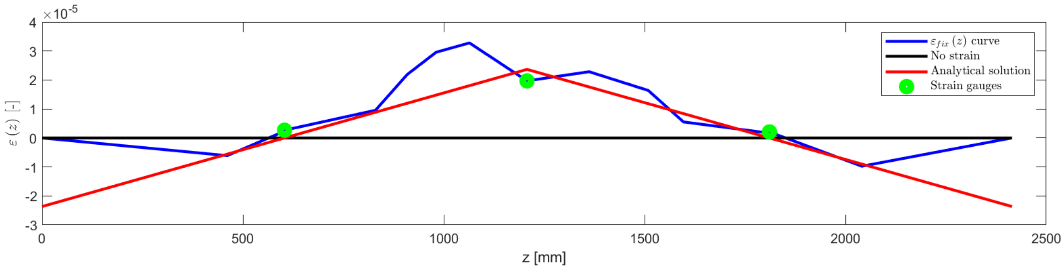

(a) $\varepsilon_{fix}(z)$ *strain function*

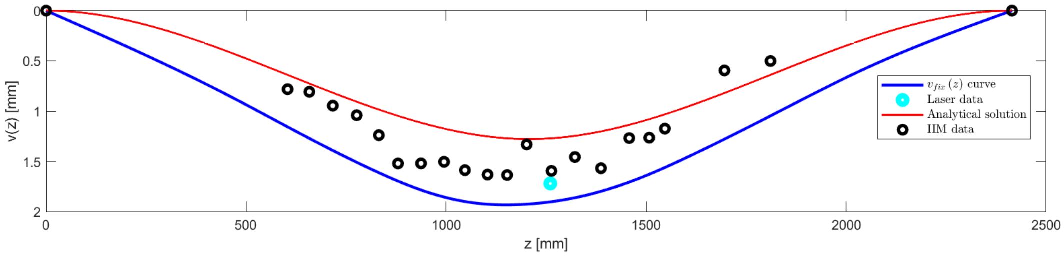

(b) $v_{fix}(z)$ *displacement function*

Figure 6.11: *Case 03 - Subcase 3*

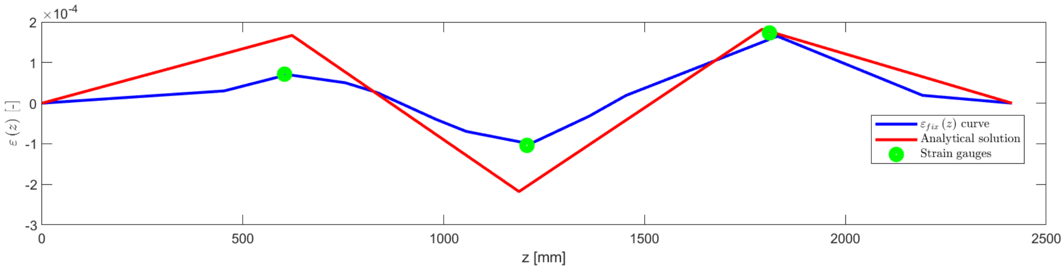

(a) $\varepsilon_{fix}(z)$ *strain function*

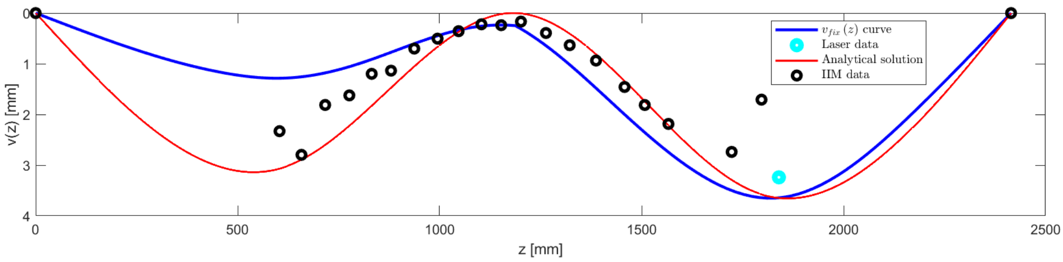

(b) $v_{fix}(z)$ *displacement function*

Figure 6.12: *Case 04 - Subcase 1*

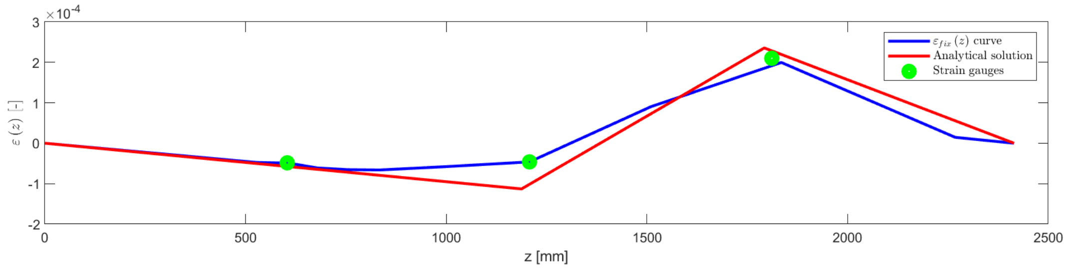

(a) $\varepsilon_{fix}(z)$ *strain function*

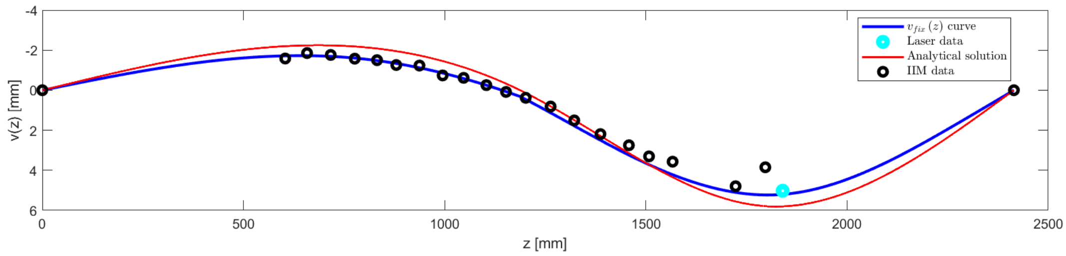

(b) $v_{fix}(z)$ *displacement function*

Figure 6.13: *Case 04 - Subcase 2*

Before assessing the accuracy of the method, some considerations are given. With regard to case studies 01 and 02, it is easily observed that the largest errors occur in case 1.1 (figures 6.5). The reason is that the accuracy of the IIM algorithm is of the same order of magnitude as the displacement measured by the laser, which leads to high errors. Another observation is that while in the case of a simply supported beam the reconstruction of displacements is accurate even in areas where no measurements are provided ($z < \frac{L}{4} \vee z > \frac{3L}{4}$), as the complexity of the boundary conditions increases, this accuracy decreases (figure 6.12). Finally, it is observed that in the case of a doubly clamped beam (figure 6.9:6.11) the strains are zero at the extremes. Not only the strain is zero where it should be maximum, but also the displacement field cannot be properly reconstructed. This constitutes a limitation of smoothing splines which can, however, be overcome by first measuring the strain of the beam in the vicinity of the constraint and then improving the strain field ($\varepsilon(z) \Rightarrow \varepsilon_{fix}(z)$).

6.1.4 Accuracy of method 1

To estimate the accuracy in reconstructing the deformation of the structure, the relative percentage error $err\%(v_{fix})$ between the displacement provided by the function $v_{fix}(z_{laser})$ and the displacement provided by the laser sensor v_{laser} is calculated, whereby

$$err\%(v_{fix}) = \frac{v_{fix}(z_{laser}) - v_{laser}}{v_{laser}} \cdot 100 \tag{6.4}$$

The relative percentage error $err\%(v_{fix})$ is compared with the relative percentage error $err\%(v)$ of the function $v(z)$, the one computed after the smoothing parameter reduction. The comparison is carried out to see whether or not it is convenient to perform this method of data fusion. The results are reported in table 6.11.

Case study	Sensor displacement	$v_{fix}\left(\frac{L}{2}\right)$ $[mm]$	$v\left(\frac{L}{2}\right)$ $[mm]$	$err\%$ (v_{fix})	$err\%$ (v)
1.1	0.53 mm	0.50 mm	0.51 mm	-5.1%	-4.2%
1.2	2.09 mm	2.00 mm	1.96 mm	-4.0%	-6.2%
1.3	5.18 mm	5.12 mm	5.10 mm	-1.1%	-1.5%
2	2.85 mm	2.84 mm	2.82 mm	-0.3%	-1.2%

Table 6.11: *Method 1 results*

It can be seen that data fusion and data interpolation by means of smoothing splines are both effective methods, with errors committed below 6%. The data fusion provides more accurate results, except for case 1.1. In the latter, the discrete displacement data are already very noisy and their derivation and subsequent integration only increase this noise. Since the measurements provided by the strain gauges are accurate in this case (table 6.1), the only way to increase the accuracy of the displacement field is to use a camera with a higher resolution.
For the other cases, however, the estimation of discrete displacements is more accurate (see Figures 6.6(b), 6.7(b) and 6.8(b)), leading to improved results.
In general, method 1 provides very accurate results, despite the imperfect alignment/positioning of the strain gauges. It is very important that the values provided by these are accurate since it is with these that the strain field $\varepsilon(z)$ is corrected. If these provide incorrect results, the resulting displacement field $v_{fix}(z)$ will be inaccurate. Referring to the figure 6.8(a), it can be seen that the strain gauge set at $z = \frac{L}{2}$ deviates from the theoretical value (error of -21.7% table 6.4) and this leads to a loss of accuracy in $v_{fix}(z)$: it can be observed in figure 6.8(b) how the first part of the curve, about the first quarter, deviates from the theoretical trend. This observation highlights another important aspect: having a single point of measurement to assess the accuracy of the displacement field is insufficient. In fact, it could happen, as in figure 6.5, that the function $v_{fix}(z)$ deviates from the actual trend except for a few points as the midpoint. Evaluating the accuracy at that point alone would seem to yield positive results, although that is not true.

In view of these considerations, it emerges that using a single reference value to assess the accuracy of the method is not sufficient. In spite of this, the first experiment made it possible to point out what changes needed to be made to the second experimental test in order to apply the 3 methods and compare them. These are:

- the use of a sufficient number of strain gauges to be able to perform shape sensing via iFEM;
- placing at least one strain gauge close to the constraints;
- shooting the entire beam with the camera;
- having several experimental measurement points of the beam displacement to be able to estimate the accuracy of the methods;
- the use of experimental constraints that act like ideal ones.

6.2 Experiment 2

As in the first experiment, tables are provided showing the values experimentally measured by the sensors, the theoretical values provided by beam theory, and the relative percentage error between the experimental and theoretical measurements. Since the purpose is to highlight the correctness of the experimental test execution, reporting tables for each test and each load condition would be redundant. For this reason, only the results obtained in the load case $m = 5\,\mathrm{kg}$ are reported.

6.2.1 Experimental measurements

One aspect to mention is that while Tests 1, 2, and 3 were performed in succession, with the load applied at the same position, Tests 4 and 5 were performed with a different point of load application than Tests 1:3. During Test 3 when reading in real-time the displacements provided by the LVDTs, it was realized that the displacement provided by the LVDTs at the tip was less than that provided at $z = 1004\,\mathrm{mm}$. The cause of this was due to the incorrect positioning of the LVDTs at the TIP, which does not work well when working near the end of the range. After changing the set-up, the load rod was repositioned, thus changing the point of load application compared to the previous tests.
The results are reported in table 6.12. To give a more immediate idea of the goodness of measurements, the following legend was used for relative percentage errors:

- green cell for $|err\%| \leq 20\%$;
- blue cell for $20\% < |err\%| < 50\%$;
- red cell for $|err\%| \geq 50\%$;

It is also specified that in order to perform a comparison between analytical and experimental strains, the analytical strains were calculated in terms of axial strains, and the experimental values measured by the strain gauges placed at $\pm 45°$ were converted into axial strains.

Strain gauges - location	Anal. Solut. $[\mu m/m]$	T2 $[\mu m/m]$	Err% T2 [%]	T3 $[\mu m/m]$	Err% T3 [%]	T4 $[\mu m/m]$	Err% T4 [%]	T5 $[\mu m/m]$	Err% T5 [%]
SG - Root Top	250.022	236.696	-5.3	240.382	-3.8	232.000	-7.2	234.473	-6.2
SG - Root Bottom	-250.022	-249.808	-0.1	-247.999	-0.8	-257.681	3.1	-257.161	2.8
SG - L/6 Top	210.303	231.053	9.9	238.832	13.6	213.824	1.7	216.331	2.9
SG - L/6 Lateral	-61.416	-57.966	-5.6	-51.917	-15.5	-71.915	17.1	-70.799	15.3
SG - L/6 Bottom	-210.303	-216.333	2.9	-211.232	0.4	-228.484	8.6	-228.131	8.5
SG - L/3 Top	167.802	169.303	0.9	178.515	6.4	147.425	-12.1	149.797	-10.7
SG - L/3 Lateral	-49.004	-47.220	-3.6	-40.556	-17.2	-63.984	30.6	-62.222	27.0
SG - L/3 Bottom	-167.802	-165.863	-1.2	-160.595	-4.3	-179.825	7.2	-178.397	6.3
SG - 2L/3 Top	82.800	79.148	-4.4	90.445	9.2	51.621	-37.6	54.664	-34.0
SG - 2L/3 Lateral	-24.181	-29.626	22.5	-21.788	-9.9	-48.797	101.8	-46.585	92.6
SG - 2L/3 Bottom	-82.800	-89.228	7.8	-83.285	0.6	-103.821	25.4	-102.064	23.3
SG - 5L/6 Top	40.299	33.642	-16.5	46.134	14.5	8.490	-78.9	10.545	-73.8
SG - 5L/6 Lateral	-11.769	-14.088	19.7	-5.423	-53.9	-32.842	179.0	-30.987	163.3
SG - 5L/6 Bottom	-40.299	-40.242	-0.1	-33.674	-16.4	-55.490	37.7	-53.745	33.4
LVDTs/DIC - location	Anal. Solut. [mm]	T2 [mm]	Err% T2 [%]	T3 [mm]	Err% T3 [%]	T4 [mm]	Err% T4 [%]	T5 [mm]	Err% T5 [%]
LVDT L/2	1.407	1.310	-6.9	1.540	9.4	1.614	14.7	1.607	14.1
LVDT near TIP	3.908	4.195	7.3	4.147	6.1	4.319	10.5	4.298	10.0
LVDT W1	4.434	4.087	-7.8	4.133	-6.8	4.763	7.4	4.762	7.4
LVDT W2	4.434	4.436	0.1	4.144	-6.5	5.199	17.2	5.144	16.0
LVDT - mean W1 W2	4.434	4.262	-3.9	4.138	-6.7	4.981	12.3	4.953	11.7
DIC near TIP	3.908	4.260	9.0	4.196	7.4	4.364	11.7	4.347	11.2
DIC TIP	4.434	4.841	9.2	4.778	7.8	4.960	11.9	4.940	11.4

Table 6.12: *Experimental measurements and relative percentage errors for* $5\,\mathrm{kg}$

Focusing initially on strains, the following considerations are made:

- Tests 2 and 3 are those with measurements more in line with the analytical ones. The largest error is committed at the lateral strain gauge set at $z = \frac{5L}{6}$ in Test 3.
- The deviation from the theoretical trend becomes more pronounced in Tests 4 and 5, both for the lateral strain gauges and for the strain gauges at the bottom at the top. It is always the lateral strain gauges that exhibit the highest errors, with the error increasing towards the free end.
- In all tests, the experimental values tend to be in line with the analytical values up to the stretch $z = \frac{L}{3}$, after which the deviation from the theoretical trends occurs; in Tests 4 and 5, the deviation is even more pronounced than in Tests 2 and 3.

Focusing now on displacements, four main aspects can be observed:

- The measurements provided by DIC are always accurate, in line with the theoretical ones, and, compared to the latter, always in excess. This is because the weight of the loading system and the pressure, although small, exerted by the LVDTs were not taken into account in the theoretical solution. For this reason, it is safe to say that the displacements calculated with DIC are accurate.
- For tests 2 and 3, the displacement recorded by the LVDTs at the tip is lower than that recorded at $z = 1004\,\mathrm{mm}$ (LVDT near TIP) for the cause discussed above. Subsequently, once their setting was changed, subsequent tests no longer found this anomaly.
- The measurements of the DIC coincide with those of the LVDTs (except with the LVDTs at TIP in tests 2 and 3).
- The errors committed in Tests 4 and 5 are greater than those committed in Tests 2 and 3.

As a final result of the considerations concerning both strains and displacements, it appears that the errors increase towards the free end of the beam, and are greater for cases 4 and 5. The reason why this occurs is due to the fact that the analytical solution was calculated for the case of pure bending; in the various tests, however, it was not possible to load the beam exactly in the shear center. This results in the beam twisting, which becomes more and more pronounced as the load increases and towards the free end.
The beam torsion is captured by the 3D DIC, and the out-of-the-plane displacements range $[u_{min}(z)\,; u_{max}(z)]$ (direction x) are reported for each test (figure 6.14:6.15).

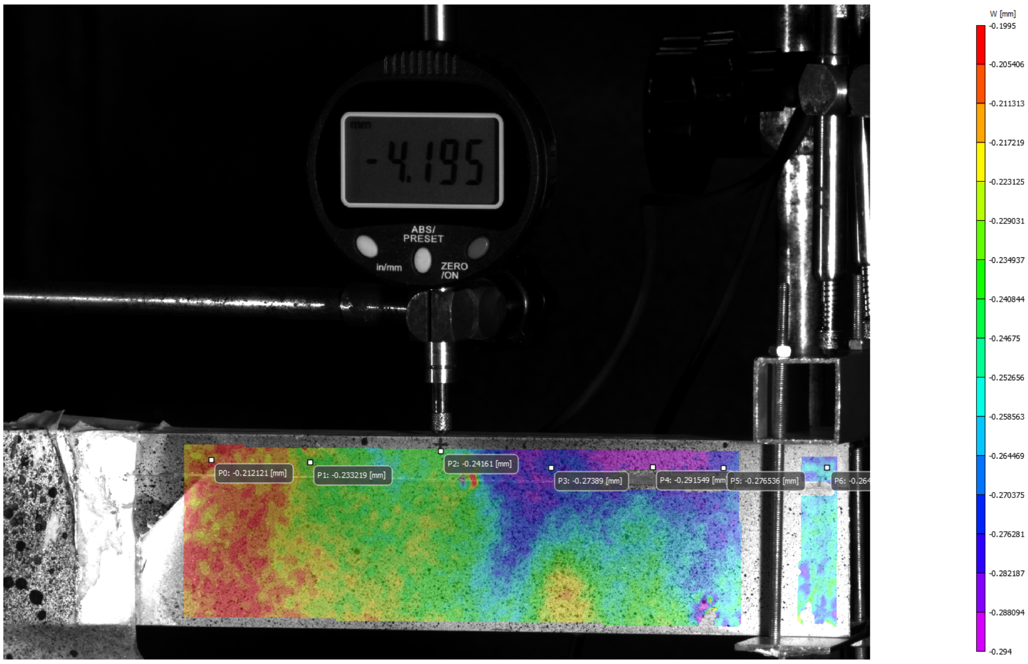

(a) Test 2 $(-0.294; -0.1995)\,mm$

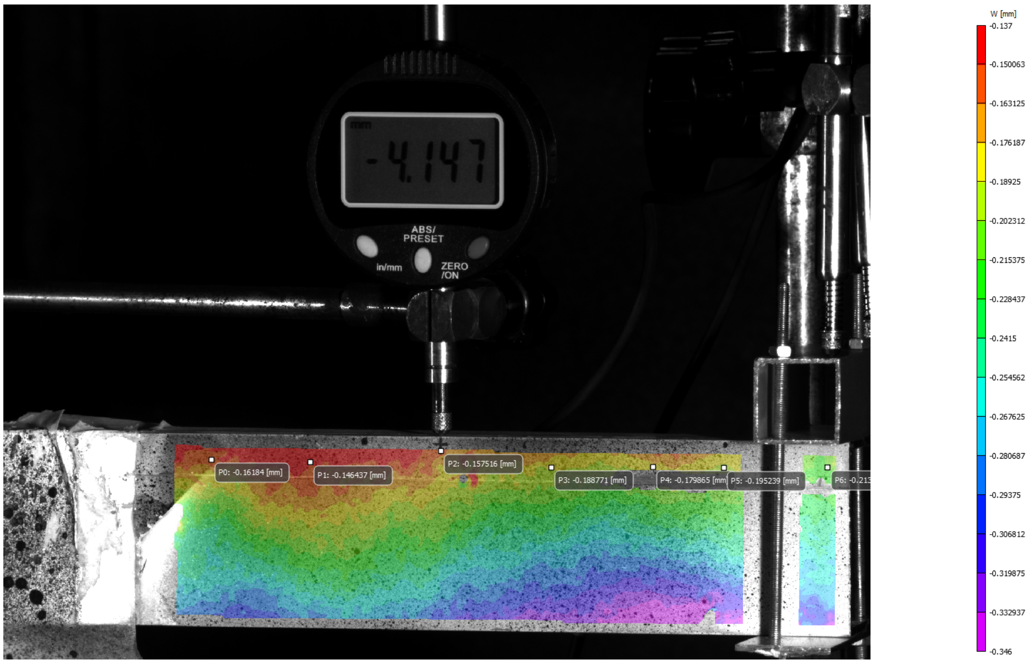

(b) Test 3 $(-0.346; -0.137)\,mm$

Figure 6.14: $u\,(z)$ *displacement*

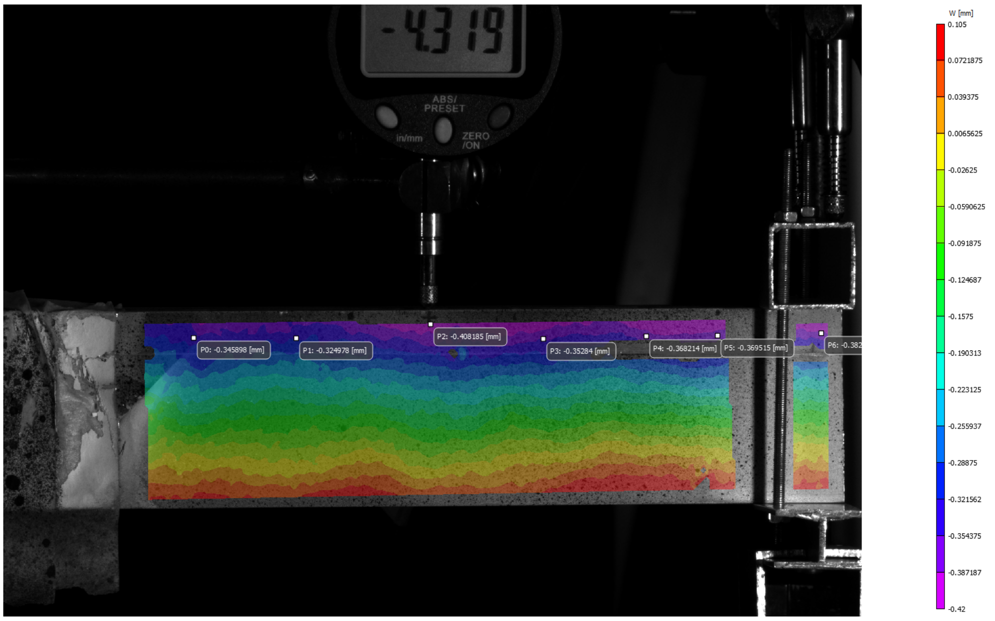

(a) Test 4 $(-0.420; 0.105)\,mm$

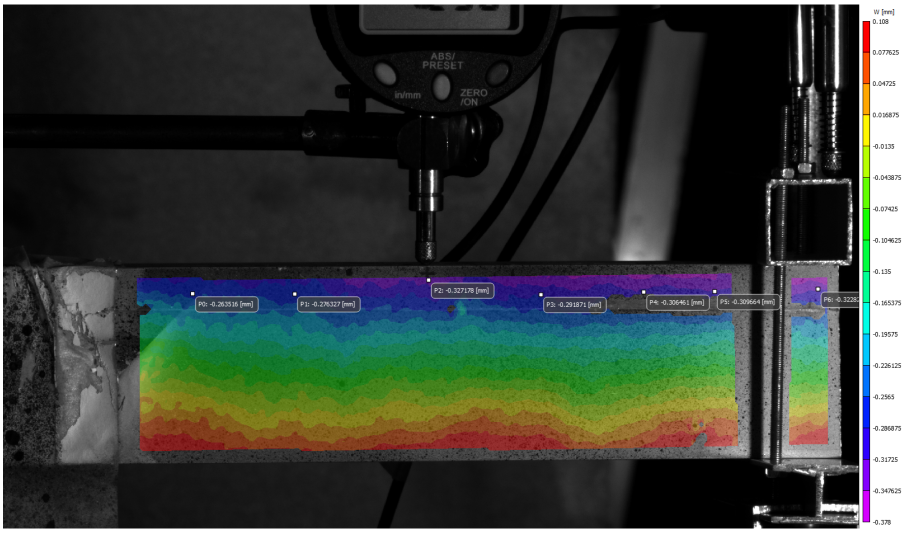

(b) Test 5 $(-0.378; 0.108)\,mm$

Figure 6.15: $u\,(z)$ *displacement*

Looking at the out-of-the-plane displacements range, it can be seen that the torsion is greater in Tests 4 and 5, where the difference between the maximum displacement $u_{max}\,(z)$ and the minimum displacement $u_{min}\,(z)$ is $0.525\,\text{mm}$ and $0.486\,\text{mm}$, respectively, while in Tests 2 and 3, such differences are $0.0945\,\text{mm}$ and $0.209\,\text{mm}$, respectively.
Following these considerations, it emerges that the experimental measurements are in line with the theoretical ones, with the errors committed with respect to the pure bending solution being greater or lesser depending on the intensity of the torsion. Finally, it can be stated that the experimental measurements, except for the measurements of LVDTs W1 and W2 for tests 2 and 3, are correct. However, since the pure bending case is to be investigated and the contribution of torsion to strain cannot be taken into account (there would have to be four strain gauges for each section), it was decided to exclude Tests 4 and 5 from the analysis of results.

6.2.2 Method 1 results

In this section, the corrected displacement function $v_{fix}(z)$ and the corrected strain function $\varepsilon_{fix}(z)$ are reported for tests 2 and 3 for the case $m = 5\,\text{kg}$. In addition, the lowest available exposure value was used for each test, both -1.0 EV for tests 2 and 3. The following legend was used in the graphs showing the strain trends:

- blue for the $\varepsilon_{fix}(z)$ curve;
- red for the analytical strain solution curve computed for the case of pure bending;
- green dots for the strain gauges values.

For the displacements:

- blue for the $v_{fix}(z)$ curve;
- red for the analytical displacements solution computed for the case of pure bending;
- black dots for the discrete displacements computed with the IIM method;
- green dots for the LVDT measurements;
- green dots for the DIC measurements obtained at LVDT locations.

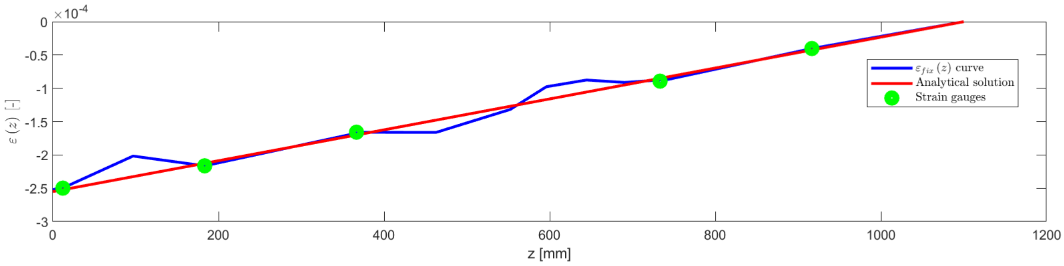

(a) $\varepsilon_{fix}(z)$ *strain function*

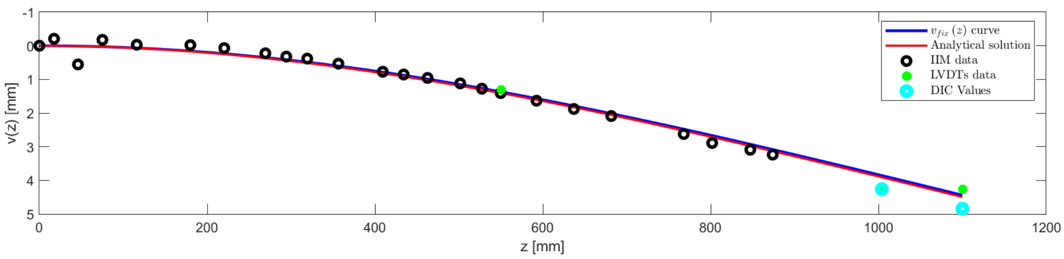

(b) $v_{fix}(z)$ *displacement function*

Figure 6.16: *Test 2*

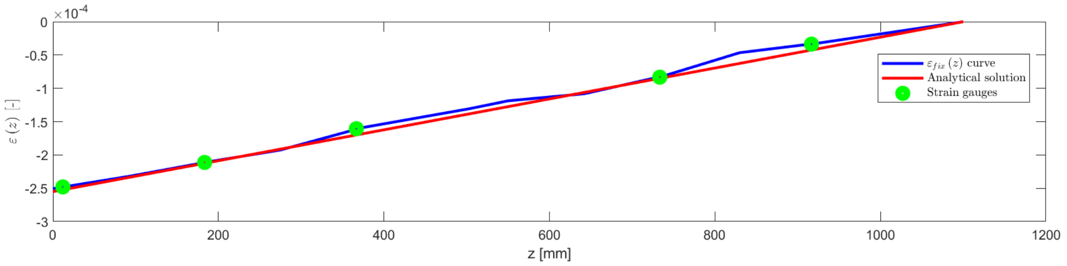

(a) $\varepsilon_{fix}\,(z)$ *strain function*

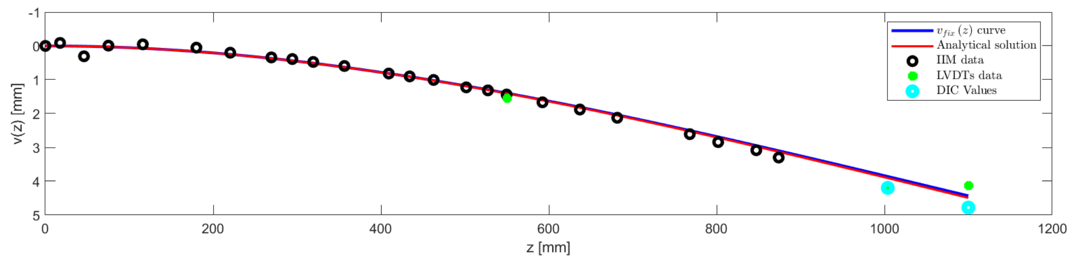

(b) $v_{fix}\,(z)$ *displacement function*

Figure 6.17: *Test 3*

Unlike the first experiment, a parametric analysis for the reduction of the smoothing parameter was not performed since it has been used the same smoothing parameter reduction factor K.
Looking at the figures related to the displacement field, it can be seen that the discrete displacements calculated using the IIM method are quite accurate. In fact, comparing the LVDT value at the centreline with the displacement calculated by the IIM method at the same coordinate $z = \frac{L}{2}$, these are almost coincident. The displacements that deviate from the expected trend are those in the region near the clamp constraint. That was to be expected: remember that the adhesive tape has been removed in this area, making the surface reflective (figure 5.14) and making it difficult for the IIM function to calculate displacements.
The strains calculated at the bottom of the beam were used to calculate the strain field $\varepsilon_{fix}\,(z)$. Strains at the top were not used because the strain gauge placed at $z = 12\,\mathrm{mm}$ provided strains, in modulus, equal to or less than the strain gauge placed at $z = \frac{L}{6}$. Comparing the values $\varepsilon_{bottom}\,(12mm)$ with those of $\varepsilon_{top}\,(12mm)$ in table 6.12, it is observed that the values of $\varepsilon_{bottom}\,(12mm)$ are greater; moreover, the errors committed with respect to the theoretical solution of pure bending are lower. The lateral strains were not used because as there was no lateral strain gauge available at $z = 12\,\mathrm{mm}$, it would not have been possible to correct the strain in the clamp section $z = 0\,\mathrm{mm}$ (without any additional assumptions being made).
Looking at the strains corrected field, $\varepsilon_{fix}\,(z)$, it can be seen that the precautions taken to correct the strain at the clamp worked. Furthermore, not having a zero strain at $z = 0\,\mathrm{mm}$ also guarantees a displacement function that has the typical clamp deformation around the constraint.
Qualitatively, the reconstructions of the strain field $varepsilon_{fix}\,(z)$ and displacement $v_{fix}\,(z)$ are accurate.

6.2.3 Accuracy of method 1

As observed in section 6.2.1, the DIC measurements are in line with those of the LVDTs, and since the DIC provides a higher number of displacements, it was decided to compare the displacements calculated by the displacement functions $v_{fix}(z)$ with the displacement measured by the LVDT placed at the centreline and the displacements calculated by the DIC. The measurement results are shown in table 6.13. In this case, for each test, the cells with the lowest relative percentage error have been marked in green, and the cells with the highest relative error in red. In addition, table 6.14 compares the relative percentage errors *Err%* committed with respect to the LVDT placed in the centreline, between the displacement function before the data fusion ($v(z)$) and after the fusion($v_{fix}(z)$). It was not possible to make a comparison with the displacements provided by the DIC as this region was masked.

Test 2	LVDT locations [mm]	DIC locations [mm]	v_{fix} value [mm]	Sensor value [mm]	Absolute error [mm]	Relative percentage error [%]
	555.000	-	1.370	1.310	0.060	4.6
	-	949.004	3.526	3.906	-0.380	-9.7
	-	972.766	3.668	4.060	-0.392	-9.6
	-	1004.000	3.856	4.260	-0.403	-9.5
	-	1030.300	4.015	4.431	-0.415	-9.4
	-	1054.408	4.162	4.580	-0.419	-9.1
	-	1071.114	4.263	4.688	-0.425	-9.1
	-	1095.466	4.411	4.841	-0.430	-8.9
Test 3	LVDT locations [mm]	DIC locations [mm]	v_{fix} value [mm]	Sensor value [mm]	Absolute error [mm]	Relative percentage error [%]
	555.000	-	1.398	1.540	-0.142	-9.2
	-	948.992	3.536	3.846	-0.310	-8.0
	-	972.767	3.676	3.995	-0.320	-8.0
	-	1004.000	3.860	4.196	-0.336	-8.0
	-	1029.887	4.016	4.363	-0.347	-8.0
	-	1054.408	4.159	4.516	-0.357	-7.9
	-	1071.115	4.259	4.623	-0.365	-7.9
	-	1095.469	4.404	4.788	-0.384	-8.0

Table 6.13: *Absolute and relative percentage errors* - 5 kg

$m = 5$ kg	LVDT L/2 [mm]	$v_{fix}(L/2)$ [mm]	$v(L/2)$ [mm]	Err% $v_{fix}(z)$	Err% $v(z)$
Test 2	1.310	1.370	1.396	4.6	6.6
Test 3	1.540	1.398	1.438	-9.2	-6.7

Table 6.14: *Comparison of centreline displacement before and after data fusion*

Analysing the results provided in table 6.13, it can be seen that the reconstruction of the deformed structure was effective. In fact, the largest error committed was -9.7%.

With reference to the table 6.14, it is observed that the data fusion leads to an improvement in the calculation of the displacement only in Test 2. Although in Test 3 the displacements calculated with data fusion are less accurate than that calculated without fusion, the difference is very small.

However, it should be remembered that without data fusion, it would not have been possible to calculate the displacements in the ROI of the DIC, where the IIM method failed due to excessive brightness.

6.2.4 Method 2 results

For ease of discussion, the tables schematizing the combinations analyzed with iFEM are shown here.

Case	BeamElement	Sections zi	Weight = 1	Weight = 0.5	Weight = 0.1
1	1 EB	L/3, 2L/3	L/3, 2L/3	-	-
2	1 EB	L/6, 5L/6	L/6, 5L/6	-	-
3	2 EB	L/6, L/3, 2L/3, 5L/6	L/6, L/3, 2L/3, 5L/6	-	-
4,5	2 EB	L/12, L/4, L/3, 5L/12, 7L/12, 2L/3, 3L/4, 11L/12	L/3, 2L/3	L/12, L/4, 5L/12, 7L/12, 3L/4, 11L/12	
6,7	2 EB	L/12, L/6, L/4, 5L/12, 7L/12, 3L/4, 5L/6, 11L/12	L/6, 5L/6	L/12, L/4, 5L/12, 7L/12, 3L/4, 11L/12	
8,9	2 EB	L/12, L/6, L/3, L/4, 5L/12, 7L/12, 2L/3, 3L/4, 5L/6, 11L/12	L/6, L/3, 2L/3, 5L/6	L/12, L/4, 5L/12, 7L/12, 3L/4, 11L/12	
10,11	3 EB	L/12, L/6, L/3, L/4, 5L/12, 7L/12, 2L/3, 3L/4, 5L/6, 11L/12	L/6, L/3, 2L/3, 5L/6	L/12, L/4, 5L/12, 7L/12, 3L/4, 11L/12	
12	1 T	L/3, 2L/3	L/3, 2L/3	-	-
13	2 T	L/6, L/3, 2L/3, 5L/6	L/6, L/3, 2L/3, 5L/6	-	-

Table 6.15: *iFEM case study*

In the table 6.15, the Bernoulli-Euler beam element is indicated by *EB* and the Timoshenko beam element by *T*. Furthermore, the various cases will be referred to by the number indicated in the appropriate column *case*; if there are 2 cases in the same row, the first will refer to Weight $= 0.5$, the second to Weight $= 0.1$.
The results of the analysis are shown in table 6.16.

Test 3	Near tip			Tip		
Case	DIC [mm]	v [mm]	Err% [%]	DIC [mm]	v [mm]	Err% [%]
1	4.196	4.005	-4.5	4.788	4.610	-3.7
2	4.196	4.164	-0.8	4.788	4.782	-0.1
3	4.196	4.153	-1.0	4.788	4.767	-0.4
4	4.196	4.023	-4.1	4.788	4.623	-3.4
5	4.196	4.014	-4.3	4.788	4.613	-3.6
6	4.196	4.087	-2.6	4.788	4.693	-2.0
7	4.196	4.123	-1.7	4.788	4.734	-1.1
8	4.196	4.072	-3.0	4.788	4.677	-2.3
9	4.196	4.100	-2.3	4.788	4.707	-1.7
10	4.196	4.048	-3.5	4.788	4.649	-2.9
11	4.196	4.091	-2.5	4.788	4.695	-1.9
12	4.196	4.374	4.2	4.788	5.014	4.7
13	4.196	4.570	8.9	4.788	5.220	9.0

Table 6.16: *iFEM results*

Focusing on cases 1 to 3, 12, and 13, it is observed that the reconstruction of the deformation of the structure is best in case 2, which is also the best case among all those analyzed, while the worst results are those of case 13. Case 2 is the one in which only 1 EB element is used with sections $z = \left(\frac{L}{6}, \frac{5L}{6}\right)$, while case 13 is the one in which 2 Timoshenko finite elements are used with sections $z = \left(\frac{L}{6}, \frac{2L}{3}, \frac{5L}{6}\right)$. Looking at case 12, the other case in which the Timoshenko element is used, the error committed is always very high.

In Test 3, the relative errors committed without using iFEM were -8.0%, both for near-tip and at-tip displacement. Comparing these errors with those committed with data fusion using iFEM, it can be seen that the latters are better: the maximum errors committed are -4.3% and -3.6% for near-tip and tip displacement respectively (Case 5). The best results of the data fusion are obtained in case 7, where the only difference with case 5 lies in the sections to which a unit weight has been associated, the outer ones being in case 5 and the inner ones in case 7. This variability in error due to the chosen sections to be assigned unit weights, also occurs in the case of iFEM without data fusion, in cases 1 and 2. Therefore, using the strains provided by the outermost sensors leads to better results.

On the other hand, comparing case 2 and case 7, it can be seen that data fusion fails to provide more accurate results than iFEM when used individually. Furthermore, the use of a weight of 0.1 associated with the sectional strains calculated from the strains provided by the function $\varepsilon_{fix}(z)$ leads to slightly lower errors than the weight of 0.5, except for cases 4 and 5 where this does not occur.

These data show that the use of additional strain sections provided by the function $\varepsilon_{fix}(z)$ does not lead to an improvement in the reconstruction of the structure deformation obtained by using iFEM alone (with Bernoulli-Euler), even if a lower weight is associated with them. On the other hand, data fusion with the Bernoulli-Euler iFEM leads to an improved reconstruction of the deformed structure, as well as providing more accurate results than the iFEM in the case of Timoshenko.

7 Conclusions

In this thesis, a method was developed to combine displacement measurements obtained by utilizing an image registration technique based on Thirion's demons method, with strain measurements provided by strain gauges. The latter, by means of shape-sensing techniques, allows the deformation of the structure to be reconstructed. The reason why this kind of data fusion was inspected is due to the different characteristics of the data to be combined. In fact, while the data provided by image registration are numerous, those provided by strain gauges are punctual and depend on the number of them installed on the structure. To reconstruct the deformation of the structure accurately, a certain number of sensors must be installed, which requires a certain amount of time. On the other hand, image registration allows a great amount of data to be obtained with minimal instrumentation, as one or two cameras are sufficient depending on the displacement to be reconstructed, 2D and 3D respectively. However, the data provided by image registration are very noisy, unlike strain gauge data, which are very accurate. Therefore, the data fusion performed in this thesis was aimed at exploiting the numerosity of the displacement data provided by image registration by mitigating the noise through strain gauge measurements. To combine the data fusion method with iFEM, the former was developed to be compatible with the latter. The method designed allows the shape reconstruction of the beam from images of the structure before and after deformation, the knowledge of its geometric properties, the boundary conditions, and the position of the strain gauges. No assumptions are therefore made about the loads acting on the structure and the material from which it is made.

This method was tested in two experiments, in which different types of boundary conditions and loads were analyzed.

Two data fusion methods were carried out. The two methods have in common the first steps, i.e. the calculation of the displacement function $v(z)$ from the displacements calculated by the image registration technique, the double derivation of the displacement field to derive the axial strain field $\varepsilon(z)$ and the correction of the latter by strain gauge measurements to obtain the strain field $\varepsilon_{fix}(z)$. While in method 1, the corrected strain field $\varepsilon_{fix}(z)$ is integrated twice to calculate the corrected displacement field $v_{fix}(z)$, in method 2, the corrected strain field $\varepsilon_{fix}(z)$ is used to provide the iFEM with additional strain sections.

One of the most complicated aspects to handle was the interpolation of the displacement data provided by the image registration. The complexity was due to having to interpolate data that was very noisy, without knowing the type of interpolating function. Therefore, a perfect fit of the data would not have been useful for the reconstruction of the deformation, and a least-squares interpolation, without knowing the degree of the interpolating polynomial, was an impractical route. This obstacle was overcome by the use of smoothing splines, which effectively solved this problem but created another. One property of smoothing splines is that the second derivative of the function cancels at the extremes. This constitutes a non-negligible problem if there are clamp constraints at the ends; where one would expect a maximum strain, this is instead

zero.
In the first experiment, only method 1 was applied due to the small number of strain gauges, which were insufficient to perform iFEM. In this experiment, the displacements calculated by the function $v_{fix}(z)$ for the case of a simply supported beam were compared with the measurement of the laser sensor, placed at the point of maximum beam deflection, with relative errors committed of less than 6%
In the second experiment, the case of a cantilever beam was analyzed, thus investigating the most critical condition in the calculation of the strain field. By placing a strain gauge in the vicinity of the clamp constraint, it was possible to correct the strain in and around the constraint section, thus improving the resulting strain field $\varepsilon_{fix}(z)$. Furthermore, this experiment was carried out so that the two methods could be applied, and thus compared. In the case of the first method, the results obtained were quite accurate with the absolute errors made with respect to the sensor measurements not exceeding 10%. The best results, relative to method 1, were obtained in the first experiment. However, in the first experiment, the condition investigated was that of simple support, and the deformation of the structure to be reconstructed had a lower complexity than that of the cantilever beam. Furthermore, while in the first experiment it was possible to ensure homogenous brightness over the entire beam, in the second experiment this was not possible due to the intense brightness required for the correct functioning of the DIC.
In the second experiment, a comparison was made between the displacements obtained with method 1, method 2, and pure iFEM. The analysis showed that the best results are obtained in the case of the pure Bernoulli-Euler iFEM, while the least accurate with the pure Timoshenko iFEM. Furthermore, while the errors committed in method 1 were 8 %, these were halved in method 2, where the maximum error did not exceed $|4.3\%|$. Furthermore, in one of the cases analyzed with method 2, an accuracy comparable to that of the pure Bernoulli-Euler iFEM is obtained.

Overall, although certain precautions must be taken to ensure the proper functioning of data fusion, such as homogeneous illumination over the entire structure and the presence of strain gauges in the vicinity of the constraints in the case of clamp constraints, the data fusion developed turns out to be an effective method in reconstructing the deformation of the structure. Further developments of this method can be focused on the calculation of displacements in the case of 2D structures such as plates and out-of-plane displacements of slender beams.

A Expression of Lagrange polynomials

The first- and second-order Lagrange shape functions are the following,

$$
\begin{aligned}
\left[L_1^{(1)}, L_2^{(1)}\right] &\equiv \frac{1}{2}\left[\left(1-\xi\right), \left(1+\xi\right)\right] \\
\left[L_1^{(2)}, L_r^{(2)}, L_2^{(2)}\right] &\equiv \frac{1}{2}\left[\xi\left(\xi-1\right), 2\left(1-\xi^{(2)}\right), \xi\left(\xi+1\right)\right]
\end{aligned}
\tag{A.1}
$$

where $\xi \equiv \frac{2x}{l^e} - 1 \in [-1, 1]$ is a dimensionless axial coordinate; $x \in [0, l^e]$ and l^e is the element length. The subscripts 1 and 2 are labels representing the end nodes, while r denotes the central node. Third-order shape functions have the form

$$
\left[N_1^{(3)}, N_r^{(3)}, N_2^{(3)}\right] \equiv \frac{l^e}{24}\left(1-\xi^{(2)}\right)\left[\left(2\xi-3\right), -4\xi, \left(2\xi+3\right)\right] \tag{A.2}
$$

B Smoothing spline formulation

Let it be assumed that pairs of points x_i, y_i are given for $i = 0, ..., n$, with $x_0 < x_1 < ... < x_n$, although the discussion can be extended in the case of coincident abscissae [34]. The smoothing function $f(x)$ must be constructed so as to minimize the integral

$$\int_{x_0}^{x_n} g''(x)^2 \, dx \tag{B.1}$$

between all functions $g(x)$ so that

$$\sum_{i=0}^{n} \left(\frac{g(x_i) - y_i}{\delta y_i} \right)^2 \leq S, \quad g \in C^2 [x_0, x_n] \tag{B.2}$$

S is a constant and allows the quantity δy_i which controls the amount of smoothing to be implicitly scaled. If $S = 0$ it falls into the case of splines. The equation B.1 influences the form of the function $f(x)$ much more in the smoothing $(S > 0)$ than in the interpolation $(S = 0)$. The solution of the equations B.1 and B.2 can be obtained by the standard methods of calculating variations. Introducing the auxiliary variable z and the Lagrangian parameter p, one must search for the minimum of the functional

$$\int_{x_0}^{x_n} g''(x)^2 \, dx + p \left\{ \sum_{i=0}^{n} \left(\frac{g(x_i) - y_i}{\delta y_i} \right)^2 + z^2 - S \right\} \tag{B.3}$$

From the corresponding Euler-Lagrange equations, the optimal function $f(x)$ is determined:

$$f''''(x) = 0, \quad x_i < x < x_{i+1}, \quad i = 0, ..., n-1, \tag{B.4}$$

$$f^{(k)}(x_i)_- - f^{(k)}(x_i)_+ = \begin{cases} 0 & \text{if } k = 0, 1 \quad (i = 1, ..., n-1) \\ 0 & \text{if } k = 2 \quad (i = 0, ..., n) \\ 2p \frac{f(x_i) - y_i}{\delta y_i^2} & \text{if } k = 3 \quad (i = 0, ..., n), \end{cases} \tag{B.5}$$

with $f^{(k)}(x_i)_\pm = \lim_{k \to x_0} f^{(k)}(x_i \pm h)$.
The equations B.4 and B.5 prove that the extremal function $f(x)$ is composed of cubic functions

$$f(x) = a_i + b_i(x - x_i) + c_i(x - x_i)^2 + d_i(x - x_i)^3, \quad x_i \leq x < x_{i+1} \tag{B.6}$$

which unite at their common endpoints in such a way that f, f' e f'' are continuous. By substituting the equation B.6 into B.5 and manipulating it, relationships between the coefficients of the splines are derived

$$\text{from } k = 2 \quad c_0 = c_n = 0, \quad d_i = \frac{c_{i+1} - c_i}{3h_i}, \quad i = 0, ..., n-1 \tag{B.7}$$

$$\text{from } k = 0 \quad b_i = \frac{a_{i+1} - a_i}{h_i} - c_i h_i - d_i h_i^2, \quad i = 0, ..., n-1 \tag{B.8}$$

$$\text{from } k = 1 \quad Tc = Q^T a, \tag{B.9}$$

$$\text{from } k = 3 \quad Qc = pD^{-2}(y - a) \tag{B.10}$$

where the following notation was used:

- $h_i = x_{i+1} - x_i$;
- $c = (c_1, ..., c_{n-1})^T$,
- $y = (y_0, y_1, ..., y_n)^T$,
- $a = (a_0, a_1, ..., a_n)^T$,
- $D = diag(\delta y_0, ..., \delta y_n)$,
- T is a positive definite tridiagonal matrix of order $n - 1$:

$$t_{i,i} = \frac{2(h_{i-1} + h_i)}{3}, \quad t_{i,i+1} = t_{i+1,i} = \frac{h_i}{3}$$

- Q is a tridiagonal matrix with $n + 1$ rows and $n - 1$ columns:

$$q_{i-1,i} = \frac{1}{h_{i-1}}, \quad q_{i,i} = -\frac{1}{h_{i-1}} - \frac{1}{h_i}, \quad q_{i+1} = \frac{1}{h_i}$$

Multiplying the first member of the equation B.10 by $Q^T D^2$ yields the variable c:

$$\left(Q^T D^2 Q + pT\right)c = pQ^T y, \tag{B.11}$$

$$a = y - p^{-1}D^2 Qc \tag{B.12}$$

In this way, if p is given, the parameter c is obtained from the equation B.11, and then the parameter a from B.12. Given a and c it is possible to calculate d and b from the equation B.7 and B.8 respectively.

B.1 Lagrangian parameter minimisation

Equation B.3 has to be minimised even with respect to p and z, leading to the following conditions:

$$pz = 0 \tag{B.13}$$

$$\sum_{i=0}^{n} \left(\frac{f(x_i) - y_i}{\delta y_i} \right)^2 = S - z^2 \tag{B.14}$$

Applying the equations B.11 and B.12, the first member of the equation B.14 can be expressed as $F(p)^2$ were

$$F(p) = ||DQ \left(Q^T D^2 Q + pT\right)^{-1} Q^T y||_2 \tag{B.15}$$

Observing the equation B.13 it is easy to see that it is fulfilled if $p = 0$ or if $z = 0$.
The first case is only possible if $F(0) \leq S^{\frac{1}{2}}$. This is true if the data points are such that the line applied to them with the least squares principle satisfies the equation B.2. From equation B.11 $c = 0$ is obtained and from equation B.12 for a limiting process

$$a = y - D^2 Q \left(Q^T D^2 Q\right) - 1 Q^T y$$

In this way, the cubic spline is reduced to a straight line.
If instead $F(0) > S^{\frac{1}{2}}$ then $p \neq 0$ e $z = 0$. In this case in the equation B.2 equality holds and p must be determined by the equation

$$F(p) = S^{\frac{1}{2}} \tag{B.16}$$

$F(p)$ is a strictly decreasing convex function if $p \geq 0$, where $F(p) \to 0$ for $p \to +\infty$. There is therefore one and only one positive root of the equation B.16. There is also at least one negative root. However, it can be shown that the value of the equation B.1 is greater for any negative root than for the positive root. Newton's method is used to calculate the positive root. Initialising $p = 0$, the $F(p)$ convexity ensures global convergence. The following abbreviation is introduced,

$$u = p^{-1} c = \left(Q^T D^2 Q + pT\right)^{-1} Q^T y$$

This results in $F(p)^2 = u^T Q^T D^2 Q u$ e

$$\begin{aligned} F\frac{dF}{dp} &= u^T Q^T D^2 Q \left(\frac{du}{dp}\right) \\ &= p u^T T \left(Q^T D^2 Q + pT\right)^{-1} T u - u^T T u \end{aligned} \tag{B.17}$$

For the calculation of u the Cholesky decomposition $R^T R$ of the positive definite band matrix $Q^T D^2 Q + pT$ is required. This symmetric decomposition could also be used for the calculation of the second member of the equation B.17. Thus, F is obtained from the triangular decomposition of $Q^T D^2 Q + pT$, by a forward substitution with R^T and a backward substitution with R. Multiplication with the tridiagonal matrix R^T and a second forward substitution with R^T yields $F \frac{dF}{dp}$.
Another way to determine the Lagrangian parameter is to apply Newton's method to the function $F\left(\frac{1}{\bar{p}} - S^{\frac{1}{2}}\right)$ starting with $\bar{p} = 0$ and producing the reciprocal value of p.

References

[1] Georgios Galanopoulos et al. “Health monitoring of aerospace structures utilizing novel health indicators extracted from complex strain and acoustic emission data”. In: *Sensors* 21.17 (2021), p. 5701.

[2] William L Ko, W Lance Richards, and Van T Tran. *Displacement theories for in-flight deformed shape predictions of aerospace structures*. Tech. rep. Nasa/TP-2007-214612, 2007.

[3] William L Ko and Van Tran Fleischer. *Further development of Ko displacement theory for deformed shape predictions of nonuniform aerospace Structures*. Tech. rep. Nasa/TP-2009-214643, 2009.

[4] Philip Bogert, Eric Haugse, and Ralph Gehrki. “Structural shape identification from experimental strains using a modal transformation technique”. In: *44th AIAA/ASME/ASCE/AHS/ASC Structures, Structural Dynamics, and Materials Conference*. 2003, p. 1626.

[5] R Bruno, N Toomarian, and M Salama. “Shape estimation from incomplete measurements: A neural-net approach”. In: *Smart Materials and Structures* 3.2 (1994), p. 92.

[6] Zhu Mao. *Comparison of shape reconstruction strategies in a complex flexible structure*. University of California, San Diego, 2008.

[7] Adnan Kefal et al. “A smoothed iFEM approach for efficient shape-sensing applications: Numerical and experimental validation on composite structures”. In: *Mechanical Systems and Signal Processing* 152 (2021), p. 107486.

[8] Alexander Tessler and Jan L Spangler. “A least-squares variational method for full-field reconstruction of elastic deformations in shear-deformable plates and shells”. In: *Computer methods in applied mechanics and engineering* 194.2-5 (2005), pp. 327–339.

[9] Marco Gherlone, Priscilla Cerracchio, and Massimiliano Mattone. “Shape sensing methods: Review and experimental comparison on a wing-shaped plate”. In: *Progress in Aerospace Sciences* 99 (2018), pp. 14–26.

[10] Marco Esposito and Marco Gherlone. “Composite wing box deformed-shape reconstruction based on measured strains: Optimization and comparison of existing approaches”. In: *Aerospace Science and Technology* 99 (2020), p. 105758.

[11] Barbara Zitova and Jan Flusser. “Image registration methods: a survey”. In: *Image and vision computing* 21.11 (2003), pp. 977–1000.

[12] T Schenk. “Digital Photogrammetry Volume I, TerraScience, Laurelville, Ohio, USA”. In: *Cited on* (1999), p. 70.

[13] Lisa Gottesfeld Brown. “A survey of image registration techniques”. In: *ACM computing surveys (CSUR)* 24.4 (1992), pp. 325–376.

[14] Bing Pan et al. “Two-dimensional digital image correlation for in-plane displacement and strain measurement: a review”. In: *Measurement science and technology* 20.6 (2009), p. 062001.

[15] Michael A Sutton et al. “The effect of out-of-plane motion on 2D and 3D digital image correlation measurements”. In: *Optics and Lasers in Engineering* 46.10 (2008), pp. 746–757.

[16] D Lecompte et al. “Analysis of speckle patterns for deformation measurements by digital image correlation”. In: *SPECKLE06: Speckles, From Grains to Flowers*. Vol. 6341. SPIE. 2006, pp. 80–85.

[17] David Lecompte et al. “Quality assessment of speckle patterns for digital image correlation”. In: *Optics and lasers in Engineering* 44.11 (2006), pp. 1132–1145.

[18] Junda Chen, Guanchang Jin, and Libo Meng. “Applications of digital correlation method to structure inspection”. In: *Tsinghua Science and Technology* 12.3 (2007), pp. 237–243.

[19] Sun Yaofeng and John HL Pang. “Study of optimal subset size in digital image correlation of speckle pattern images”. In: *Optics and lasers in engineering* 45.9 (2007), pp. 967–974.

[20] Bing Pan et al. “Full-field strain measurement using a two-dimensional Savitzky-Golay digital differentiator in digital image correlation”. In: *Optical Engineering* 46.3 (2007), pp. 033601–033601.

[21] Hubert W Schreier and Michael A Sutton. “Systematic errors in digital image correlation due to undermatched subset shape functions”. In: *Experimental Mechanics* 42 (2002), pp. 303–310.

[22] Hubert W Schreier, Joachim R Braasch, and Michael A Sutton. “Systematic errors in digital image correlation caused by intensity interpolation”. In: *Optical engineering* 39.11 (2000), pp. 2915–2921.

[23] Pan Bing et al. “Performance of sub-pixel registration algorithms in digital image correlation”. In: *Measurement Science and Technology* 17.6 (2006), p. 1615.

[24] J-P Thirion. “Image matching as a diffusion process: an analogy with Maxwell’s demons”. In: *Medical image analysis* 2.3 (1998), pp. 243–260.

[25] J-P Thirion. “Non-rigid matching using demons”. In: *Proceedings CVPR IEEE Computer Society Conference on Computer Vision and Pattern Recognition*. IEEE. 1996, pp. 245–251.

[26] Marco Gherlone et al. “An inverse finite element method for beam shape sensing: theoretical framework and experimental validation”. In: *Smart Materials and Structures* 23.4 (2014), p. 045027.

[27] Marco Gherlone et al. “Shape sensing of 3D frame structures using an inverse finite element method”. In: *International Journal of Solids and Structures* 49.22 (2012), pp. 3100–3112. ISSN: 0020-7683. DOI: https://doi.org/10.1016/j.ijsolstr.2012.06.009. URL: https://www.sciencedirect.com/science/article/pii/S0020768312002648.

[28] Rinto Roy, Marco Gherlone, and Cecilia Surace. “A shape sensing methodology for beams with generic cross-sections: Application to airfoil beams”. In: *Aerospace Science and Technology* 110 (2021), p. 106484.

[29] Pierclaudio Savino. “Shape sensing with inverse finite element method for slender structures”. In: *Structural Engineering and Mechanics, An Int’l Journal* 72.2 (2019), pp. 217–227.

[30] Frulla Giacomo. *Course slide of Experimentation on aerospace structures*. Tech. rep. Teaching material, Department of Mechanical and Aerospace Engineering (DIMEAS). Polytechnic University of Turin, 2023.

[31] Damien Kinet et al. "Fiber Bragg grating sensors toward structural health monitoring in composite materials: Challenges and solutions". In: *Sensors* 14.4 (2014), pp. 7394–7419.

[32] MATLAB. *9.13.0.2105380 (R2022b) Update 2*. Natick, Massachusetts: The MathWorks Inc., 2022.

[33] German Rodrıguez. "Smoothing and non-parametric regression". In: *New Jersey: Princeton University* (2001).

[34] Christian H Reinsch. "Smoothing by spline functions". In: *Numerische mathematik* 10.3 (1967), pp. 177–183.

Sitography

[35] IBM Cloud Education. *Reti neurali*. https://www.ibm.com/it-it/cloud/learn/neural-networks. Aug. 2020.
[36] Apex technologies. *Bragg fiber*. https://www.desmos.com/calculator?lang=it.
[37] SHOWA Strain Gages & Load Cells. *Electric strain gauge*. http://www.showa-sokki.co.jp/english/products_e/strain_gage_e/strain_gage_config_e.html.
[38] 80/20®. *Structural pivot*. https://8020.net/4195.html.